José Tomé Serra Afonso Figueira

Licenciado em Ciências de Engenharia Mecânica

Study and Validation of Constitutive Models for AHSS Steels

Dissertação para obtenção do Grau de Mestre em

Engenharia Mecânica

Orientador: Jorge Joaquim Pamies Teixeira, Professor Catedrático na Faculdade de Ciências e Tecnologia da Universidade Nova de Lisboa

Júri:

Presidente: Prof. Doutora Carla Maria Moreira Machado

Arguentes: Prof. Doutor Alexandre José da Costa Velhinho

Prof. Doutor Telmo Jorge Gomes dos Santos

FACULDADE DE CIÊNCIAS E TECNOLOGIA
UNIVERSIDADE NOVA DE LISBOA

Setembro 2018

Study and Validation of Constitutive Models for AHSS Steels

To my family

Acknowledgements

First, I would like to show my appreciation to my supervisor, Professor Jorge Pamies Teixeira for always being available to clarify any questions arose during this work. Thank you for your guidance, transmitted knowledge, inspiration, and for all the valuable advices on academic and professional matters. It was a privilege to have worked under the supervision of such a wise person.

To all the Professors of the Mechanical Engineering Department of Faculdade de Ciências e Tecnologia, Universidade Nova de Lisboa (FCT-UNL) for their contribution in my academic education. Also, a big thanks to engineer André Silva for all the help provided and complicity showed in difficult times. You always found the time to help me, even when you had a tight schedule.

A special note of heartfelt gratitude to all my family whom always supported me during my entire academic career. To my parents who taught me to never give up and for always showing unconditional support throughout this arduous journey. To my grandfathers who always inspired me and without them, none of this would have been possible. To my grandmothers, for all the support and whose delicious meals fed me and made me feel closer to home.

Finally, to my colleagues and friends, whose companionship and support was crucial during these past five years. A special note of thanks to Tiago Saraiva and Rui Comba, for all the challenges that we overcame together. To Gonçalo Serrano, David Negrão and Pedro Fernandes who were my companions in this journey that it is about to end.

Abstract

Advanced High Strength Steels have been extensively used in automotive industry due to their high yield and ultimate tensile strengths, allowing the production of lighter structural components for the car body structure without compromising safety requirements, however these steels exhibit a large springback phenomenon, after forming processes. To deal with this challenge, constitutive material models have been studied to capture the material behaviour under plastic deformation, and accurately predict the springback.

Making use of the material characterization tests previously performed, the aim of this dissertation is to study and validate constitutive material models for Dual-Phase steels, DP1000, and DP1200. For that, FEM simulations with LS-DYNA software were performed to study which material models better describe the material behaviour under different loading paths and in springback prediction. The Nakajima and notch tensile tests simulations were performed using explicit time integration to study the different loading paths, while for the U-shaped bend tests the simulation procedure was separated into two distinct simulations. A forming simulation with explicit time integration and a springback simulation with implicit time integration to validate constitutive models in its application for springback prediction. The results of the simulations were compared with the data obtained from experimental testing.

Regarding the loading path behaviour, the results indicate that most of the material models followed accurately the elementary loading paths, such as biaxial tension and uniaxial tension. As for the U-shaped bend test for the setup with the higher punch and die radiuses, the Yoshida-Uemori material model considering transverse anisotropy performed well in springback prediction.

Keywords: *Advanced High Strength Steels (AHSS), Dual-Phase steels (DP), Springback prediction, Constitutive material models, Loading paths*

Resumo

Os aços avançados de alta resistência têm sido muito utilizados na indústria automóvel, dadas as suas elevadas tensões de cedência e de rotura. Esta característica permite a produção de componentes estruturais mais leves para a carroçaria do automóvel, sem comprometer o cumprimento dos requisitos de segurança. No entanto, estes aços apresentam um fenómeno de recuperação elástica após serem submetidos a deformação plástica. Para enfrentar este problema, vários modelos constitutivos de material têm sido estudados e desenvolvidos com o objetivo de descrever o comportamento dos aços no domínio plástico e prever a recuperação elástica.

Utilizando os ensaios de caracterização que foram realizados em trabalhos anteriores, o objetivo desta dissertação é estudar e validar modelos constitutivos de material para os aços bifásicos DP1000 e DP1200. Para isso foram realizadas simulações no *software* de elementos finitos LS-DYNA de modo a estudar quais os modelos de material que melhor se adaptam a diferentes trajetórias de carga e na previsão da recuperação elástica. As simulações do ensaio de Nakajima e de tração com provetes entalhados, foram realizadas pelo método de integração explícito com o objetivo de estudar as diferentes trajetórias de carga, enquanto que as de dupla dobragem foram realizadas com duas simulações distintas. Uma simulação com a deformação do provete pelo método de integração explícito seguida de uma simulação de *springback* pelo método de integração implícito, para estudar a aplicação dos modelos à previsão da recuperação elástica. Os resultados das simulações são comparados com os resultados obtidos pela via experimental.

Os resultados desta dissertação mostram que a maior parte dos modelos de material conseguiram descrever as trajetórias de carga elementares, do estado de tensão biaxial e uniaxial. Quanto à previsão da recuperação elástica, o modelo de Yoshida-Uemori, considerando a anisotropia normal, destacou-se para os raios de matriz e punção mais elevados.

Palavras-Chave: *Aços Avançados de Alta Resistência (AHSS), Aços de dupla fase (DP), Previsão de springback, Modelos constitutivos de material, Trajetórias de carga*

Table of Contents

Acknowledgements v

Abstract vii

Resumo ix

Table of Contents xi

List of Figures xv

List of Tables xix

List of Symbols and Abbreviations xxi

1. Introduction 1

1.1 Motivation 1

1.2 Objectives 2

1.3 Structure 3

2. Literature Review 5

2.1 Advanced High Strength Steels 5

2.1.1 Transformation-Induced Plasticity Steels 6

2.1.2 Complex Phase Steels 7

2.1.3 Martensitic Steels 7

2.1.4 Dual-Phase Steels 7

2.1.5 Dual-Phase steels drawbacks 11

2.1.6 AHSS applications 12

2.2 Material Characterization tests 13

2.2.1 Uniaxial tensile test 13

2.2.2 Cyclic Loading-Unloading tensile tests 14

2.2.3 Nakajima Test 16

2.2.4 Tension-Compression Tests 17

2.2.5 U-shaped Bend Test 18
2.3 Constitutive Models 19
2.3.1 Quadratic Hill Yield Criterion 19
2.3.2 Barlat and Lian Yield Criterion 22
2.3.3 Isotropic Hardening Model 22
2.3.4 Kinematic Hardening Model 23
2.3.5 Combined Model 24
2.3.6 Yoshida-Uemori model 25
3. Methodology 29
3.1 Material Characterization 29
3.1.1 Chemical Composition 29
3.1.2 Uniaxial Tensile Tests 30
3.1.3 Cyclic Loading-Unloading Tensile Tests 31
3.2 Measurement Procedure 32
3.2.1 Nakajima and Notch Tensile Tests 32
3.2.2 U-shaped Bend test 35
3.3 Simulation Procedure 37
3.3.1 LS-DYNA Material Models 37
3.3.2 Nakajima Simulation 42
3.4 Notch Tensile test simulation 45
3.5 U-Shaped Bend test Simulation 46
4. Results and Discussion 49
4.1 Experimental Measurements 49
4.1.1 Nakajima Test 49
4.1.2 Notch tensile test 55
4.1.3 U-shaped bend test 56
4.2 Simulations 59
4.2.1 Identification of material parameters 59
4.2.2 Nakajima Simulations 64
4.2.3 Notch Tensile Test 69

4.2.4 U-Shaped Bend Test Simulation 69
5 Conclusions and Future Work 73
References 75
Appendix 77
A.1 U-shaped Bend Test Measurements 77
A.2 U-Shaped Bend Tests Simulation Results 81

List of Figures

Figure 1.1 - Projection of AHSS use per vehicle [3] 2

Figure 2.1 - HSS and AHSS families [5] 6

Figure 2.2 - DP steels microstructure [5] 8

Figure 2.3 - DP steels stress-strain curves [4] 8

Figure 2.4 - Instantaneous n-value vs engineering strain comparison between TRIP, DP and HSLA steel grades [8] 9

Figure 2.5 – Springback representation in stress-strain curve for HSS and mild steel [13] 11

Figure 2.6 - Springback after U-Shaped Bend Test for DP500, DP600 and DP780 [12] 12

Figure 2.7 - Steel types for different components of the car body structure [4] 12

Figure 2.8 - 2017 Kia Sportage body structure [1] 13

Figure 2.9 - DP steels engineering stress-strain curve. Adapted from [5] 14

Figure 2.10 - DP780 true stress-strain ULUL test [12] 15

Figure 2.11 - Evolution of elastic modulus degradation under different loading strategies [12] . 15

Figure 2.12 - Nakajima test setup [15] 16

Figure 2.13 - FLD for different DP steels [5] 17

Figure 2.14 - Loading paths of tensile test of notched planar specimen. Adapted from [16, 17] 17

Figure 2.15 - Stress-Strain curve for tension-compression test [19] 18

Figure 2.16 - Schematic of a U-shaped Bend test [20] 19

Figure 2.17 - Sheet withdrawn specimen in the rolling direction [10] 20

Figure 2.18 - Influence of the normal anisotropy coefficient [21] 21

Figure 2.19 - Isotropic Hardening scheme [24] 23

Figure 2.20 - Kinematic Hardening [24] 24

Figure 2.21 - Yield surface modifications in principal stress plane [25] 24

Figure 2.22 - Illustration of a two-surface model [26] 25

Figure 2.23 - Elastic Modulus decrease in a Uniaxial Load-Unload cyclic test [12] 27

Figure 2.24 - Side-wall curl after springback [27] 27
Figure 3.1 - True stress-strain curve for DP 1000 and DP1200 30
Figure 3.2 - Engineering stress-strain curve for cyclic loading-unloading test 31
Figure 3.3 - Nakajima specimen: (a) Sheet marking (b) Schematic of the measurement procedure 32
Figure 3.4 - Specimen dimensions: a) Notched tensile test specimen b) Nakajima test specimen 33
Figure 3.5 - Measurement methodology for springback quantification of a U-shaped bend test specimen 35
Figure 3.6 - Blank section after the test and before springback 36
Figure 3.7 - Elastic Plastic behaviour described by MT 3 [30] 38
Figure 3.8 - Fitting of bound stress curve [31] 41
Figure 3.9 - Fitting of reverse bound stress curve [31] 41
Figure 3.10 - Determination of parameter C [31] 42
Figure 3.11 - Nakajima Test Simulation model 43
Figure 3.12 - Flowchart of the Nakajima simulation methodology 45
Figure 3.13 - Meshed specimen for notch tensile test simulation 46
Figure 3.14 - U-shaped bend test simulation setup 47
Figure 3.15 - U-bend test simulation methodology 47
Figure 4.1 - W80 loading path for DP1000 50
Figure 4.2 - W70 loading path for DP1000 50
Figure 4.3 - W60 loading path for DP1000 51
Figure 4.4 - W55 loading path for DP1000 52
Figure 4.5 - W40 loading path for DP1000 52
Figure 4.6 - W20 loading path for DP1000 53
Figure 4.7 - Nakajima results for DP1000 steel 54
Figure 4.8 - Nakajima test results for DP1200 steel 54
Figure 4.9 - Notch tensile tests loading paths for DP1000 steel 55
Figure 4.10 - True Stress vs Plastic Strain curve with MT3 59
Figure 4.11 - True stress vs plastic strain with Ludwik-Hollomon equation 61
Figure 4.12 - Curve Fitting for Material Type 125 63

Figure 4.13 – DP1000 Nakajima simulation results for W80 loading path 64
Figure 4.14 – DP1000 Nakajima Simulation Results for W60 loading path 65
Figure 4.15 – DP1000 Nakajima test simulation results for W40 loading path 65
Figure 4.16 – DP1000 Nakajima simulation results for W20 loading path 66
Figure 4.17 - DP1200 Nakajima simulation results for W80 loading path 67
Figure 4.18 - DP1200 Nakajima simulation results for W60 loading path 67
Figure 4.19 - DP1200 Nakajima simulation results for W40 loading path 68
Figure 4.20 - R25 Notch Tensile test simulation for DP1000 69
Figure 4.21 - Sidewall curl after springback with 10P30 setup for DP1000 steel 70
Figure 4.22 - Opening angle after springback with 10P30 setup for DP1000 steel 70
Figure A.0.1 - Sidewall curl after springback with 12P30 setup for DP1000 81
Figure A.0.2 - Opening angle after springback with 12P30 setup for DP1000 81
Figure A.0.3 - Sidewall curl after springback with 10P60 setup for DP1000 82
Figure A.0.4 - Opening angle after springback with 10P60 setup for DP1000 82
Figure A.0.5 - Sidewall curl after springback with 12P60 setup for DP1000 83
Figure A.0.6 - Opening angle after springback with 12P60 setup for DP1000 83

List of Tables

Table 3.1 - DP1000 Chemical Composition 29

Table 3.2 - DP1200 Chemical Composition 29

Table 3.3 - Anisotropy coefficients for DP1000 and DP1200 31

Table 3.4 - Specimen dimensions of the Notched tensile tests 34

Table 3.5 - Specimen dimensions of the Nakajima tests 34

Table 3.6 - Number of tested specimens with the notch tensile test 34

Table 3.7 - Number of tested specimens with Nakajima test 35

Table 3.8 - Specimen dimensions: U-shaped bend test 36

Table 3.9 - Punch displacement in the Nakajima test and Simulation 44

Table 4.1 - Mean and standard deviation of the U-shaped bend tests specimen's measurements for DP1000 57

Table 4.2 - Influence of the punch and die radiuses in DP 1000 springback 57

Table 4.3 - Influence of the sheet thickness in DP1000 springback 58

Table 4.4 - Mean and standard deviation of the U-shaped bend tests specimen's measurements for DP1200 58

Table 4.5 - Material Type 3 parameters 60

Table 4.6 - Material Type 18 parameters 60

Table 4.7 - Material Type 36 parameters 61

Table 4.8 - Material Type 37 parameters 62

Table 4.9 - Material Type 103p parameters 62

Table 4.10 - Material Type 125 parameters 64

Table A.1 - 10P30R02 measurements of DP1000 steel 77

Table A.2 - 10P30R10 measurements of DP1000 steel 77

Table A.3 - 12P30R02 measurements of DP1000 steel 78

Table A.4 - 12P30R10 measurements of DP1000 steel 78

Table A.5 - 10P60R02 measurements of DP1000 steel 78

Table A.6 - 10P60R10 measurements of DP1000 steel 79

Table A.7 - 12P60R02 measurements of DP1000 steel 79

Table A.8 - 12P60R10 measurements of DP1000 steel 79

Table A.9 - 10P30R10 measurements of DP1200 steel 80

Table A.10 - 10P60R10 measurements of DP1200 steel 80

Table A.11 - Sidewall curl and opening angle after springback with 10P30R10 and 10P60R10 setups for DP1200 84

List of Symbols and Abbreviations

AHSS	Advanced High Strength Steels
CP	Complex Phase
DP	Dual-Phase
HSLA	High Strength Low Alloy
HSS	High Strength Steels
MS	Martensitic Steel
MT	Material Type
TRIP	Transformation-Induced Plasticity
ULSAB	Ultra-Light Steel Auto Body
UTS	Ultimate Tensile Strength
ULUL	Uniaxial Loading-Unloading-Loading
BLUL	Biaxial Loading-Unloading-Loading
TPB	Three-Point Bending
FLD	Forming Limit Diagram
σ	Stress [MPa]
K	Strength coefficient [MPa]
n	Strain hardening exponent
r	Anisotropy coefficient
Δr	Planar anisotropy coefficient
$\bar{r}$	Normal anisotropy coefficient
α_{ij}	Back-stress tensor [MPa]
F, G, H, L, M and N	Quadratic Hill Yield Criterion constants
ε	Strain

r_i	Lankford Coefficient
a, c, h and p	Barlat and Lian Yield Criterion constants
σ_{ij}	Stress tensor [MPa]
K	Hardening parameter [MPa]
f	Yield surface
F	Bounding surface
s	Cauchy stress deviator [MPa]
Y, σ_y	Yield tensile strength [MPa]
β	Centre of the bounding surface
B	Size of the bounding surface [MPa]
α_*	Relative kinematic motion
b, m, C	Material parameters of the Yoshida-Uemori model
R	Isotropic hardening parameter, Notch radius [mm]
D^P	Plastic deformation rate
R_{sat}	Saturated value the isotropic hardening stress at infinite plastic strain [MPa]
E_{av}	Average Young's modulus [MPa]
E_0	Initial Young's modulus [MPa]
E_a	Saturated value of Young's modulus [MPa]
R	Sidewall curl radius [mm]
θ_w	Opening angle [º]
β'	MT3 hardening parameter
E_p	Plastic hardening modulus [MPa]
E_t	Tangent modulus [MPa]
E	Young's modulus [MPa]

1. Introduction

1.1 Motivation

Air pollution represents one of the biggest problems that humanity needs to address. The greenhouse effect is an important and sensitive phenomenon that supports the different ecosystems on Earth. This phenomenon is being disturbed by human-induced greenhouse gases, carbon dioxide being the one emitted in greater quantity into the atmosphere.

Since vehicle emissions represent a large source of air pollutants, global legislators have passed more stringent regulations towards the automotive industry. The increase of safety regulations, also challenged the automakers to improve the car body structure, increasing passenger safety and car crash performance. So, the automotive industry's challenge is to improve vehicle safety while simultaneously reducing emissions. Corresponding to the safety regulations could be as simple as adding more safety components, however, this only meets one side of the problem [1].

A careful material selection can meet the two ends of the problem by using stronger materials that allow thinner structural components, leading to a vehicle weight reduction and improvement of vehicle fuel consumption. However, there are many factors that must be taken into account in material selection for automotive applications, such as safety, fuel efficiency, environmentalism, manufacturability, durability, quality, and cost [1].

The steel industry responded with the development of a new steel family called Advanced High Strength Steels (AHSS). These are known for having higher yield and ultimate tensile strengths than conventional High Strength Steels (HSS) without compromising ductility, which allows the development of more resistant structural components. This leads to weight reduction due to the possibility of using thinner sheet steels that can meet the safety requirements. In the light of these advantages, AHSS steels have been extensively used in the automotive industry, particularly Dual-Phase (DP) steels, as illustrated in Figure 1.1 [2].

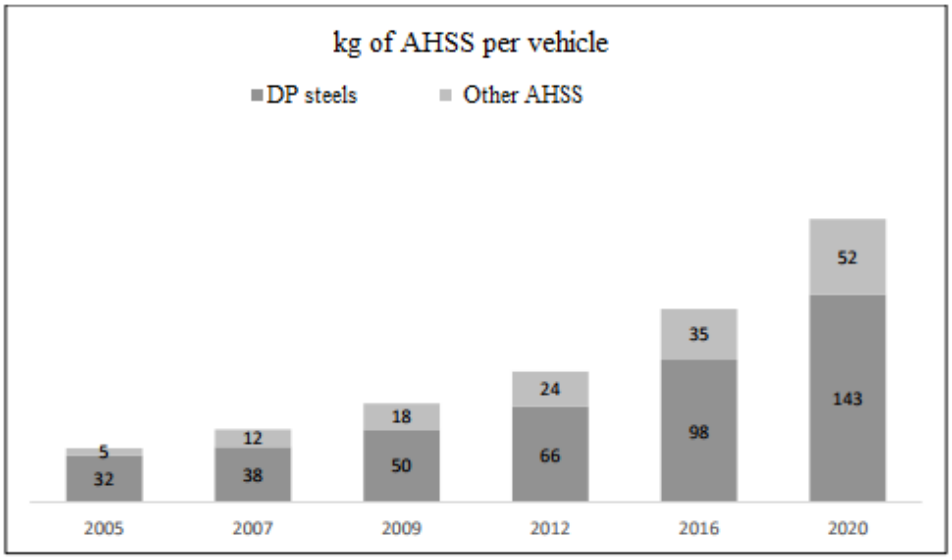

Figure 1.1 - Projection of AHSS use per vehicle [3]

With the purpose of investigating and develop a new methodology for AHSS tool design, the company MCG mind for metal started the ULTRAFORMING project. The project was carried out within a partnership between MCG's research and development unit, and a UNIDEMI research team from FCT-UNL, which instigated a doctoral study and three master dissertations, including this one. The main goals were to research and develop new constitutive models for AHSS elastic--plastic behaviour, research and develop new simulation models that can fit in AHSS tool designs and develop a good practice guide for tool design and AHSS stamped parts. Thus, this dissertation has a contribution to the final stages of the ULTRAFORMING project to continue this study.

1.2 **Objectives**

The present dissertation aims to continue the study of Dual-Phase DP1000 and DP1200 steels, using the experimental work performed in earlier stages of the ULTRAFORMING project as the basis to study and validate constitutive material models.

For that effect, the material characterization test results must be analysed, and measurement and simulations methodologies must be studied and implemented. Through FEM simulations, the validation of material models is separated into two parts, the strain path characterization under different loading paths and springback prediction.

1.3 **Structure**

The present document divides the work done for this dissertation in five main chapters. This first chapter describes the motivation, the objectives, and the respective document structure.

The second chapter is a review of the first AHSS steels generation with emphasis to DP steels, material characterization tests that were previously performed in earlier stages of the project and others that are used to obtain material parameters, and some of the most popular constitutive material models that have the purpose of describing AHSS behaviour.

In the third chapter, the methodologies used in this work for the specimen's measurement of the U-shaped bend, Notch tensile and Nakajima tests, the identification of material parameters for different material models, and the simulation procedure are described in detail.

The fourth chapter presents the results of this work following the methodologies described in the third chapter. The simulations are analysed and compared with the experimental data.

In the fifth and final chapter, all the conclusions obtained from this dissertation are presented, with suggestions for future work to improve and continue this study.

2. Literature Review

2.1 Advanced High Strength Steels

As referred to in the introduction, the increasing requirements for passenger safety and fuel consumption have made the automotive industry to look for lighter and stronger materials, to build car body structural components. Thus, in 1975 a strong competition between steel and low-density metal industries began [2].

To face the competition, in 1994 the steel industry made a consortium of 35 sheet steel producers and began the Ultra-Light Steel Auto Body (ULSAB) program with the aim of design lighter car body structures. From this program, the AHSS steel family emerged. As opposed to the conventional HSS in which ductility decreases with strength, AHSS steels are known for having high strength without compromise ductility. These steels derive their good mechanical properties from multi-phase complex microstructures, that allows the material to retain the characteristics from different phases. The main difference between HSLA (High Strength Low Alloy) steels and AHSS is that the HSLA exhibit a single-phase ferrite microstructure [2, 4]

There are two distinct generations of AHSS family, the first generation possesses a ferrite-based microstructure while the second is known as austenitic steels. As illustrated in Figure 2.1, the mechanical properties of AHSS steels cover a wide range of strength and ductility This allows the production of various parts that can meet the requirements of different areas of the car body structure, achieving a more efficient material usage [4, 5].

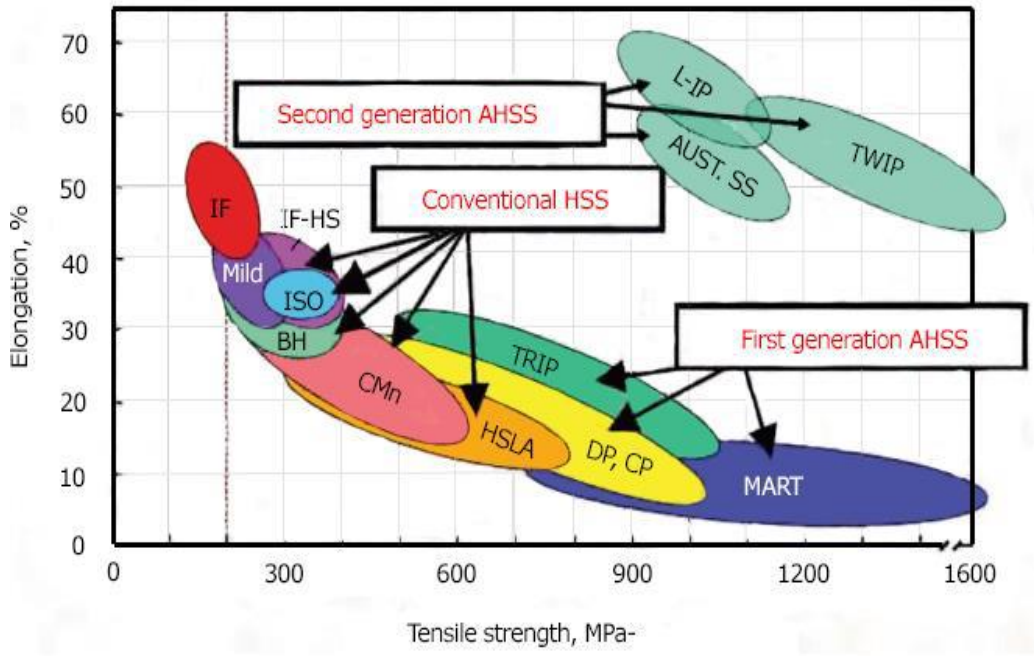

Figure 2.1 - HSS and AHSS families [5]

2.1.1 Transformation-Induced Plasticity Steels

TRIP (Transformation-Induced Plasticity) steels have a dispersed multi-phase microstructure composed by a ferrite matrix, bainite, retained austenite (at least 5 percent) and martensite. As can be seen in Figure 2.1, the range covered by TRIP steels of strength and ductility is very similar to DP and CP (Complex Phase) steels, although TRIP steels endure higher values of elongation. This is due to the presence of retained austenite in the microstructure. During plastic deformation, austenite turns into hard martensite which allows a high hardening rate causing the resultant microstructure to be toughened by the hard martensite. Due to this transformation, the steel is capable of enduring high strain levels, and therefore reaches higher values of elongation [1, 2].

The high work hardening rate make these steels good for stamping applications, high energy absorption under strain results in a high level of crash energy absorption and excellent durability is suitable for parts that are subjected to high load cycles.

2.1.2 Complex Phase Steels

Like TRIP steels, CP steels have a multi-phase microstructure, however, CP steels typically do not have retained austenite in the microstructure. The microstructure is composed of a mixed ferritic-bainitic matrix with bits of martensite and pearlite. The reason why CP steels have high yield strength and high elongation at tensile strengths (like DP steels), is the fine microstructure that characterizes this steel grade. The small grains in the microstructure causes a good edge stretchability, the high ultimate tensile strength and residual deformation capability result in a high energy absorption and resistance to deformation which is good for car safety parts. Due to decreased formability at higher strengths, the local necking may cause a quick and localized cracking [1, 2].

2.1.3 Martensitic Steels

The steel that provides the highest UTS (ultimate tensile strength), in the first generation of AHSS, is the MS (Martensitic Steel) steel with values between 900 to 1700 MPa. This extremely high strength is due to a quenching process after hot rolling (or annealing), where almost all austenite is transformed into martensite. The resulting microstructure is composed by a martensite matrix with a small amount of ferrite and bainite phases. Despite the highest UTS, MS steels exhibit the lowest elongation. So, MS steels are often subjected to post-quenching tempering with the aim of improving ductility and formability. Due to the high UTS, these steels allow the production of strong and light-weight components but with the limitations of low elongation and high springback effects [2].

2.1.4 Dual-Phase Steels

The Dual-Phase term is referred to AHSS steel grades that are composed by two distinct phases. The DP steels microstructure is based on a soft ferrite matrix filled with martensite islands (typically from 10 to 40 percent), as illustrated in Figure 2.2. This type of microstructure allows the steel to hold a UTS between 500 and 1200 MPa. [2].

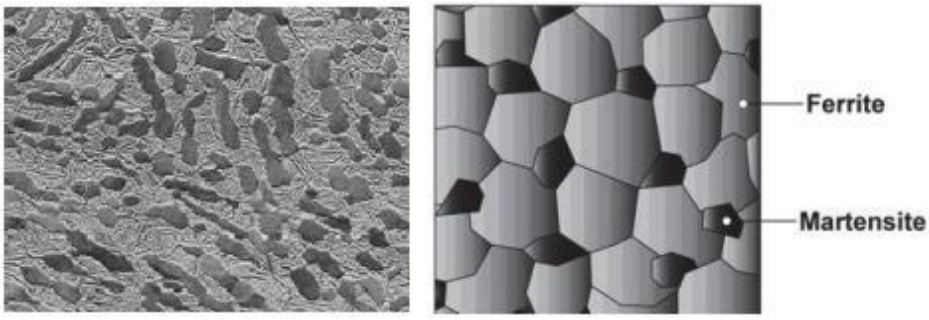

Figure 2.2 - DP steels microstructure [5]

Using these two phases, one can obtain a good balance between high strength and ductility. The martensitic phase is responsible for the material's strength, due to the martensite islands acting as an obstacle to the material dislocations (during deformation). As the percentage of martensite increases in the ferrite matrix, the steel achieves higher UTS, as illustrated in Figure 2.3. The common designation for Dual-Phase steels is presented with the initials DP followed by the yield and ultimate tensile strengths. For instance, in Figure 2.3 DP500/800 is referred to a Dual-Phase steel which the yield and ultimate tensile strengths are 500 MPa and 800MPa, respectively. The martensitic phase can also be an important factor when it comes to the material durability since the martensite islands can delay a possible crack propagation. The ferritic phase isolates the martensitic islands, being responsible for the material's ductility and formability [6].

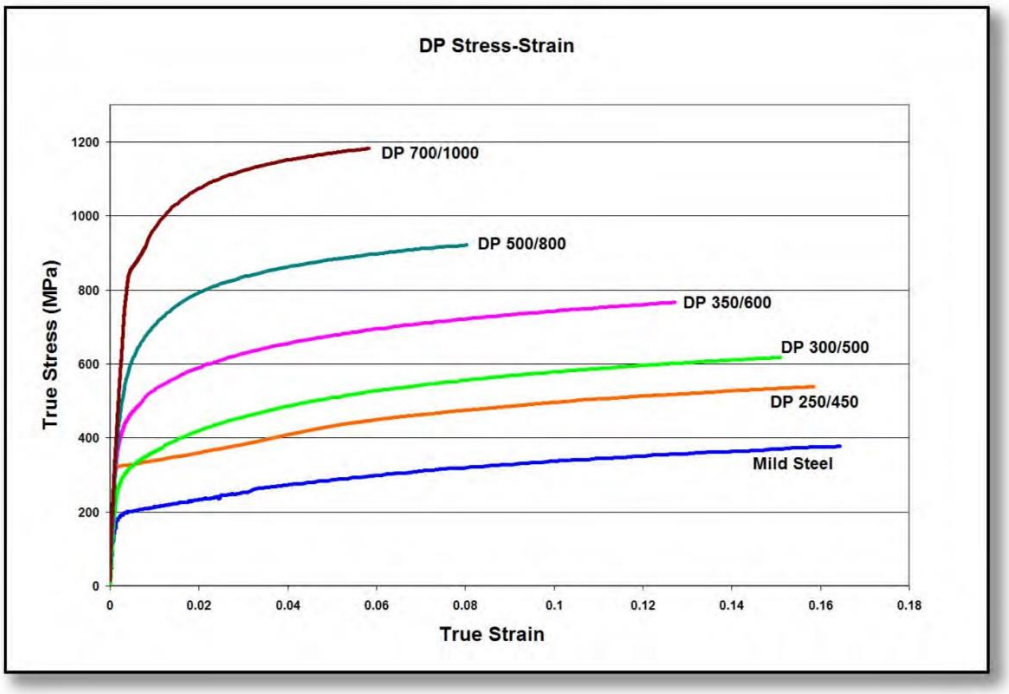

Figure 2.3 - DP steels stress-strain curves [4]

As Figure 2.3 shows, DP steels exhibit a high initial strain hardening when compared to mild steel, and an absence of an exact yield tensile strength. A justification for the continuous yielding behaviour could be the presence of induced mobile dislocations in the ferritic matrix that result in the elimination of yield point elongation. These mobile dislocations can also be the reason for the high work hardening rate. The finely dispersed martensite grains interact with these dislocations, resulting in high strain hardening, meaning that the plastic deformation and the hardening phenomenon occur around the martensitic islands [7].

Mild steel exhibits a constant strain hardening rate that can be described by the very popular Ludwik-Hollomon hardening rule, represented by equation (2.1). DP steels do not exhibit this behaviour, instead, when plastic deformation occurs, the material presents a high initial hardening rate that, after a certain amount of plastic strain, starts to decrease to a constant value.

$$\sigma = K \times \varepsilon^{n} \tag{2.1}$$

where K [MPa] is the strength coefficient and n is the hardening exponent, known as the n-value.

Ludwik-Hollomon model considers the n-value as a constant, but in AHSS steels there is variation in the strain hardening behaviour. This is mainly due to the multi-phase microstructure and the phase transformations during deformation. Since n is not constant, the Ludwik Hollomon rule may not be valid for simulation purposes, regarding AHSS steels behaviour. Figure 2.4 illustrates the n-value evolution through engineering strain for a DP, TRIP and HSLA steels. It can be noticed the characteristic behaviour of the DP steel [8].

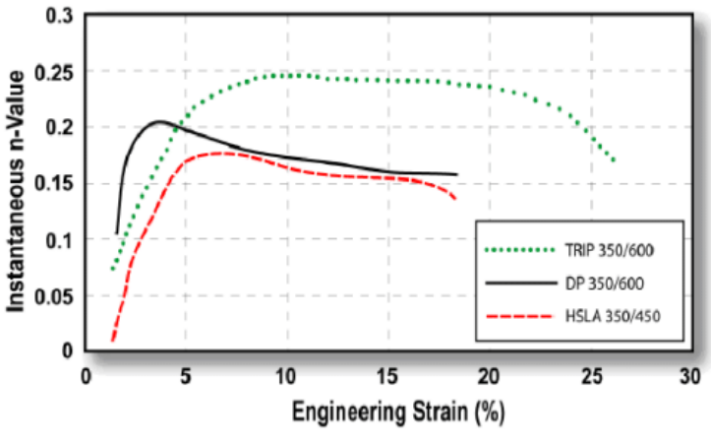

Figure 2.4 - Instantaneous n-value vs engineering strain comparison between TRIP, DP and HSLA steel grades [8]

When it comes to DP steels manufacturing, an important aspect that must be considered is the transformation of austenite into martensite. The addition of alloying elements like Carbon (C), Manganese (Mn), Silicon (Si), etc. helps stabilizing this process. [2].

DP steel sheets are produced by annealing low carbon steels into the inter-critical temperature range to form a mixed ferrite-martensite microstructure, followed by a rapid cooling to transform austenite into martensite [9]. This microstructure can be developed through a hot rolling process or in a cold rolled sheet material [2].

After the hot rolling process, there are two alternatives, one is to start a cooling stage where the amount of ferrite is obtained from the austenite transformation, while the other one is to accelerate the cooling process, to the lowest stability temperature, followed by a slow cooling. This will allow the austenite to decompose into ferrite. Austenite transformation in the ferritic phase allows the carbon content enrichment in the remaining austenite, increasing its hardenability. The two alternatives now converge to the final step that consists in a rapid cooling rate to entirely transform the remaining austenite into martensite [2].

The DP microstructure can also be obtained by cold rolling. Starting with a continuous annealing process, where the sheet is heated up to a temperature between 730ºC and 760ºC. At this point, 15% of the microstructure, that is composed of ferrite and perlite, transforms into austenite. After this, the sheet is quenched and the austenite transform in martensite resulting, therefore, a ferritic-martensitic microstructure [2].

The use of rolling processes induces crystallographic structure orientations, leading to a sheet steel with anisotropic behaviour. This means that the sheet steel will exhibit a different tensile strength when subjected to loads in different directions [10].

After plastic deformation, DP steels exhibit a reduction of the elastic modulus. This decrease has shown to be greater in small plastic strains and tends to an asymptotic value. DP steels that have a greater UTS (more martensite percentage) show a greater decrease in Young's modulus. The work of Hyunjin Kim et. al [11] show some interesting conclusions and interpretations for the elastic modulus degradation. The author states that the residual stress increases with deformation, disturbing elastic recovery causing a decrease in the elastic modulus. Another conclusion is that the accumulation of dislocations that move along the slip plane, while the front dislocations are stopped by grain boundaries. Many of these dislocations are repulsive to each other and are kept together by the applied stress. When the stress drops, the dislocations re-establish their previous equilibrium spacing with associated strain and an apparent degradation on elastic modulus [10, 11].

2.1.5 Dual-Phase steels drawbacks

DP steels are the most used AHSS steel grade used in the automotive industry. The search for stronger DP steels had one major drawback, the springback phenomenon. Springback occurs after a forming process, where the material “tries” to recover its original state, hence being called springback. Al Azraq et al. [13] stated that this phenomenon is proportional to the yield tensile strength, as schematicically represented in Figure 2.5, DP steels with higher UTS have shown to exhibit larger springback phenomenon [14].

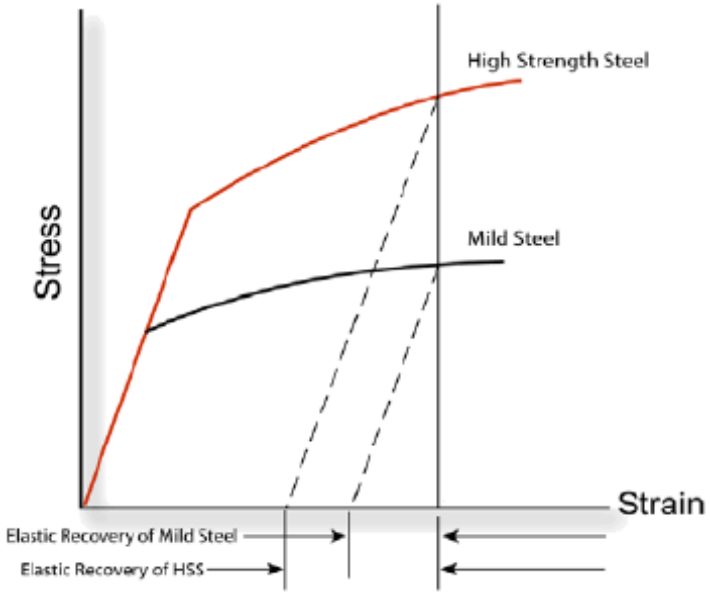

Figure 2.5 – Springback representation in stress-strain curve for HSS and mild steel [13]

Figure 2.5 illustrates the springback phenomenon in a stress-strain curve, however, it does not represent the problem in stamping applications. For instance, Figure 2.6 shows the springback for three types of DP steels after a U-shaped Bend test. When it comes to the car body structure design, the parts that need to be assembled with each other must have specific dimensions. To obtain these parts, one must understand the springback phenomenon and how to deal with it.

In the U-shaped bend test, the springback phenomenon is significantly affected by the test setup. The blank holder load, punch and die radiuses, and sheet thickness are some of the parameters that can be changed to reduce the springback. For instance, smaller punch and die radiuses lead to a lower springback response.

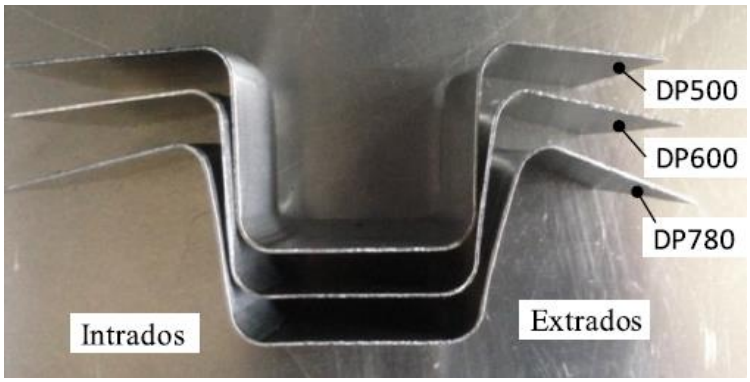

Figure 2.6 - Springback after U-Shaped Bend Test for DP500, DP600 and DP780 [12]

2.1.6 AHSS applications

As previously mentioned, automakers need to face challenges to meet safety and gases emissions regulations. The answer to this problem is in the material selection. Selecting higher--strength steels, one can reduce the structural component's thickness, leading to the vehicle's weight reduction and simultaneously improve passenger safety. To maximize efficiency, one must know which AHSS steel grade better suits at each structural component, in the car body structure. Figure 2.7 illustrates an analysis of which steel grade to use in different components of the same passenger compartment [4].

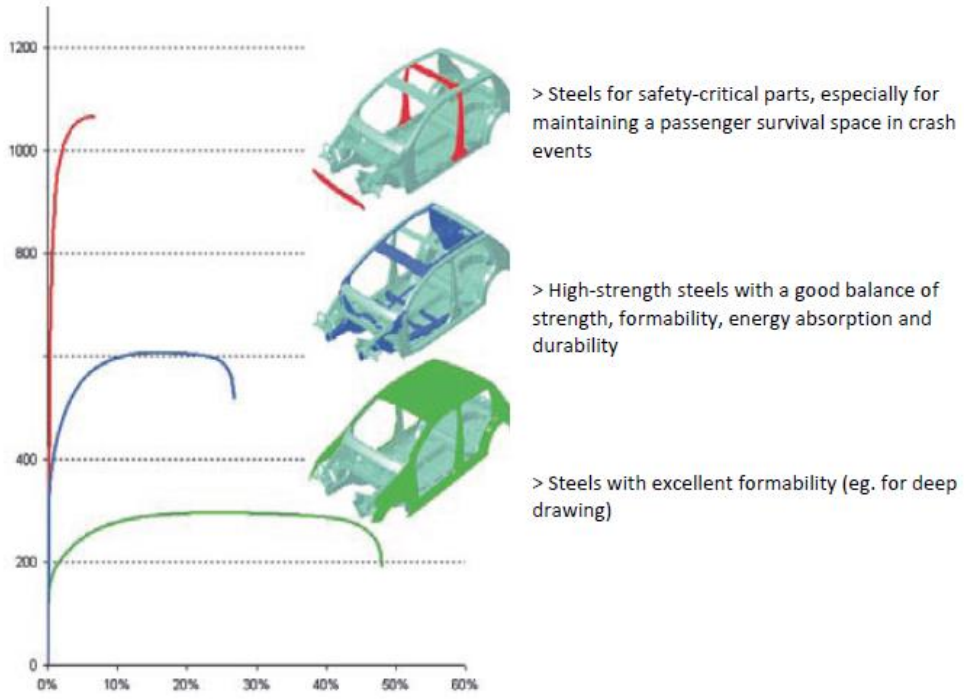

Figure 2.7 - Steel types for different components of the car body structure [4]

After the brief first AHSS generation steel grades description, one can easily connect the steel grade to the vehicle structural compartment. The red area would be an MS steel while the blue area could be a TRIP, CP or DP steel grade [4]. A good example of a direct application of this concept is the 2017 Kia Sportage (Figure 2.8), where 51% of his body structure is composed of AHSS steel [1].

Figure 2.8 - 2017 Kia Sportage body structure [1]

2.2 Material Characterization tests

This subchapter contains a review of the typical material characterization tests that are performed to understand the different materials behaviour. In this study it is important to know briefly the purpose of these tests since some of those were already performed in earlier stages of the project.

2.2.1 Uniaxial tensile test

The Uniaxial Tensile test is a universal mechanical test used to determine the essential mechanical properties of a material. The procedure goes through applying an increasing tensile load to the specimen, until fracture occurs. The output of this process is the well-known stress--strain curve that allows determining various mechanical properties, such as yield tensile strength,

ultimate tensile strength, elongation, etc. Figure 2.9 illustrates that with increasing strength the ductility decreases, but also that the elasto-plastic behaviour becomes more accentuated. This absence of an exact yield point elongation and the continuous yielding behaviour might be related to the presence of the martensitic islands in the ferrite matrix [10].

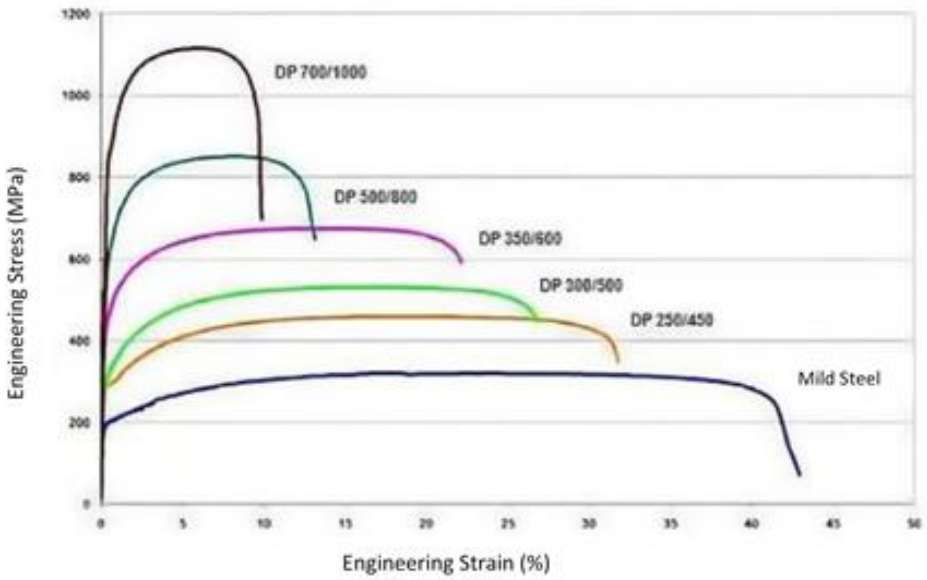

Figure 2.9 - DP steels engineering stress-strain curve. Adapted from [5]

2.2.2 Cyclic Loading-Unloading tensile tests

With increasing plastic strain, the Dual-Phase steel Young's modulus decreases. To observe this phenomenon, one must perform a cyclic load-unload tensile test. This test consists in loading the specimen to a certain amount of plastic strain followed by an unloading until zero stress. The process is repeated the desired number of times, as shown in Figure 2.10. When it comes to DP steels, the elastic modulus degradation follows a saturation curve. Therefore, when a certain value is reached the elastic modulus stops decreasing and becomes constant, as depicted in Figure 2.11 [12].

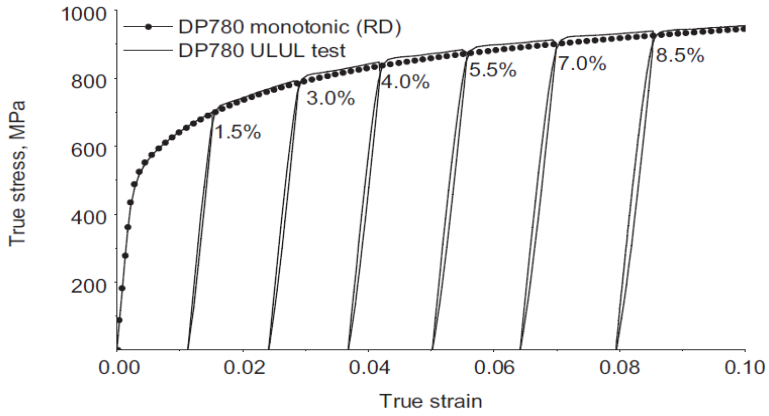

Figure 2.10 - DP780 true stress-strain ULUL test [12]

Xin Xue et al. [12] studied Young's modulus degradation dependency of loading paths. The use of three different cyclic loading-unloading tests shows a big difference in the reduction of the elastic modulus, as depicted in Figure 2.11. Making use of the three experimental tests ULUL (Uniaxial Loading-Unloading-Loading), BLUL (Biaxial Loading-Unloading-Loading) and TPB (Three-Point Bending), the authors performed three distinct springback simulations considering the behavior of the elastic modulus exhibited in the different loading strategies. The results showed a slight difference in the final geometry of the simulated specimen, being the one that considered the TPB the more accurate.

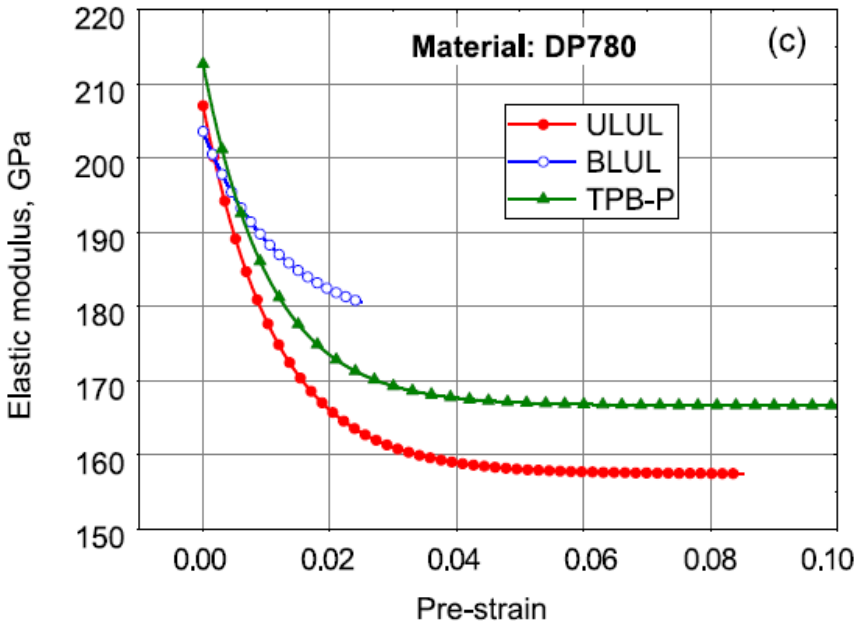

Figure 2.11 - Evolution of elastic modulus degradation under different loading strategies [12]

2.2.3 Nakajima Test

The FDL (Forming Limit Diagram) is a very important tool in the steel manufacturing industry that uses processes based on plastic deformation. This diagram is crucial to analyze the sheet steel formability. In stamping applications, the material can be subjected to a wide range of loading paths that can be studied with the FDL. As can be seen in Figure 2.8, the AHSS structural components of the car body structure, are submitted to stamping processes. An example of forming limit curves of DP steels is illustrated in Figure 2.13. Due to the stronger DP steels having a greater martensite percentage and the ferrite being responsible for the material ductility and formability, stronger DP steels have lower formability [5, 10].

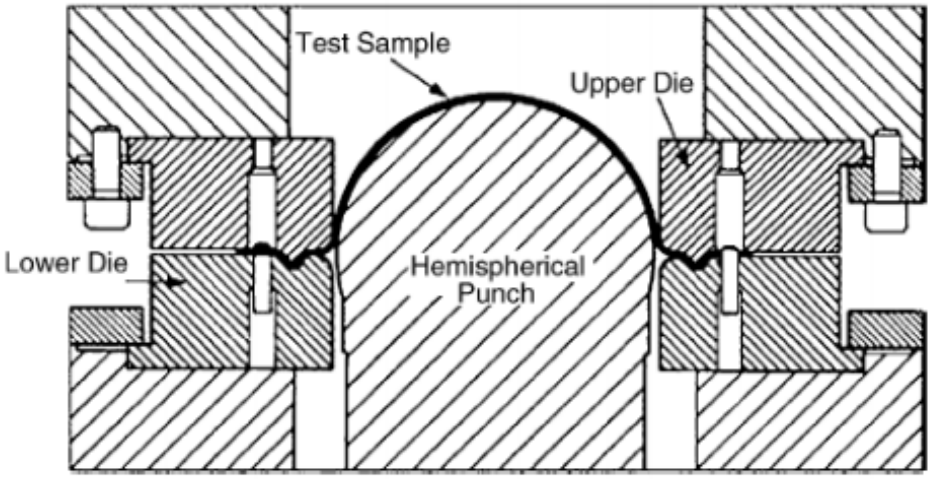

Figure 2.12 - Nakajima test setup [15]

To create this diagram, it is necessary to perform mechanical tests that subjects the material in different load paths. The Nakajima test enables the material to experience various loading paths by varying the specimen's width, allowing the material to flow in different strain paths, as shown in Figure 2.14 (b). The Nakajima test consists in stretching the material with the action of a hemispherical punch, until fracture occurs. Since the specimen is constrained at the edges the material is subjected to severe stretching. A schematic of the Nakajima test setup is presented in Figure 2.12 [15].

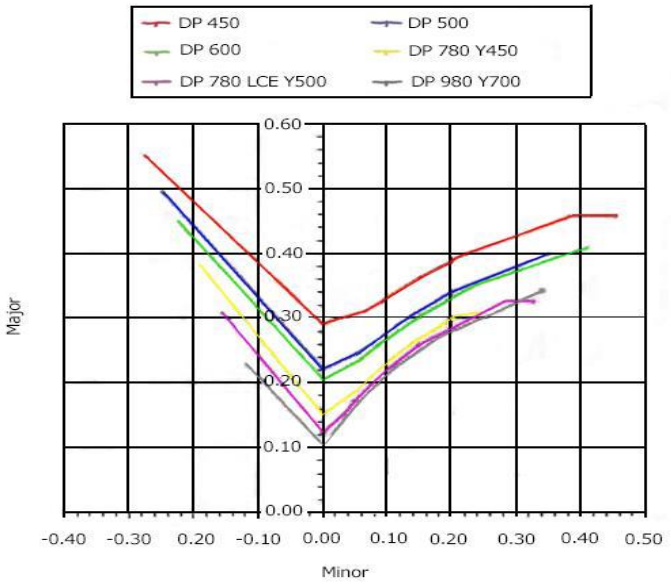

Figure 2.13 - FLD for different DP steels [5]

To capture loading paths between uniaxial stretching and plane deformation state ($\varepsilon_{II} = 0$), the use of tensile tests with notched planar specimens can also be performed [16]. A schematic of how this test fits in the FDL is illustrated in Figure 2.14 (b).

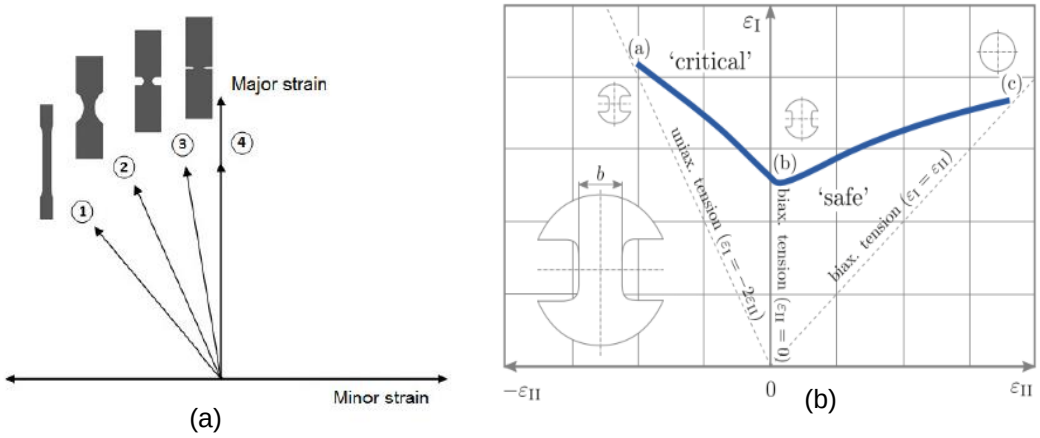

Figure 2.14 - Loading paths of tensile test of notched planar specimen. Adapted from [16, 17]

2.2.4 Tension-Compression Tests

There are many plastic deformation processes in the steel industry where the material is submitted to cyclic tension-compression loads. For instance, U-Shaped Bend tests are used for validation of constitutive models when it comes to springback prediction. In this test, the sheet is

submitted to cyclic tension compression loads, and constitutive models that describe the Bauschinger effect, have shown to be more accurate. When a material is loaded (and plastically deformed) followed by an unloading, to zero stress, there will remain residual stresses between the material grains. If the same material is now loaded in the opposite direction, the entrance in plastic deformation will be influenced by the residual stresses. This is called the Bauschinger effect [10].

The characterization of the stress-strain curve with the tension-compression test, is very important in constitutive models that incorporate kinematic hardening. The Transient Bauschinger effect (causing an early re-yielding), the work hardening stagnation and permanent softening are phenomena that can be observed with this test (Figure 2.15) [18].

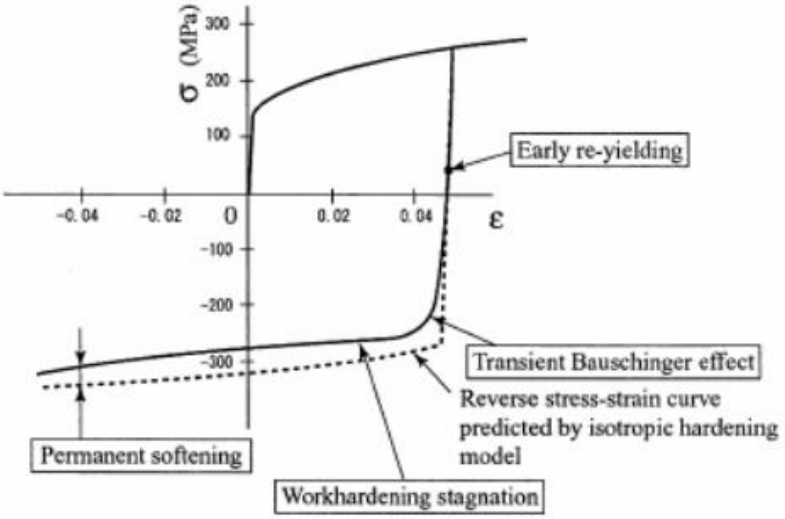

Figure 2.15 - Stress-Strain curve for tension-compression test [19]

2.2.5 U-shaped Bend Test

The U-shaped Bend test is commonly used to study the springback phenomenon, more specifically, for validation of material constitutive models. This test consists in applying a certain displacement in the punch, bending the specimen until the cross section shows a U-shaped geometry. A schematic of this test is shown in Figure 2.16. After this test, the sheet will exhibit springback, and as previously mentioned stronger DP steels tend to have higher springback effects, as illustrated in Figure 2.6. This test also allows to study the influence of stamping parameters in springback, such as blank holder load, punch radius, etc.

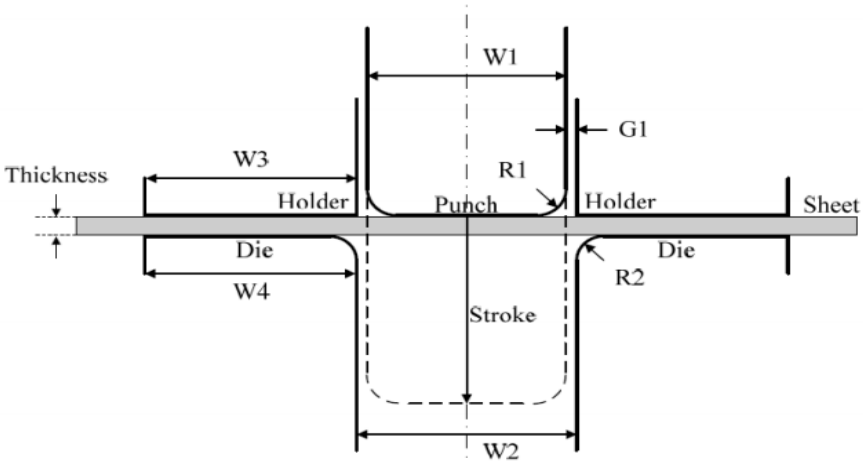

Figure 2.16 - Schematic of a U-shaped Bend test [20]

2.3 Constitutive Models

As previously mentioned, DP steels present high springback after plastic deformation. One way of dealing with this problem is to vary the parameters that influence the springback (like punch and die radiuses, sheet thickness, etc.) and perform experimental test until the desired part geometry is obtained. This is a high-cost method, since the new tools must be designed for new test setups. Also, it results in a great waste of raw material.

The other way to face this issue is through simulation. With accurate constitutive material models that can describe the material behaviour accurately and describe the springback phenomenon, one can reduce significantly the tool adjustments and material waste.

2.3.1 Quadratic Hill Yield Criterion

In 1948, Hill developed a yield criterion that considers orthotropic anisotropy states. For an arbitrary anisotropy state where the principal anisotropy and global axis coincide, the Hill criterion is represented by the following equation [10]:

$$F(\sigma_y - \sigma_z)^2 + G(\sigma_z + \sigma_x)^2 + H(\sigma_x - \sigma_y)^2 + 2L\tau_{yz}^2 + 2M\tau_{zx}^2 + 2N\tau_{xy}^2 = 1 \qquad (2.2)$$

Where F, G, H, L, M and N are constants that characterize the anisotropy state.

The sheet anisotropy state can be characterized through uniaxial tensile tests, with the specimens withdrawn from different directions in the sheet plane. For instance, with the specimen represented in Figure 2.17, it is possible to obtain the anisotropy coefficient (r), also known as Lankford coefficient. This coefficient is obtained by the quotient between specimen's width (ε_w) and thickness (ε_h) true strains:

$$r = \frac{\ln\left(\frac{w}{w_0}\right)}{\ln\left(\frac{h}{h_0}\right)} = \frac{\varepsilon_w}{\varepsilon_h} \tag{2.3}$$

where h_0, w_0, h, w [mm] are, respectively, the initial thickness and width, the instantaneous thickness and width.

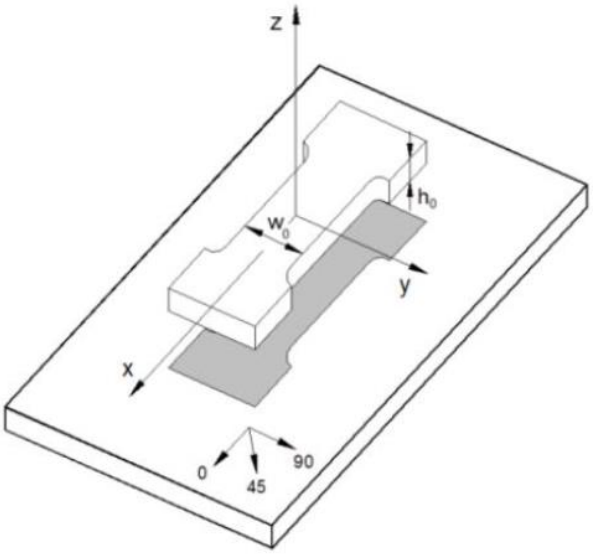

Figure 2.17 - Sheet withdrawn specimen in the rolling direction [10]

If the Lankford coefficients in the 3 directions are known, one can determine the Hill's yield criterion constants:

$$H = \frac{r_0}{1+r_0}; F = \frac{r_0}{(1+r_0)r_{90}}; N = \frac{(r_0+r_{90})(2r_{45}+1)}{2(1+r_0)r_{90}}; G = 1-H \tag{2.4}$$

The planar anisotropy coefficient Δr, quantifies the difference between the sheet properties in every 45 degrees direction. For instance, if $\Delta r = 0$, the sheet has the same r value in every direction [10]. This coefficient can be calculated by the following expression:

$$\Delta r = \frac{r_0 + r_{90} - 2r_{45}}{2} \tag{2.5}$$

In stamping application, materials that have a high normal anisotropy coefficient ($\bar{r}$) are appreciated since present a higher resistance to thickness reduction and fracture. This is mainly because the normal anisotropy increases the material's strength through thickness:

$$\bar{r} = \frac{r_0 + 2r_{45} + r_{90}}{4} \tag{2.6}$$

The influence of this coefficient on the shape of the yield function is illustrated in Figure 2.18.

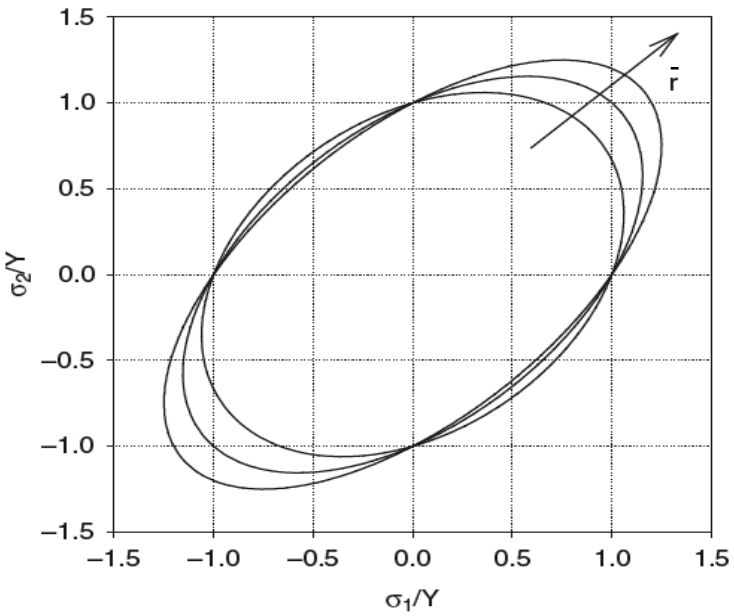

Figure 2.18 - Influence of the normal anisotropy coefficient [21]

High values of the normal anisotropy coefficient, $\bar{r}$, indicate a high resistance to thickness reduction and, therefore, a higher strength in biaxial stress states. That is appreciated in stamping applications, where the fracture and/or necking typically occur where biaxial stress states take place, for instance, the areas in contact with the bottom and the edge of the punch [10].

2.3.2 Barlat and Lian Yield Criterion

Barlat and Lian [22], in 1989, proposed a yield function that describe the orthotropic behavior of sheet metals under full plane stress state. In addition, it gives an approximate representation of polycrystalline yield surfaces [22]. The yield function is given by:

$$a|k_1 + k_2|^M + a|k_1 - k_2|^M + c|2k_2|^M = 2\sigma_e^M \tag{2.7}$$

$$k_1 = \frac{\sigma_{xx} + h\sigma_{yy}}{2}; k_2 = \sqrt{\left(\frac{\sigma_{xx} - h\sigma_{yy}}{2}\right)^2 + p^2\tau_{xy}^2} \tag{2.8}$$

where a, c, h and p are material constants that can be obtained through the Lankford coefficients, like in Quadratic Hill yield criterion [22]:

$$c = 2\sqrt{\frac{r_0}{1+r_0} \cdot \frac{r_{90}}{1+r_{90}}}; a = 2 - c; h = \sqrt{\frac{r_0}{1+r_0} \cdot \frac{1+r_{90}}{r_{90}}} \tag{2.9}$$

The M parameter is a constant that depends in the crystallographic structure. For instance, a BCC (body-centered cubic) material, such as a Ferritic-Martensitic steel (DP steels) [23], M takes the value of 6, according to the article referenced as [22].

2.3.3 Isotropic Hardening Model

Steels present a strain hardening phenomenon when the yield tensile strength is surpassed. If one only relies on yield surface (like von Mises criterion), the strain hardening cannot be represented. In this model, when the plastic deformation begins, the yield surface expands with increasing stress without changing its shape, as illustrated in Figure 2.19. Because the yield surface expanded, after unloading, the material has a new yield tensile strength, considering the material hardening. If reloading occurs the material now has a new tensile strength, which is important for metal forming simulations [24].

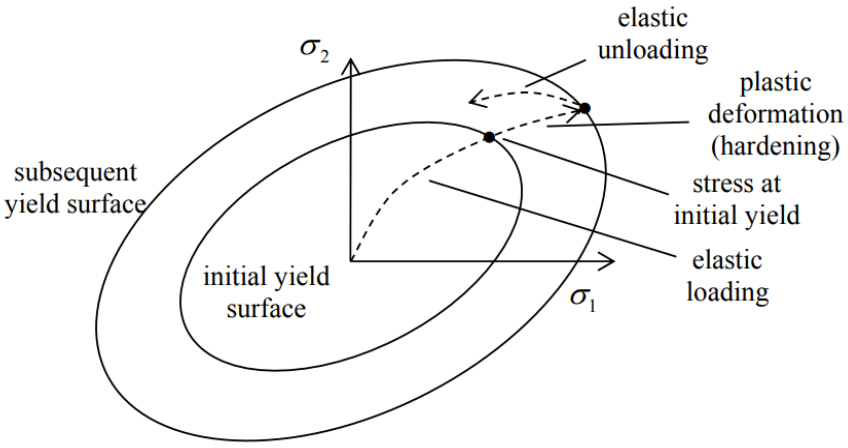

Figure 2.19 - Isotropic Hardening scheme [24]

The initial shape is specified by the initial yield function, $f_0(\sigma_{ij})$, and the changes in size are dependent of the hardening parameter K:

$$f(\sigma_{ij}, K_i) = f_0(\sigma_{ij}) - K = 0 \tag{2.10}$$

2.3.4 Kinematic Hardening Model

Although the isotropic hardening model does capture the hardening behavior, it implies that the yield strength in tension and compression are the same and remain equal as the yield surface increases with plastic strain. As previously mentioned, this does not happen due to the Bauschinger effect and strain softening, in reverse stress. So, to model the Bauschinger effect, one can use the Kinematic Hardening Model. The yield surface remains the same size and shape but translates in the stress space [24]. The yield function takes the general form:

$$f(\sigma_{ij}, K_i) = f_o(\sigma_{ij} - \alpha_{ij}) = 0 \tag{2.11}$$

The hardening parameter in this model, α_{ij}, is known as the back-stress tensor. This parameter is responsible for the translation of the yield surface (Figure 2.20).

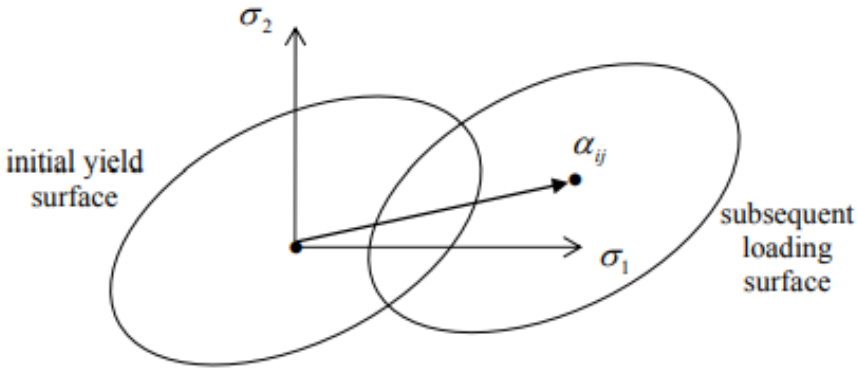

Figure 2.20 - Kinematic Hardening [24]

2.3.5 Combined Model

A combination of isotropic-hardening can also be used. The yield function both translates and expands with plastic strain. Figure 2.21 demonstrates how the yield surface would behave in a combined hardening scenario [24].

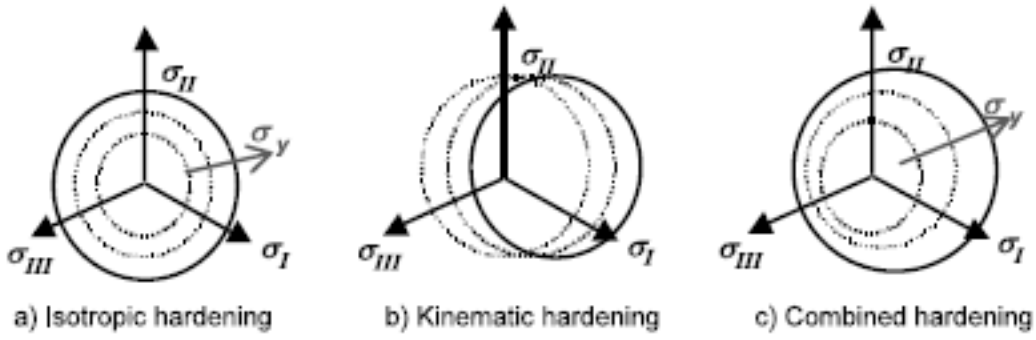

Figure 2.21 - Yield surface modifications in principal stress plane [25]

The general form of the yield function is more complex due to the presence of a hardening parameter and the back-stress tensor:

$$f(\sigma_{ij}, K_i) = f_0(\sigma_{ij} - \alpha_{ij}) - K = 0 \tag{2.12}$$

2.3.6 Yoshida-Uemori model

Yoshida et al. (2001) [18] proposed a constitutive model of large-strain cyclic plasticity. The current model is a two-surface model that assumes kinematic hardening for the yield surface within a bounding surface of combined isotropic-kinematic hardening, as illustrated in Figure 2.22 [18].

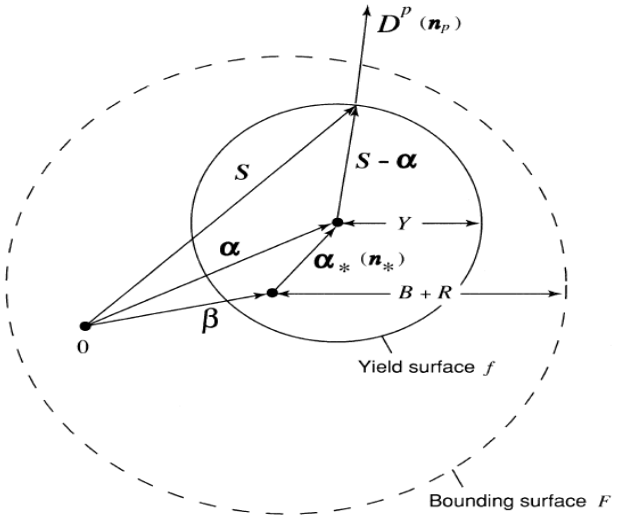

Figure 2.22 - Illustration of a two-surface model [26]

To describe the transient Bauschinger effect (characterized by an early re-yielding and the subsequent change of work hardening rate), the yield surface is modelled with a kinematic hardening rule. The global work hardening behaviour is described by the isotropic hardening in the Bounding surface. To capture the permanent softening and work hardening stagnation, the bounding surface is assumed to have a kinematic and a non-isotropic hardening behaviour [18].

The yield surface (f) and the bounding surface (F) are represented by the following equations (based on the von Mises criterion) [18]:

$$f = \frac{3}{2}(s-\alpha) : (s-\alpha) - Y^2 = 0 \tag{2.13}$$

$$F = \frac{3}{2}(s-\beta) : (s-\beta) - (B+R)^2 = 0 \tag{2.14}$$

where s is the Cauchy stress deviator, Y the yield tensile strength, β and B is the centre and the initial size of the bounding surface, respectively, and R the isotropic hardening component.

The relative kinematic motion (α_*) of the yield surface to the bounding surface is expressed by [18]:

$$\alpha_* = \alpha - \beta \tag{2.15}$$

$$\dot{\alpha_*} = C\left(\frac{2}{3} a\, D^p - \alpha_* \dot{p}\right);\ a = B + R - Y \tag{2.16}$$

where C is a material parameter that controls the kinematic hardening rate, D^p is the plastic deformation rate and $\dot{p}$ the effective plastic strain.

As previously mentioned, the bounding surface is modelled by a mixed isotropic-kinematic hardening. So, the isotropic and kinematic evolution of the bounding surface is given by the equations (2.17) and (2.18) respectively:

$$\dot{R} = m(R_{sat} - R)\dot{p} \tag{2.17}$$

$$\dot{\beta} = m\left(\frac{2}{3} b D^p - \beta \dot{p}\right) \tag{2.18}$$

Where m is a material parameter that controls the rate of isotropic hardening, b is a material parameter and R_{sat} is the saturated value of the isotropic hardening stress R at infinite large plastic strain [18].

Yoshida et al. [26], notice that the average Young's moduli E_{av} decreases rapidly with increasing pre-strain ε_0^p and approach their asymptotic values. The Young's modulus degradation dependency of the pre-strain can be expressed by the following equation [26]:

$$E_{av} = E_0 - (E_0 - E_a)\left[1 - e^{\zeta \varepsilon_0^p}\right] \tag{2.19}$$

Where E_0 and E_a is the initial Young-s modulus (for virgin material) and for infinitely large pre-strained materials, respectively. As can be seen in Figure 2.23, this equation can describe accurately the degradation of the Young's modulus. Using a cyclic load-unload test and a curve

fitting to the experimental Young-s modulus values, one can obtain this equation-s parameters [12].

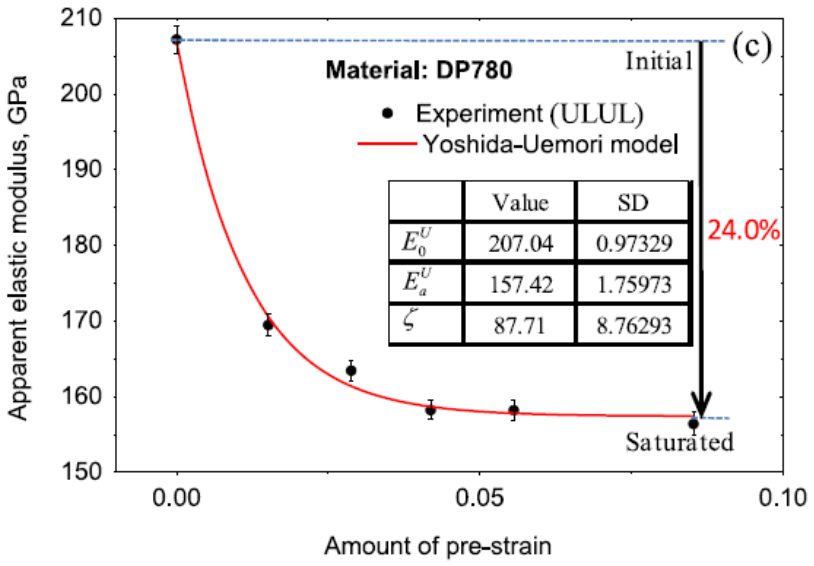

Figure 2.23 - Elastic Modulus decrease in a Uniaxial Load-Unload cyclic test [12]

F. Yoshida and T. Uemori (2002), with the aim of validating the application of their own model to springback prediction, conducted a study with four different constitutive material models to predict the side-wall curl, after a U-shaped bend test for an HSS. The constitutive material models were IH (Isotropic Hardening), LK (Linear Kinematic Hardening), IH+NLK (combined Isotropic Hardening with nonlinear Kinematic Hardening) and the Yoshida-Uemori model. As illustrated by Figure 2.24, the authors concluded that the Yoshida-Uemori model predicts accurately the springback for different die radius, the IH+NLK gives moderate results while IH and LK do not show consistent results [27].

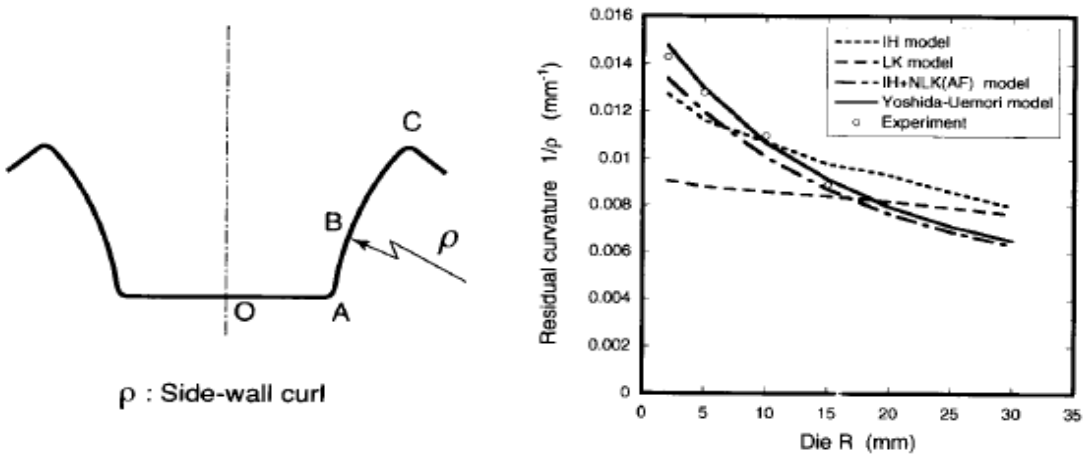

Figure 2.24 - Side-wall curl after springback [27]

3. Methodology

3.1 Material Characterization

The current AHSS steels under study are DP1000 and DP1200 steels. To better understand these steels behaviour, the UNIDEMI research team conducted a series of material characterization tests. The data obtained by those tests will support the present dissertation in material parameters identification and material model validation.

3.1.1 Chemical Composition

With the aim of evaluating and verifying if the material's chemical composition agrees with the steels manufacture data, a chemical analysis test was conducted with an optical emission spectrometer. The tests were carried out in a company called GENERAL ELECTRIC (GE Power) and the results for DP1000 and DP1200 are presented in Table 3.1 and Table 3.2, respectively.

Table 3.1 - DP1000 Chemical Composition

C [%]	Si [%]	Mn [%]	P [%]	S [%]	Al [%]	Nb+Ti [%]	Cr+Mo [%]	B [%]	Cu [%]
0.134	0.197	1.449	0.012	0.0021	0.040	0.0149	0.035	<0.0005	0.0073

Table 3.2 - DP1200 Chemical Composition

C [%]	Si [%]	Mn [%]	P [%]	S [%]	Al [%]	Nb+Ti [%]	Cr+Mo [%]	B [%]	Cu [%]
0.079	0.206	1.505	0.0096	0.0027	0.043	0.038	0.0297	0.0014	0.0059

3.1.2 Uniaxial Tensile Tests

The starting point of experimental work is tensile testing, in this case, the uniaxial tensile test. Being one of the most common and universal tests, the uniaxial tensile test allows to observe certain phenomena and quantify certain mechanical properties, like yield and ultimate tensile strength, Young's modulus and elongation. The machines on which the tests were performed, were a SHIMADZU in MCG's facilities and an MTS in FCT-UNL laboratories. Figure 3.1 illustrates the true stress-strain curves for DP1000 and DP1200 steels obtained by the UNIDEMI's research team.

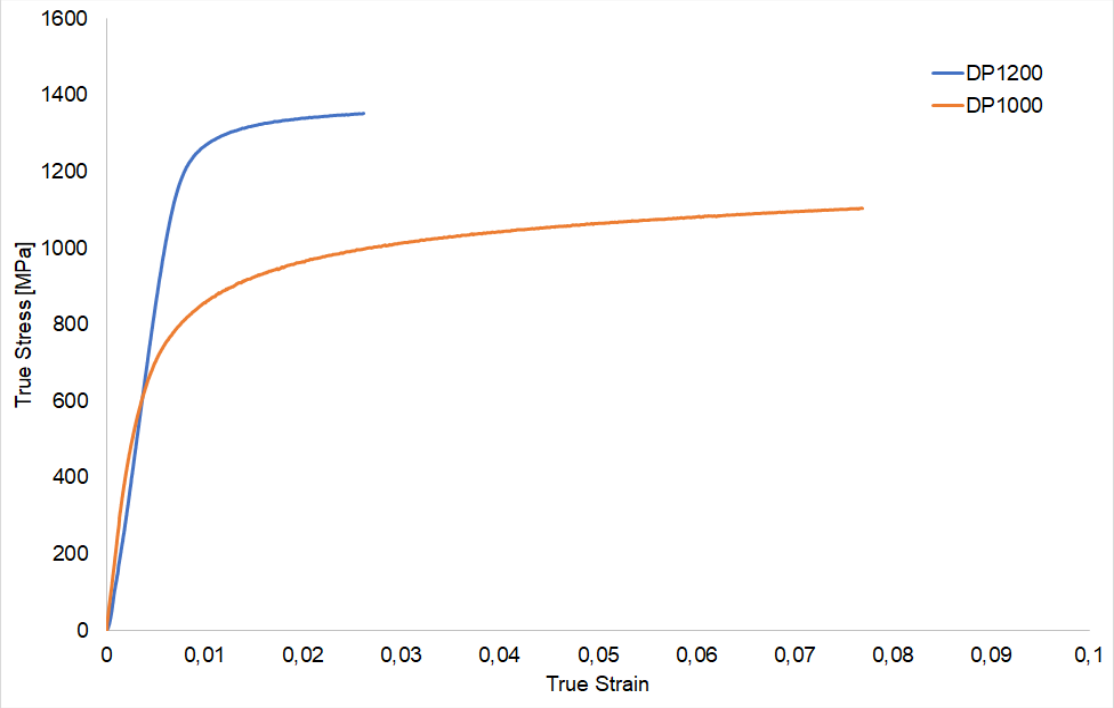

Figure 3.1 - True stress-strain curve for DP 1000 and DP1200

From this test the yield and ultimate tensile strength can be obtained. For DP1000 the values are 757.8 MPa and 1100 MPa, respectively. As for DP1200 the values are, 1126.5 MPa and 1350 MPa, respectively.

To characterize the anisotropic behavior of both materials, the Lankford coefficients were obtained with tensile testing with specimen withdrawn in 0º, 45º, and 90º from the rolling direction. The data obtained by these tests are shown in Table 3.3. The results indicate that both steels possess anisotropic behavior through the thickness, which is good for stamping applications, as referred to earlier.

Table 3.3 - Anisotropy coefficients for DP1000 and DP1200

Material	Lankford Coefficients	Normal anisotropy coefficient	Planar anisotropy coefficient
DP1000	$r_0 = 0.737$	$\bar{r} = 1.021$	$\Delta r = -0.133$
	$r_{45} = 1.087$		
	$r_{90} = 1.172$		
DP1200	$r_0 = 1.019$	$\bar{r} = 1.337$	$\Delta r = -0.336$
	$r_{45} = 1.506$		
	$r_{90} = 1.319$		

3.1.3 Cyclic Loading-Unloading Tensile Tests

To observe and evaluate the Young's modulus degradation, uniaxial loading-unloading tensile test were carried out. The Young's modulus can be obtained after every cycle through the engineering stress-strain curve (Figure 3.2).

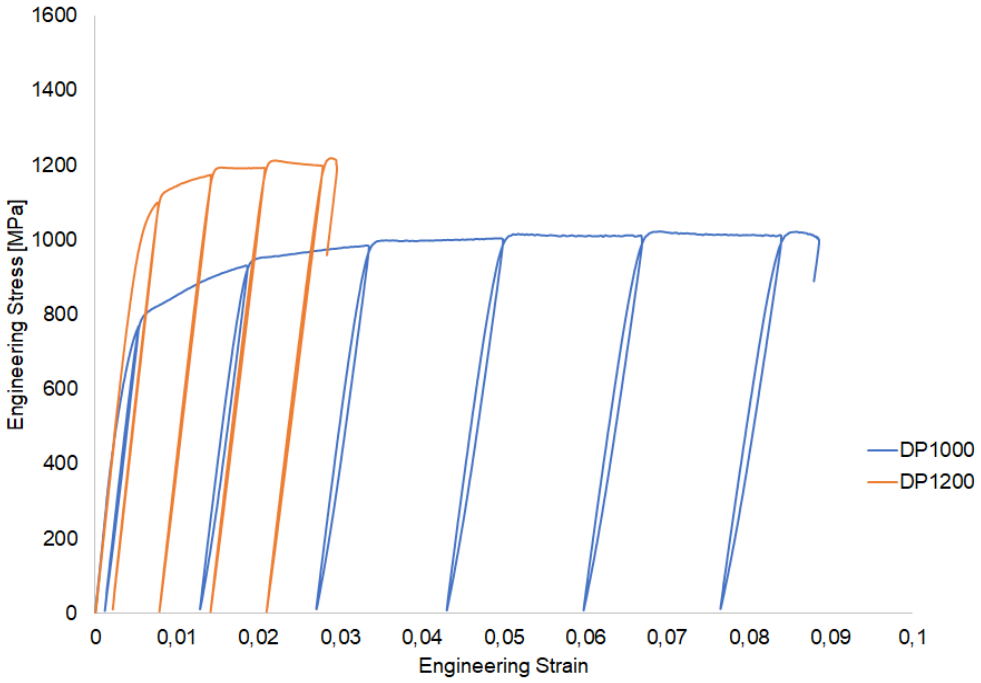

Figure 3.2 - Engineering stress-strain curve for cyclic loading-unloading test

The methodology that was used by the research team to obtain the degradation values is the one used by Sun and Wagoner [28]. The results of these tests are part of another master's dissertation that has not been finalized yet and could not be shown, however the parameters for the Yoshida-Uemori equation for Young's modulus degradation were made available.

3.2 Measurement Procedure

3.2.1 Nakajima and Notch Tensile Tests

The set of tests that involves the Nakajima and the Notch tensile tests, were planned with two main purposes. The conception of an FLD for both materials, and validation of constitutive models for different loading paths. In the present study, the tests are measured with the aim of validation.

Since only one type of specimen geometry, for the Nakajima test, available can exhibit a loading path between the uniaxial deformation, and plane deformation state, the Notch tensile tests complemented the study allowing more loading paths within that range. The specimens of both tests were marked with circumferences of 5 mm in diameter, as shown in Figure 3.3 (a). This methodology is based on the work of C. Schwindt et al. [16].

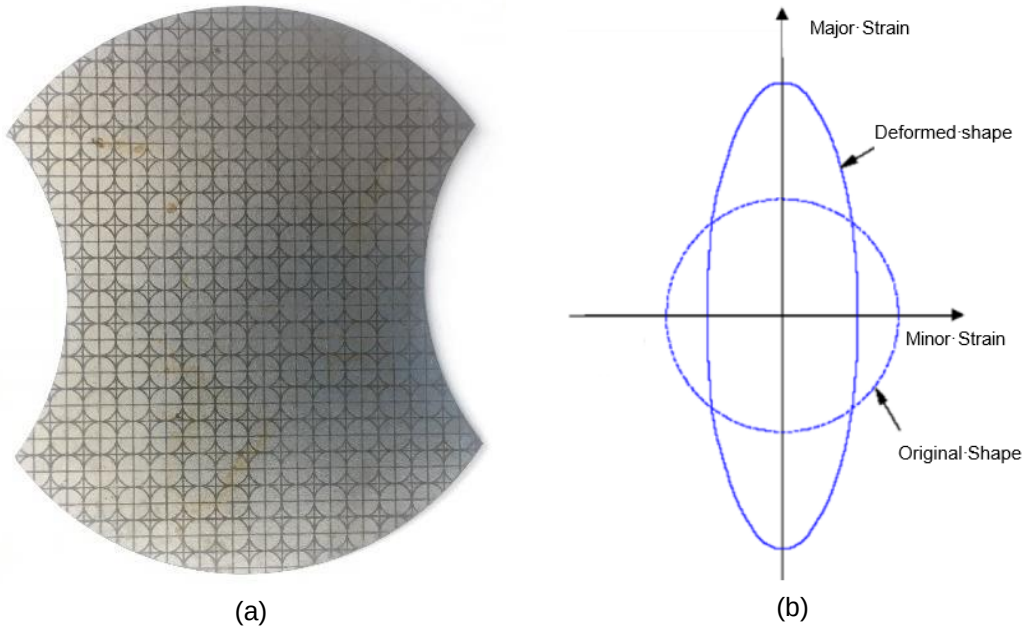

Figure 3.3 - Nakajima specimen: (a) Sheet marking (b) Schematic of the measurement procedure

As illustrated in Figure 3.3 (b), this procedure allows the measurements of the Major and Minor strains after the test is completed. The measurements were carried out with Adobe Photoshop CC[1] software through pictures, taken vertically from the center of the deformed circumference. The camera's position is very important to minimize the parallax errors. For this, it was necessary a calibration procedure using references with known dimensions. After the measurement the strains are obtained with equation (3.1):

$$\varepsilon = \frac{l - d}{d} \tag{3.1}$$

where l is the ellipse axis length (major or minor) and d the initial circumference diameter.

The Nakajima test does not produce linear loading paths, like tensile tests (this might be due to the friction between the specimen and the punch) so, the circumferences to measure are the ones closest to the necking area, to capture the final trajectory [10].

A schematic of the different specimen dimensions is illustrated in Figure 3.4.

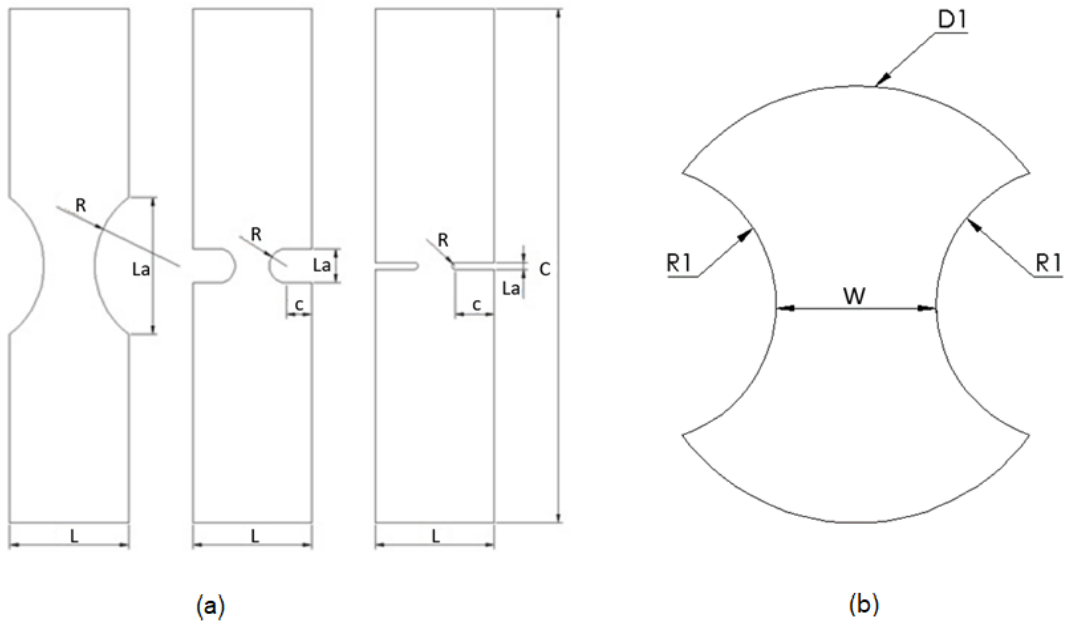

Figure 3.4 - Specimen dimensions: a) Notched tensile test specimen b) Nakajima test specimen

[1] Granted by professor Jorge Pamies Teixeira

The dimensions of the Notched tensile test specimens and Nakajima tests are presented in Table 3.4 and Table 3.5, respectively.

Table 3.4 - Specimen dimensions of the Notched tensile tests

Specimen	1	2	3
La [mm]	40	10	2
R [mm]	25	5	1
c [mm]		7.5	11.5
L [mm]	35		
C [mm]	150		

Table 3.5 - Specimen dimensions of the Nakajima tests

Specimen	1	2	3	4	5	6
W [mm]	20	40	55	60	70	80
D1 [mm]	87					
R1 [mm]	40					

While for DP1000 all Nakajima and notch tensile tests were performed, only the Nakajima tests for 1.0 mm sheet thickness were performed for DP1200, due to time limitations. The number of specimens tested in the notch tensile tests and Nakajima tests are presented in Table 3.6 Table 3.7, respectively.

Table 3.6 - Number of tested specimens with the notch tensile test

		Specimen		
Steel	Thickness [mm]	R25	R5	R1
DP1000	1.0	3	3	3
	1.2	3	3	3

The specimen type designation R25, R5 and R1 is equivalent to the respective notch radius, for instance R25 is the specimen whose notch radius, R, is 25 mm. The same logic follows for the Nakajima test, for instance the specimen W20 is referred to the specimen that has a width, W, of 20 mm (Table 3.5).

The geometries of the specimens and the methodologies for the Nakajima and Notch tensile tests were based on the work of Claudio D. Schwindt et al. [16].

Table 3.7 - Number of tested specimens with Nakajima test

		Specimen type					
Material	Thickness [mm]	W20	W40	W55	W60	W70	W80
DP1000	1.0	3	1	3	2	2	2
	1.2	3	3	3	3	2	3
DP1200	1.0	0	2	2	2	2	2

3.2.2 U-shaped Bend test

As previously mentioned in the Literature Review chapter, the U-shaped bed tests are commonly used to study the springback phenomenon. In this work, U-shaped bend tests were performed in MCG with the aim of quantifying the springback and validate constitutive modes regarding springback prediction. The developed methodology for the specimen measurements, presented in Figure 3.5, is based on the work of J. Jung et al. [14], Yoshida and Uemori [27], and J. Liao et al. [29]. Yoshida and Uemori only quantified the sidewall curl but that does not consider the deviation angle.

Using a scanner, the specimen's section is registered in the computer as an image file (PNG) and is subsequently measured in SolidWorks software. The scale is defined by measuring the distance between the two ends of the specimen flanges, since it is the largest distance that can be used as a reference, to reduce the error propagation of the measurements.

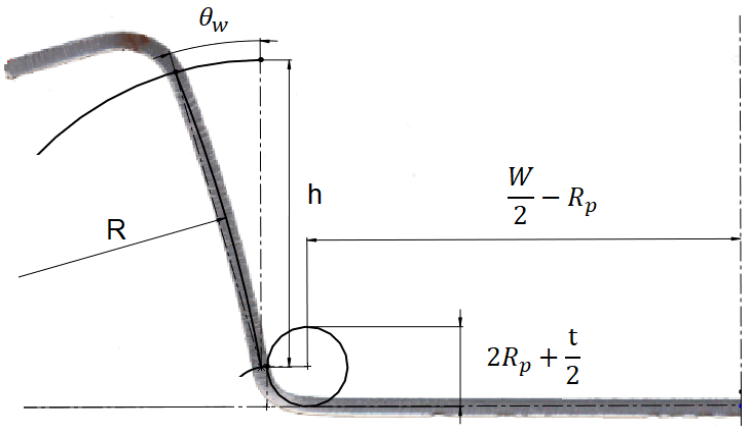

Figure 3.5 - Measurement methodology for springback quantification of a U-shaped bend test specimen

In Figure 3.5 and Figure 3.6, W represents the punch width, R_p the punch radius, t the specimen thickness, h the stamping depth, R the side wall curl radius and θ_w the opening angle. The reason for the measurements being performed in a mid-surface of the specimen thickness is due to the simulation being composed by mid-surface shell elements and to have a more accurate comparison.

To observe the influence of different tool parameters like the punch radius, U-shaped bend test with different tools were performed. This also allows to see which constitutive material models can adapt to different test parameters. The different U-shaped bend tests are illustrated in Figure 3.6 and the respective table (Table 3.8).

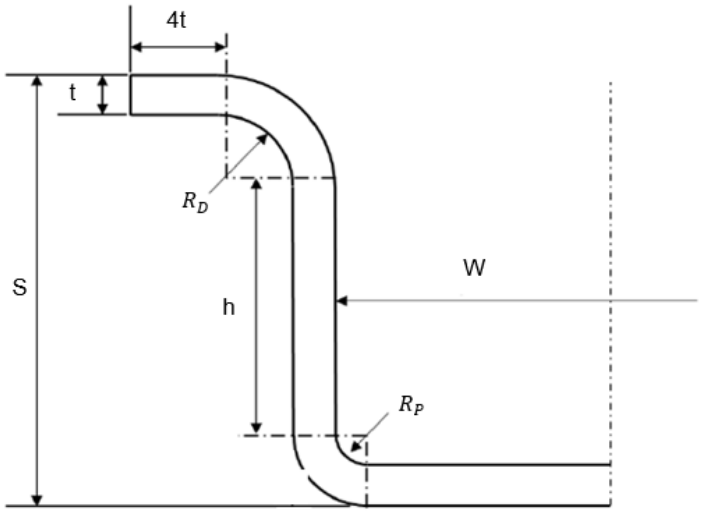

Figure 3.6 - Blank section after the test and before springback

Table 3.8 - Specimen dimensions: U-shaped bend test

t [mm]	1.0				1.2			
W [mm]	30		60		30		60	
R_P [mm]	2	10	2	10	2	10	2	10
R_D [mm]	3	15	3	15	3	15	3	15
S [mm]	26	46	26	46	26.2	46.2	26.2	46.2
h [mm]	20							
L_S [mm]	91.3	138.1	121.3	168.1	93.2	140.0	123.2	168.3
W_S [mm]	100							

where L_s and W_s is the specimen length and width, respectively.

Like in the Nakajima test, all these U-shaped bend test variations were performed for the DP1000 steel, while DP1200 had some limitations, as referred to earlier.

3.3 Simulation Procedure

After being plastically deformed, AHSS steels exhibit springback phenomenon. The use of simulation with accurate constitutive models can significantly reduce the production cost of AHSS parts by reducing tool adjustments and material waste. The current study aims at validation of constitutive models for DP1000 and DP1200 steels. With that purpose, two different types of validations are performed. One for load path characterization with the simulation of Nakajima and Notch tensile tests, and the other for springback prediction with the simulation of the u-shaped bend test.

3.3.1 LS-DYNA Material Models

Initially, the software chosen for the conduction of this study was ANSYS. ANSYS is a very powerful simulation software that allows not only structural analysis but also fluids, electronics, systems and many other engineering fields of study. The change for LS-DYNA version 10.0, was mainly due to the range of constitutive material models included in the software. LS-DYNA is very popular in car crash simulations, using explicit time integration. However, in this study, it was used for metal forming simulations. The material models presented in this section are referenced to LS-DYNA manual version 10.0 [30].

3.3.1.1 Elastic Plastic with Kinematic Hardening

This is a material model provided by the LS-DYNA software, version 10.0, known as Material Plastic-Kinematic or MT (Material Type) 3. This model enables the user to choose an isotropic, kinematic or a mixed isotropic-kinematic hardening formulation of the yield surface. This is possible due to one input parameter in this model (β'). The stress calculation follows the equation (3.2):

$$\sigma_y = \sigma_0 + \beta' E_p \varepsilon_{eff}^p \tag{3.2}$$

The kinematic motion of the yield surface follows:

$$\alpha_{ij}^{\nabla} = (1 - \beta')\frac{2}{3}E_p\dot{\varepsilon}_{ij}^{p} \tag{3.3}$$

$$E_p = \frac{(E_t E)}{E - E_t} \tag{3.4}$$

Where σ_y and σ_0 are the instantaneous and initial radius of the yield surface, E_p [MPa] the plastic hardening modulus and E_t [MPa] the tangent modulus. The tangent modulus is the slope of the stress--strain curve at any specified stress of strain. In this material model, E_t represents the slope of the plastic component of the true stress-strain curve, when represented by a line.

If $\beta' = 0$, a pure kinematic formulation is obtained, since equation (3.2) is reduced to $\sigma_y = \sigma_0$ and the yield surface will not expand, although the yield surface will translate following equation (3.3). The pure isotropic formulation is achieved when is given the value $\beta' = 1$, where the yield surface will expand, as expressed in equation (3.2), and will not translate due to its effect on equation (3.3), $\alpha_{ij}^{\nabla} = 0$.

Figure 3.7 illustrates that the material is modeled with a bilinear behaviour, and the influence of isotropic or kinematic hardening formulation.

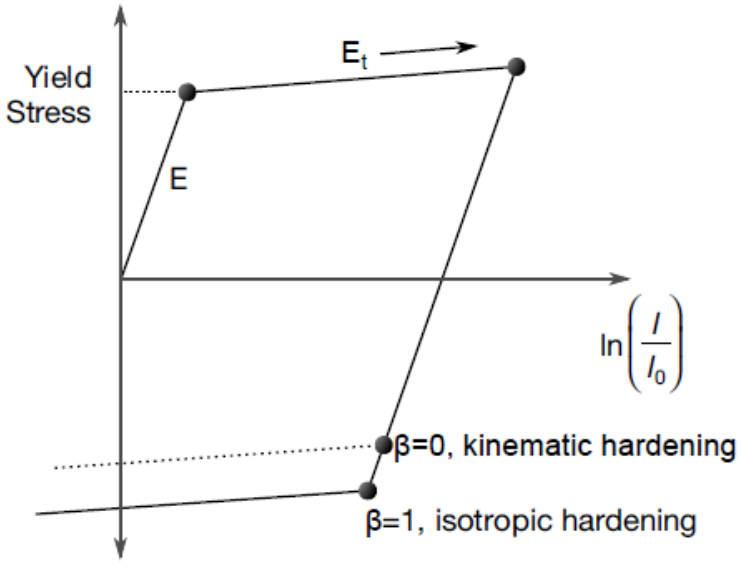

Figure 3.7 - Elastic Plastic behaviour described by MT 3 [30]

The input material parameters are mass density, Young's modulus, Poisson's ration, yield stress, the tangent modulus and the hardening parameter β'.

3.3.1.2 Power Law Isotropic Plasticity

This material model is identified as MT 18, it is an isotropic plasticity model which uses a power law hardening rule. The yield stress is given as a function of plastic strain given by equation (3.5), based on Ludwik-Hollomon hardening rule.

$$\sigma_y = K\varepsilon^n = K\left(\varepsilon_{yp} + \bar{\varepsilon}^p\right)^n \tag{3.5}$$

The elastic strain at yielding (ε_{yp}), is calculated based on the yield tensile strength input value:

$$\varepsilon_{yp} = \left(\frac{\sigma_y}{k}\right)^{\frac{1}{n}} \tag{3.6}$$

The input parameters for this model are mass density, Young's Modulus, Poisson's ration, yield stress, the strength and hardening exponent coefficients from Ludwik-Hollomon hardening rule.

3.3.1.3 Barlat's 3-Parameter Plasticity Model

Known as MT 36, this LS-DYNA material model is based in Barlat and Lian's 1989 yield criterion. The purpose of this model if for sheet metal forming simulations with anisotropic behavior, under plane stress conditions. The anisotropy is modeled with the Lankford coefficients in 0º, 45º, and 90º from the rolling direction. As mentioned in the Literature Review chapter, the yield surface is calculated based on these three coefficients.

The hardening rule can be a linear, exponential or determined by a load curve. The load curve input is the true stress as a function of plastic strain in uniaxial tension in the rolling direction (0 degrees). The current material model possesses multiple options to characterize the material behavior. Many methods are available for the hardening rule, anisotropy characterization and even an option to include Young's modulus as a function of plastic strain.

The chosen method was to characterize the material with a load curve for the hardening rule, the Lankford coefficients, the exponent (M) in Barlat yield function and Young's modulus is given as constant. Other material parameters are also needed, like mass density and Poisson's ratio.

3.3.1.4 Transversely Anisotropic Elastic-Plastic

This material model (MT 37) is for simulating sheet forming processes with anisotropic material, although only transverse anisotropy can be considered. The yield function is modeled by the Quadratic Hill Yield Criterion. If the normal anisotropy coefficient is not given, the material model reduces to a von-Mises material. The hardening rule can be defined with a load curve, like MT 36. The Young's modulus degradation can be included with the Yoshida-Uemori equation (2.19).

The input parameter for this model are mass density, initial Young's modulus, Poisson's ratio, load curve in uniaxial tension, normal anisotropy coefficient and the parameters for the Yoshida-Uemori equation for Young's modulus degradation. The load curve in this model is expressed by effective stress as a function of effective plastic strain in uniaxial tension.

3.3.1.5 Anisotropic Plastic

This is material type 103_P, a simplification of material type 103 (Anisotropic Viscoplastic) [30]. The yield surface expands with isotropic hardening. Material anisotropy is defined with Lankford coefficients and the hardening rule is given by a load curve that defines effective stress vs effective plastic strain in uniaxial tension. The main difference between MT103p and MT36 is that the present model uses the following yield criteria:

$$F(\sigma_{22}-\sigma_{33})^2 + G(\sigma_{33}-\sigma_{11})^2 + H(\sigma_{11}-\sigma_{22})^2 + 2L\sigma_{23}^2 + 2M\sigma_{23}^2 + 2N\sigma_{12}^2 = \left[\sigma\left(\varepsilon_{eff}^p, \dot{\varepsilon}_{eff}^p\right)\right]^2 \quad (3.7)$$

3.3.1.6 Kinematic Hardening Transversely Anisotropic

Known as MT125, this model combines the Yoshida-Uemori constitutive model with material type 37. As demonstrated in the Literature Review, this model uses two surfaces (one yield surface modeled with kinematic hardening and a bounding surface modeled with a combination of isotropic-kinematic hardening) with a transversely anisotropic material (Hill criterion).

The input material parameters are the seven Yoshida-Uemori material parameters, the normal anisotropy coefficient, the parameters for the Yoshida-Uemori equation for de Young's modulus degradation, mass density, yield stress and Poisson's ratio.

Although the Yoshida-Uemori model has seven material parameters, they are relatively easy to obtain. A simplified way of obtaining the material parameters is through curve fitting. Using the equations that define each part of the tension-compression test, one can adapt these equations to the experimental data. With equation (3.8), the parameters B, $(R_{sat}+b)$, and m can be obtained with curve fitting as shown in Figure 3.8. This equation describes the behaviour of the bounding surface in the forward stress [31].

$$\sigma_{Bound} = B + (R_{sat}+b)\left(1 - e^{-m\varepsilon^p}\right) \tag{3.8}$$

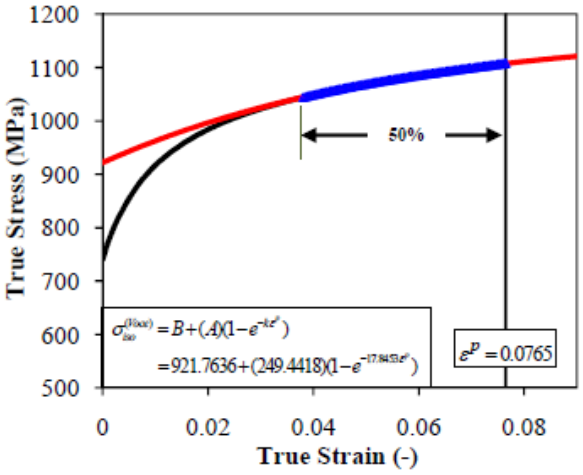

Figure 3.8 - Fitting of bound stress curve [31]

Using the reverse stress curve from the experimental test (Figure) and equation (3.9), the parameters b and R_{sat} can be obtained, since m and $(R_{sat}+b)$ are already known [31].

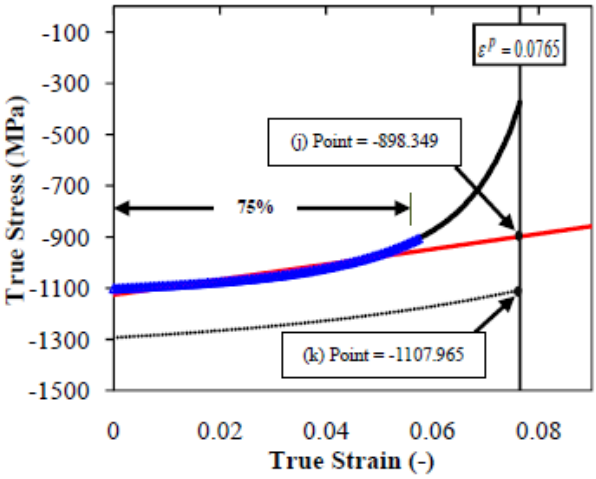

Figure 3.9 - Fitting of reverse bound stress curve [31]

$$\sigma_{Bo}^{(P)} = 2b\left(1 - e^{-m\varepsilon^p}\right) \tag{3.9}$$

The (k) point present in Figure 3.9 represents the isotropic boundary calculated from 0.0765 plastic strain [31].

T. Phongsai et al. [31], stated that the parameter h does not influence significantly the simulations so fixed its value, leaving only the parameter C to be obtained. That can be done with another curve fitting, with equation (3.10).

$$\sigma_B^t \cong 2ae^{-C\varepsilon^p} \tag{3.10}$$

Where σ_B^t [MPa] represents the difference between the reverse stress strain curve from the transient Bauschinger zone, as illustrated in Figure 3.10 a). The curve fitting can be seen in Figure 3.10 b).

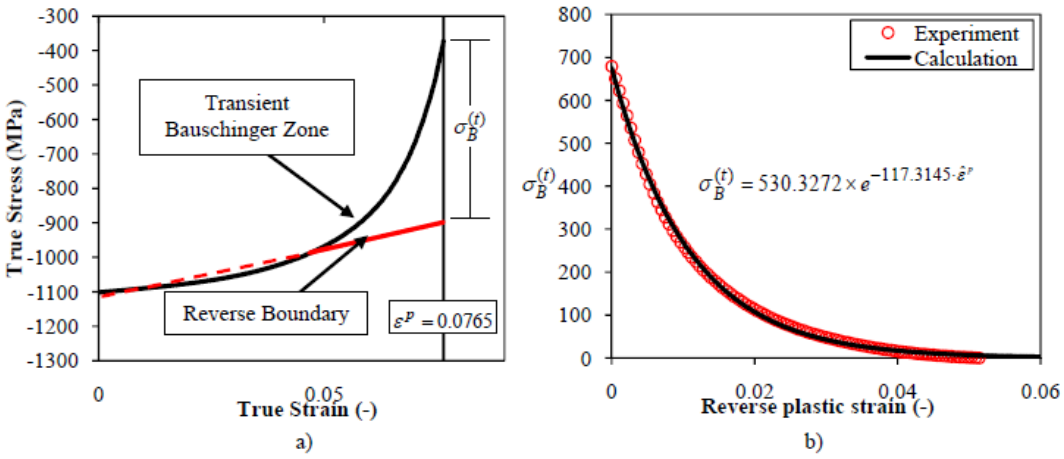

Figure 3.10 - Determination of parameter C [31]

3.3.2 Nakajima Simulation

LS-DYNA is a finite element program for transient dynamic analysis using the explicit time integration method. This means that the simulations have short time durations and are performed in a dynamic environment were dynamic effects are present. The Nakajima test does not fit in this description, the test has a large time duration and the punch velocity is low, meaning that the dynamic effects can be neglected. Thus, the Nakajima test should be simulated using implicit time integration, since is a quasi-static problem.

Instead of performing an explicit time integration simulation with a long-time duration, an artificially high punch velocity can be applied to reduce the time duration of the test, although to reduce the dynamic effects introduced by the tool velocity, one can use the mass scaling technique. Mass scaling is used to achieve higher timesteps in explicit simulations by adding nonphysical mass to the elements of the deformable part (the specimen). B. Maker and X. Zhu [32] recommended that the tool velocity should not surpass 2.0 mm/ms. The simulation's methodology is based on the work of the present authors.

To make sure that it is performed a quasi-static simulation, the kinetic energy should be much lower than the internal energy, which is controlled by the timestep size. A comparison between the internal energy and the external work should also be done. If the internal energy and the external work are very similar, the simulation did not present any calculation instabilities, like contact penetrations. Internal energy considers the elastic strain energy and the work done in permanent deformation, while the external work is the work done by applied forces and the punch displacement.

There are four parts that must be modeled to perform the Nakajima test simulation, the three tools (punch, die, and blank holder) and the specimen. The specimen is clamped between the die and the blank holder by a 70 mm diameter ring. To reduce simulation time, instead of modeling the whole setup the simulation is reduced within that diameter. This means that D1 (Figure 3.4) will be reduced to 70 mm while maintaining the other dimensions in agreement with Table 3.5. So, the specimen nodes that coincide with that circumference are constrained from any displacement with boundary conditions. The modeled test setup is illustrated in Figure 3.11.

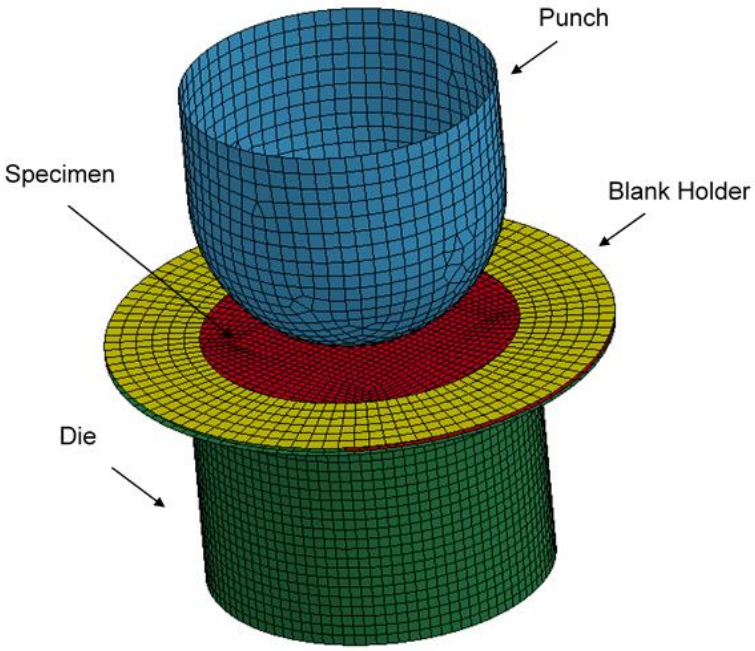

Figure 3.11 - Nakajima Test Simulation model

To reduce the simulation runtime and avoid hourglass problems the fully integrated thick shell elements are used. These elements consider the thickness variations with integration points through the thickness (this option is used only for the deformable body). For specimen with 1.0 mm and 1.2 mm thickness, 7 and 9 integration points are used, respectively. The tools are defined as rigid bodies, so no deformation occurs, and no time is wasted on such calculations. Thus, the specimen is the only deformable body in the simulation.

The specimen is modeled with square shaped elements ($1 \times 1\ mm^2$) while the rigid bodies are modeled with $2 \times 2\ mm^2$ elements. The meshing of the rigid bodies is not so important except where curvatures exist. In that exception, the part must be carefully meshed to exhibit a good approximation to the actual geometry.

The punch displacement input in the simulation is slightly higher than the actual one. This allows observing if the material can fully follow the loading path since it's not linear. The input simulation and experimental average values can be found in Table 3.9. After reaching the input value the punch slowly reverses the movement direction.

Table 3.9 - Punch displacement in the Nakajima test and Simulation

	DP1000		DP1200	
	Experimental [mm]	Simulation [mm]	Experimental [mm]	Simulation [mm]
W20	12.36	14		
W40	15.87	17	8.22	10
W60	15.09	17	10.79	12
W80	17.43	19	14.02	16

Table 3.9 illustrates the setups simulated for 1.0 mm thickness.

When multiple parts are used in a simulation, one must define the contacts between each pair of parts otherwise, the parts would just go through each other. The chosen contact type is the One-way surface to surface contact [33]. This type of contact allows the compression and tangential loads to be transferred between the slave (deformable body) and the master (rigid bodies).

After the simulation is completed, the software gives the principal strains as an output. Analyzing the two first principal strains one can build the loading path that the material model exhibited through the simulation. The elements chosen for the strain output are, approximately the ones within the same areas as the circumferences measured in the experimental specimen.

A flowchart illustrated in Figure 3.12, shows the methodology followed for every Nakajima simulation. The procedure is repeated for all the material models previously mentioned.

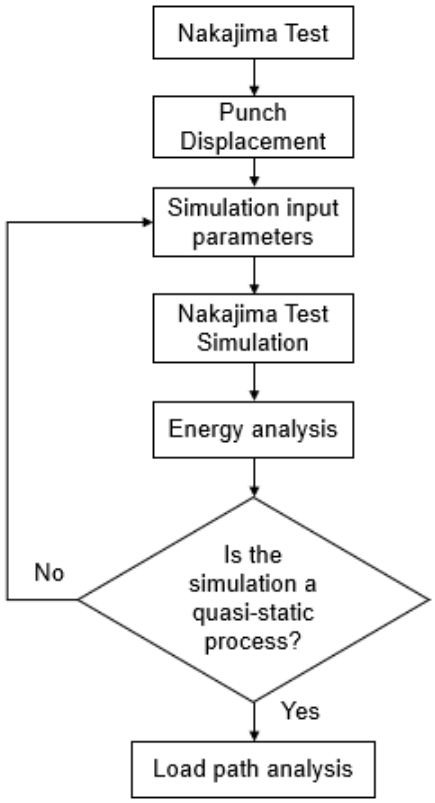

Figure 3.12 - Flowchart of the Nakajima simulation methodology

3.4 Notch Tensile test simulation

Although the notch tensile and Nakajima tests have the purpose of study different loading paths, they are very different tests. The simulation of this test was also performed with explicit time integration, which means that the energy of the simulation must be carefully monitored. Also, the output strain method is the same as in the Nakajima test simulation. So, the main difference is that, for this simulation no rigid bodies (tools) were modeled, only the specimen. The method was to clamp one side of the specimen and apply the respective displacement on the other. The elements are shell elements as well and the mesh was refined around the necking area, as Figure 3.13 illustrates.

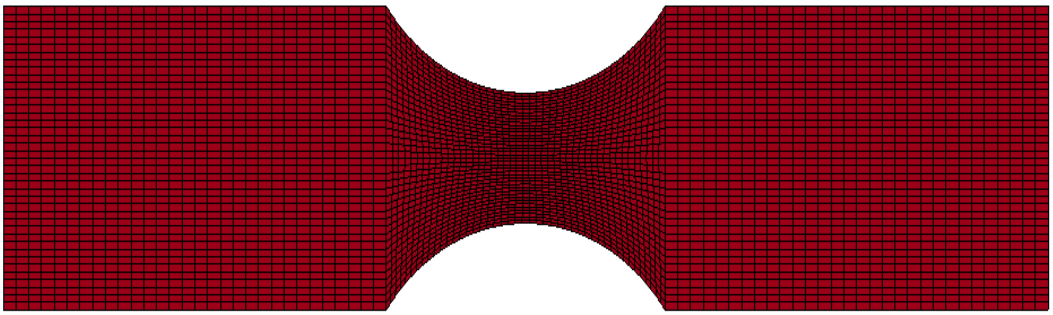

Figure 3.13 - Meshed specimen for notch tensile test simulation

3.5 U-Shaped Bend test Simulation

The U-shaped bend test simulation has the aim of validating constitutive models for springback prediction. To achieve this, the test was divided into two distinct simulations, a forming simulation with explicit time integration and a springback simulation with implicit time integration. This methodology is based on the work of B. Maker and X. Zhu [34].

The forming simulation is very similar to the Nakajima test simulation. Although, in this one, the test setup was cut in half and simulated with symmetry boundary conditions, with the aim of reducing the runtime of the simulation as shown in Figure 3.14. The element and contact types are the same as the Nakajima test simulation. As for the element size, the blank (specimen) was modeled with 0.5 for 0.5 mm squares. This refined mesh was made for improving the accuracy in the springback simulation, due to the small punch and die radius, in some of the test variations. The tools are defined as rigid bodies and the specimen as a deformable one. Also, the same care must be considered regarding the simulation energy to remain a quasi-static process. The input parameters for the simulations (blank holder load, displacement, etc.) are the same ones as for the experimental tests.

After the forming simulation, the software outputs a file containing the element history variables of the specimen. This file will be used as an input for the springback simulation and because it only has the deformable part, the rigid bodies (tools) will be neglected in the next simulation.

At the beginning of the springback simulation, it is performed an inertial relief to the specimen so that the part does not contain artificial support constraints. After that, the nonlinear implicit springback simulation begins. These simulations often tend to have convergence issues, so it was set for the solver to form a new stiffness matrix after every iteration and the LS-DYNA artificial stabilization method was applied. The artificial stabilization divides the springback response into several steps, in this case, 4 steps are applied.

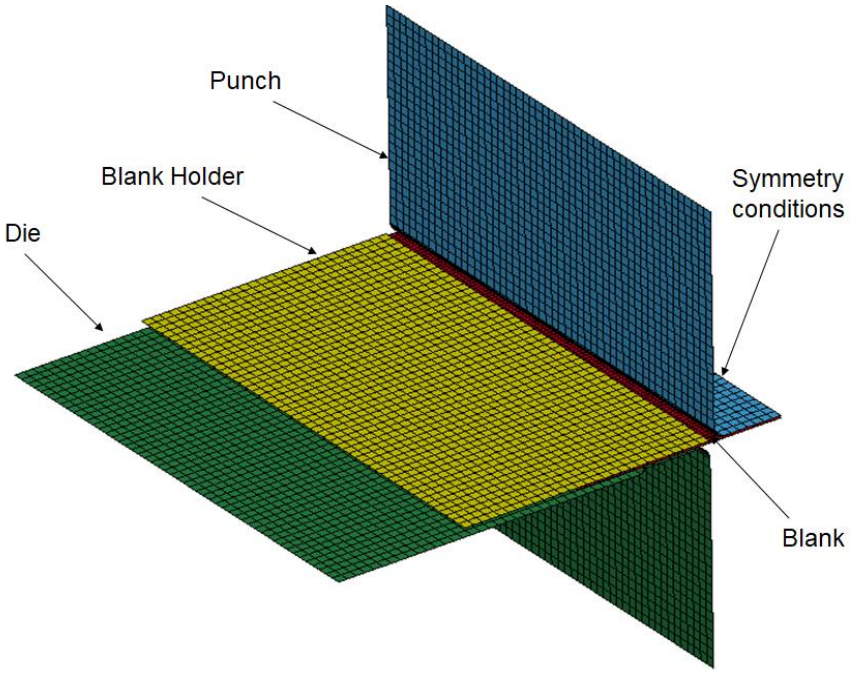

Figure 3.14 - U-shaped bend test simulation setup

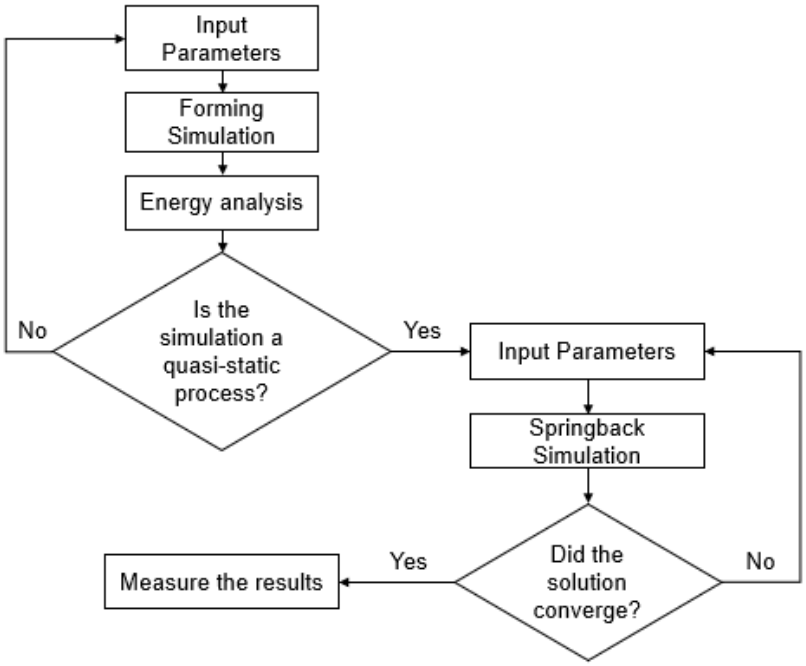

Figure 3.15 - U-bend test simulation methodology

After the simulation, the result is a specimen with a certain amount of springback. This part can be converted to an STL file format and measured in SolidWorks software, with the same methodology as the experimental procedure. This methodology is represented by the flowchart illustrated in Figure 3.15.

4. Results and Discussion

4.1 Experimental Measurements

The material characterization tests were previously performed in earlier stages of the ULTRAFORMING project. Even though, the results of the Nakajima test, Notch tensile test, and U-shaped bend tests were not analysed. So, the measurement of the respective specimen and the results interpretation is also part of the current study.

4.1.1 Nakajima Test

As mentioned in the Methodology section, the Nakajima test allows the study of a certain material under different deformation paths. The results of this test are shown in the principal strain space, where the major and minor strains are referred to the first (ε_1) and second (ε_2) principal strains, respectively.

Since the specimen with the largest width is 80 mm, and it is clamped by a ring with 70 mm diameter, between the die and the blank holder, the loading path exhibited by the largest specimen (W80) is theoretically the same as the elementary biaxial tension ($\varepsilon_1 = \varepsilon_2$). While W20 is the specimen that should be closer to the uniaxial tension deformation path ($\varepsilon_1 = -2\varepsilon_2$).

The number of specimens is far greater for DP1000 steel, and for that reason, the experimental measurements are presented separately to avoid a big cluster of points. While for DP1200 the results will be presented in one single chart, since de different loading paths are clearly distinguished from each other.

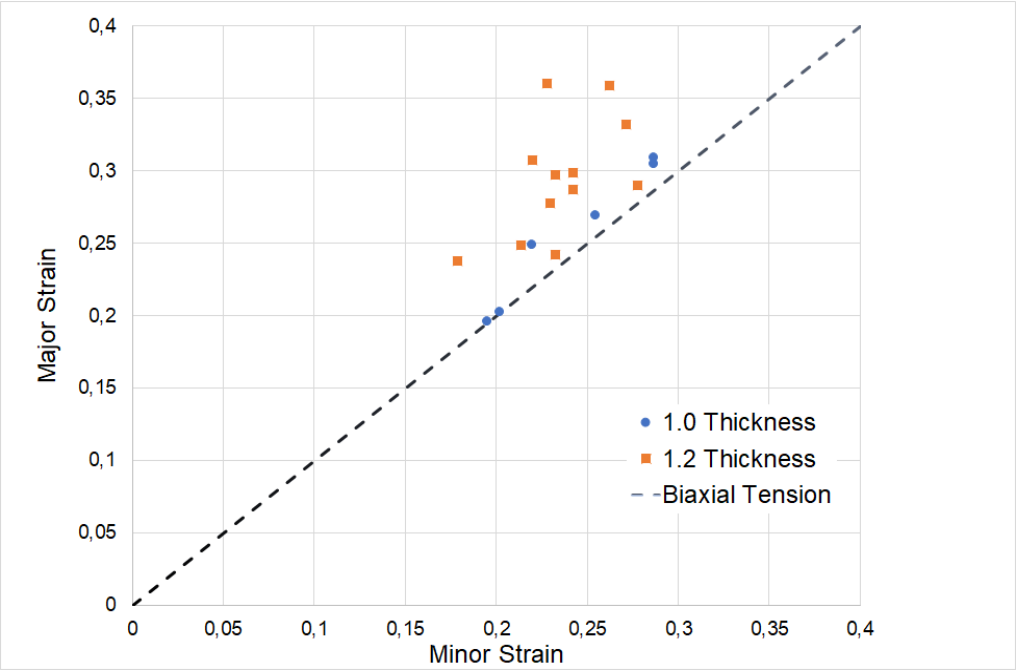

Figure 4.1 - W80 loading path for DP1000

Figure 4.1 illustrates the loading path correspondent to the W80 Nakajima specimens for 1.0 mm and 1.2 mm thickness. The results for 1.0 mm thickness are very close to the elementary biaxial loading path. The results obtained for 1.2 mm thickness agree that the increase of sheet thickness translates the FLC upwards in the Major strain direction.

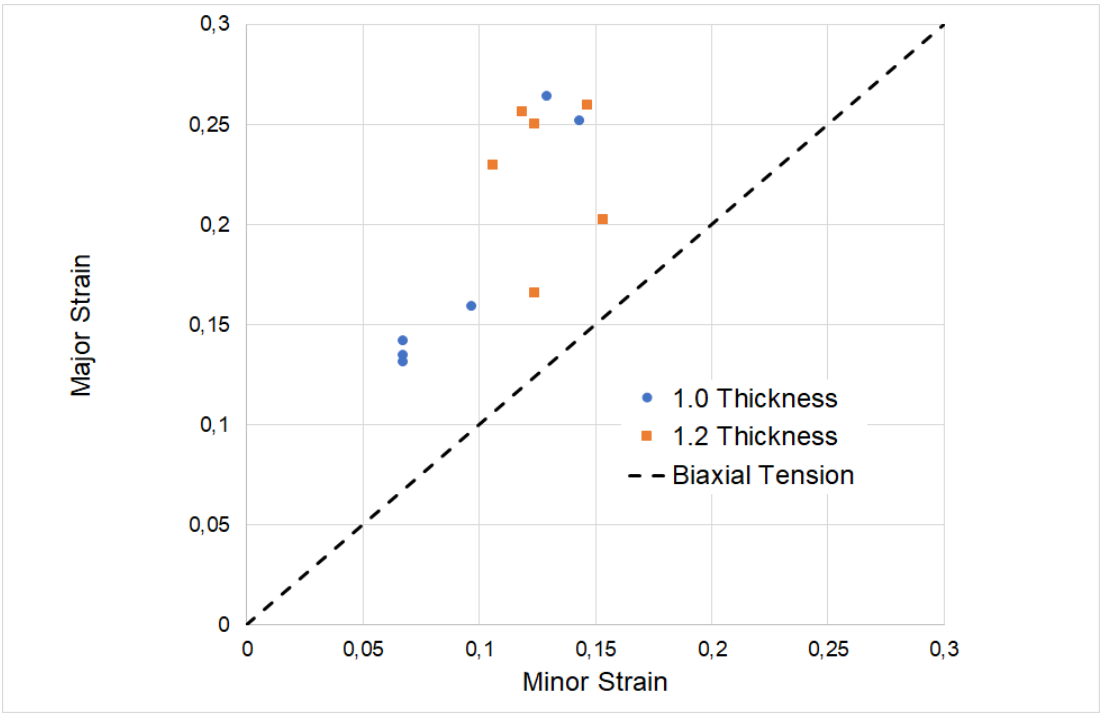

Figure 4.2 - W70 loading path for DP1000

The W70 loading path, illustrated in Figure 4.2, also shows, on average, some consistency when the sheet thickness is increased. The change of width caused a slight shift in the loading path, away from the biaxial tension, when compared to the W80. Two dots of the 1.0 mm test are high compared with the 1.2 mm thickness. A possible explanation might be that, in some specimen, the fracture followed the marks on the sheet, meaning that the marking procedure could have induced stress concentrations. This would give the fracture a preferential direction for its propagation.

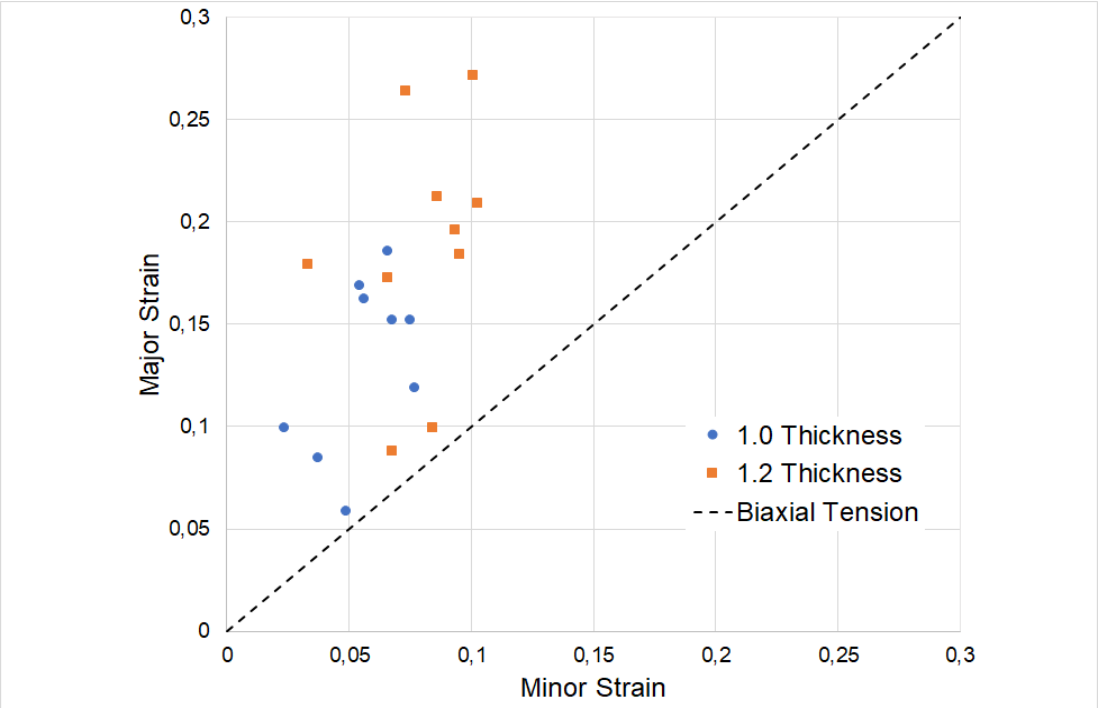

Figure 4.3 - W60 loading path for DP1000

In resemblance to W70, the W60 loading path, illustrated in Figure 4.3, shows that the reduction of the specimen width slightly shifts once more. Even though that the measurements show a higher dispersion of points, the values of Major and Minor strains are decreasing, as they would do in a typical FLD. Once more, the influence of the sheet thickness is noticeable.

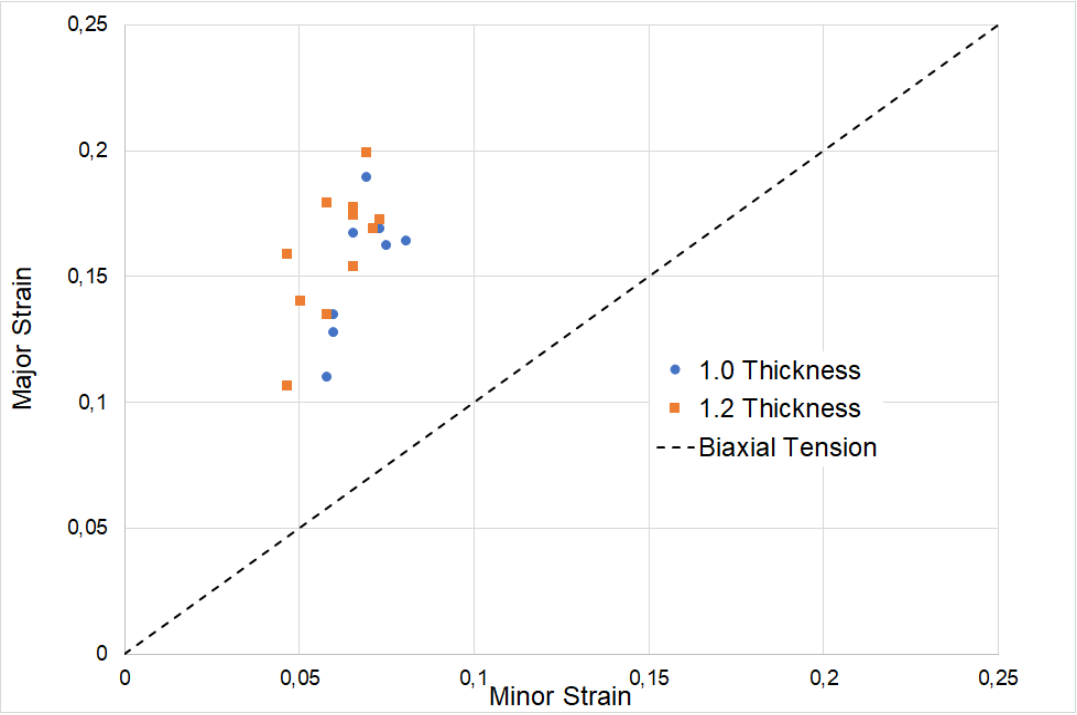

Figure 4.4 - W55 loading path for DP1000

Figure 4.4 represents the loading path from the W55 specimens. In average, the shift of the loading path is not noticeable, when compared to the W60, however, it does show a decrease in the sheet formability. These measurements show a high resemblance with both thicknesses, unlike the previous results.

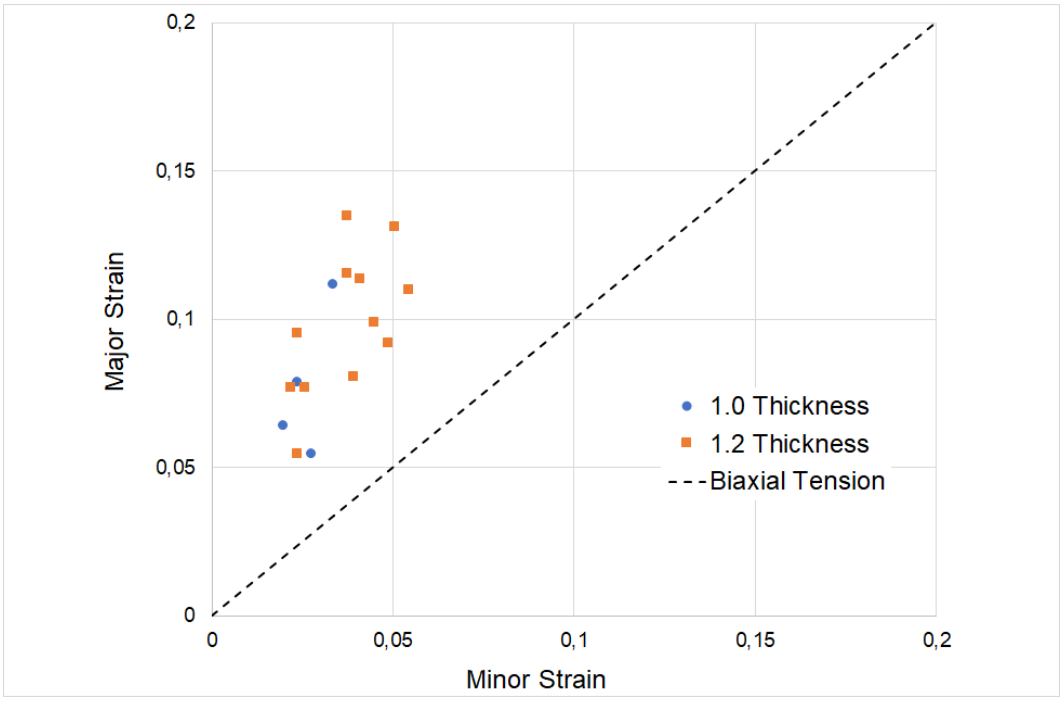

Figure 4.5 - W40 loading path for DP1000

The Nakajima test, when performed with a W40 specimen type, presents a loading path closer to the plane deformation state, as illustrated in Figure 4.5, than the previous ones. Even though that only one specimen with 1.0 mm thickness was successfully tested, it is noticeable that the 1.2 mm results tend to reach higher levels of major strain.

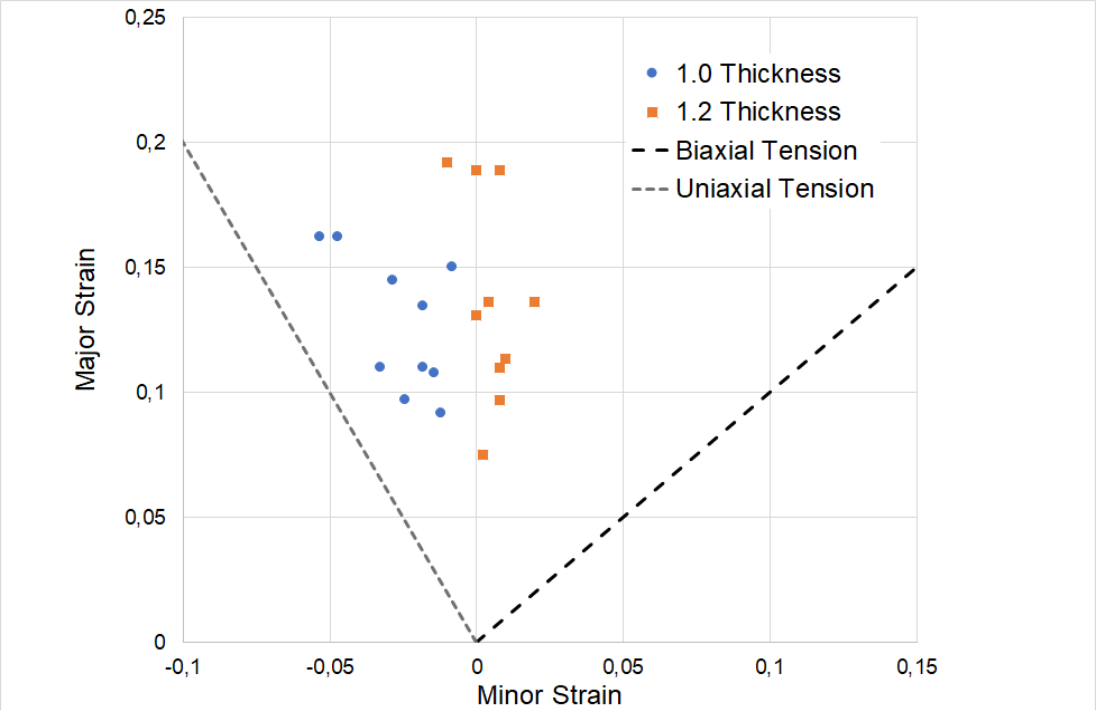

Figure 4.6 - W20 loading path for DP1000

The Nakajima test with the W20 specimen represents the loading path closer to the uniaxial tension. The results for 1.0 mm thickness show a loading path close to the uniaxial deformation, however, the 1.2 mm thickness is placed in the plane deformation. The measurements for these specimens presented some difficulties, due to the specimen being completely fractured, which might have induced some errors. Even so, this happened with both specimen thicknesses.

Most of the DP1000 specimens from the Nakajima test show signs of slight slipping between the die and the blank holder, where the blank should be clamped. This induces some changes in the measured major and minor strains, leading to a minor difference in the loading paths.

The W20 specimens were separated into two pieces, which led to additional difficulties in the measurements. A test setup with punch depth control should be implemented to avoid the complete fracture of the specimen. However, the results for DP1000 were consistent with the expected. The loading paths shifted towards the uniaxial tension with the decreasing specimen's width.

Figure 4.7 gathers all the Nakajima tests for DP1000 and it is clear that not all loading paths are distinguished from the others, specially when it comes to more complex loading paths.

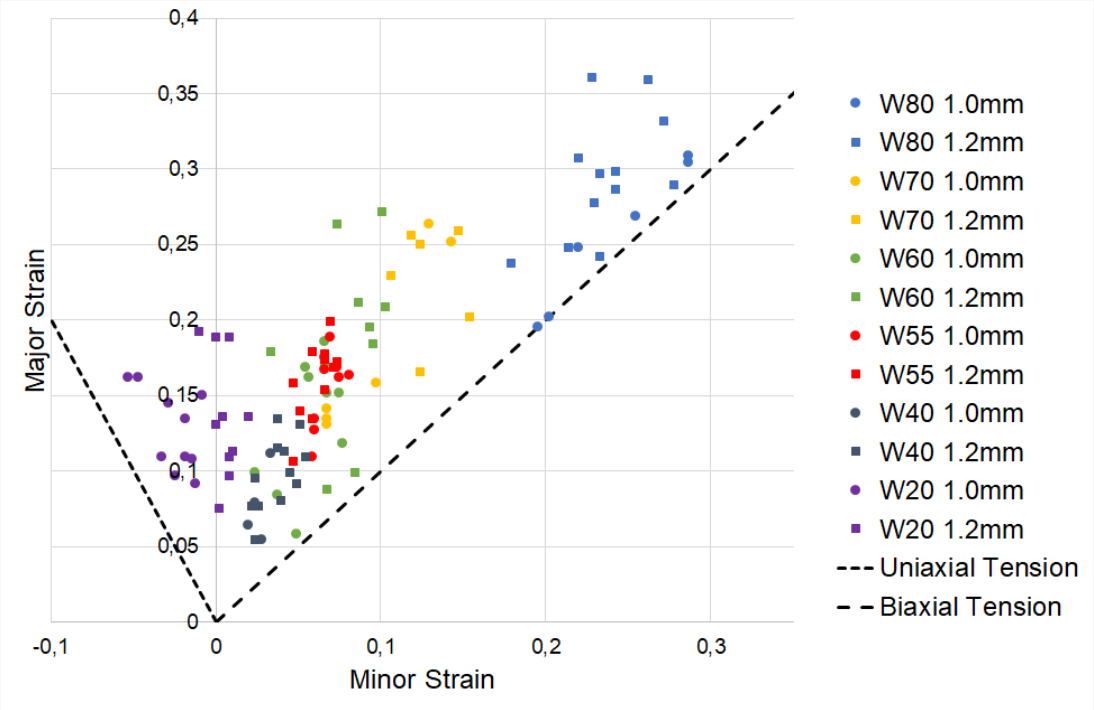

Figure 4.7 - Nakajima results for DP1000 steel

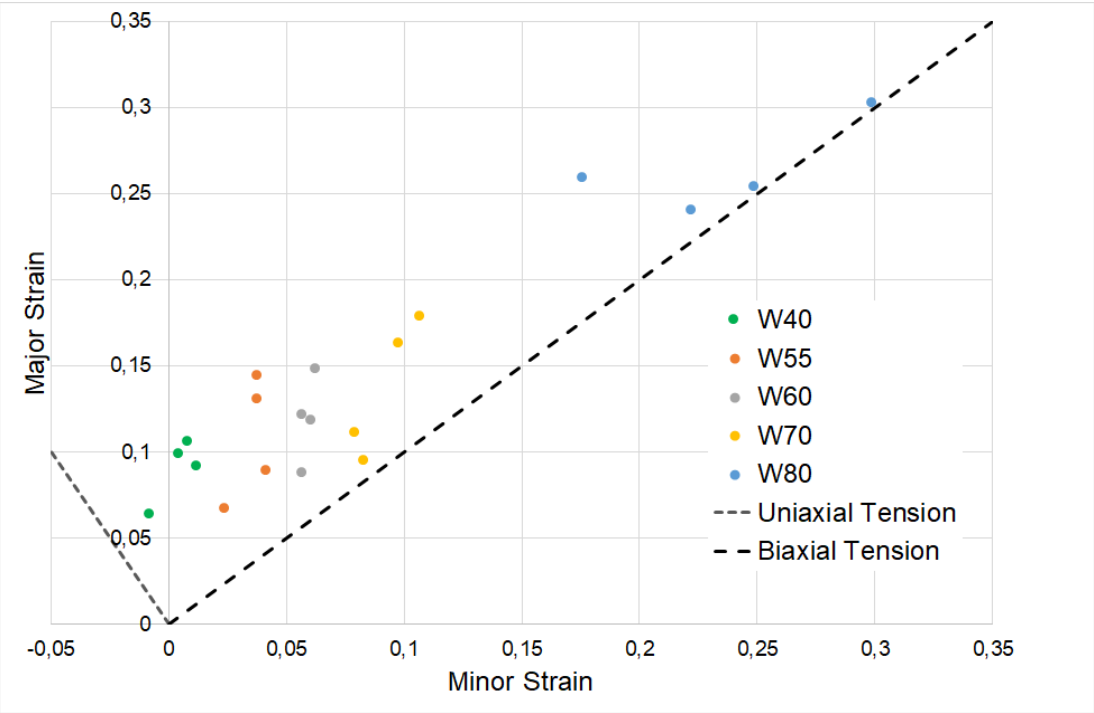

Figure 4.8 - Nakajima test results for DP1200 steel

The results of the Nakajima tests for DP1200 steel, that are illustrated in Figure 4.8, show a clear difference among the loading paths. Except for W80 and W40, this steel presented lower formability. Unlike the DP1000 tests, these specimens do not show signs of slipping. That might be the reason why the loading paths are easily distinguished from each other.

The methodology used for the measurement procedure of these tests doesn't consider the final geometry of the specimen. The hemispherical punch causes the specimen to have curvatures and even though that the photos were taken in a vertical position, the strains can be underestimated. This is more significant for DP1000 in which the punch had a higher displacement. Also, the springback phenomenon exhibited by DP1200 greater than DP1000 steel, meaning that the curvature in DP1000 will always present a steeper curvature.

4.1.2 Notch tensile test

The notch tensile tests allow different loading paths between the uniaxial tension and the plane deformation state. The results are presented in Figure 4.9. The tests are distinguished by AARBB, where AA means the sheet thickness (10 represents 1.0 mm and 12 represents 1.2 mm) while BB represents the notch radius in millimetres.

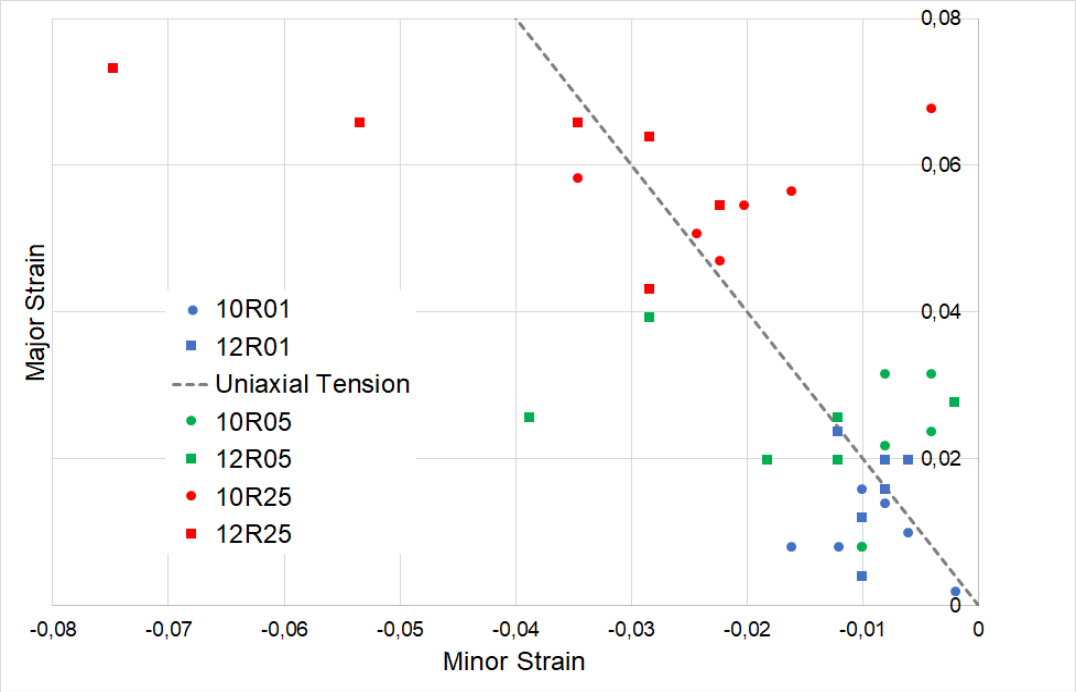

Figure 4.9 - Notch tensile tests loading paths for DP1000 steel

The results show that with a greater notch radius the specimen achieve higher values of strain. According to the literature, the three specimens should have produced different loading paths, although that did not happen. As previously mentioned, these materials present a very localized necking, around the fracture and the fact that the circumferences had an initial 5 mm diameter led to a difficult measurement procedure, especially for the specimen with a notch radius of 5 mm and 1 mm.

Unlike the Nakajima test, the tested specimen does not exhibit curvatures and the methodology using photoshop showed to be very accurate.

4.1.3 U-shaped bend test

The U-shaped bend tests were performed with two main goals in this dissertation, study and quantify the springback phenomenon and to validate constitutive material models regarding springback prediction.

Initially, during the experimental tests, the punch and the specimen were not properly aligned which led to a significant difference in springback between either side of the blank. This was corrected by drilling the specimens to hold the sheet preventing it from slipping. All specimen's measurements can be found in Appendix A.1, while the mean and standard deviation are shown in Table 4.1.

The specimen from different tests are identified as AAPBBRCC, where AA denotes the specimen's thickness, PBB means the width of the punch used in the test and RCC represents the radius of the punch. For instance, 12P60R10 corresponds to the test which the specimen has 1.2 mm of thickness and the punch has a width of 60 mm and a 10 mm radius. The rest of the test setup can be found in Table 3.8 of the Methodology chapter.

According to the literature, there are a certain number of variables that influence the amount of springback exhibited by the sheet after a stamping process, like the punch/die radius, sheet thickness, the blank holder load, etc. Since these tests have different setups, the influence of the sheet thickness and punch/die radius can be studied.

Table 4.1 - Mean and standard deviation of the U-shaped bend tests specimen's measurements for DP1000

Specimen	1/R [mm^{-1}]		θ_w [°]	
	$\bar{X}$	SD	$\bar{X}$	SD
10P30R02	0.01453	0.00211	17.03	1.535
10P30R10	0.01386	0.00078	27.21	1.197
12P30R02	0.01295	0.00224	15.21	1.360
12P30R10	0.01259	0.00048	24.88	1.160
10P60R02	0.01539	0.00154	19.74	1.598
10P60R10	0.01268	0.00065	31.37	1.020
12P60R02	0.01155	0.00135	17.14	1.099
12P60R10	0.01327	0.00076	28.64	0.957

To study the influence of a certain tool parameter, in the amount of springback exhibited after the test, the setups that must be compared with each other can only present one variable. This means that, for instance, to study the influence of the sheet thickness the punch and die radius must be the same in both setups and the only variable is the thickness of the specimen.

The results obtained for the variation of the punch and die radiuses from 10 mm and 15 mm to 2 mm and 3 mm, respectively, show that the amount of springback is highly influenced by these tool parameters. Smaller punch and die radiuses lead to a smaller springback effect after the forming process. Table 4.2 illustrates the springback reduction in the U-shaped bend test when the punch and die radiuses are changed from 10 mm and 15 mm to 2 mm and 3 mm respectively, where the minus sign represents a decrease and plus sign an increase of the respective parameter.

Table 4.2 - Influence of the punch and die radiuses in DP 1000 springback

Test setup	R (%)	θ_w (%)
10P30	+11.35	-45.59
10P60	-9.85	-40.76
12P30	-11.02	-41.54
12P60	+18.52	-44.67

The specimen's thickness also influenced the springback phenomenon. This influence is illustrated in Table 4.3, where the results are based on changing from 1.0 mm to 1.2 mm thickness. The increase of the sheet thickness reduces the springback.

Table 4.3 - Influence of the sheet thickness in DP1000 springback

Test setup	R (%)	θ_w (%)
P30R02	+16.50	-10.02
P30R10	+23.99	-8.56
P60R02	+34.24	-10.40
P60R10	+4.30	-7.45

The increased sheet thickness and small punch/die radius decreased significantly the springback. However, DP1000 still presented large springback. The increase of the blank holder load is also a parameter that reduces this phenomenon, however it was not comprised in this study.

Table 4.4 - Mean and standard deviation of the U-shaped bend tests specimen's measurements for DP1200

Specimen	1/R $[mm^{-1}]$		θ_w [°]	
	$\bar{X}$	SD	$\bar{X}$	SD
10P30R10	0.01453	0.00211	17.03	1.535
10P60R10	0.01386	0.00078	27.21	1.197

Even though that only two different setups for the U-shape bend test of DP1200 steel were performed, the measurement results clearly show that the springback effect is greater in DP1200 steel than in DP1000 steel.

4.2 Simulations

4.2.1 Identification of material parameters

The identification of material parameters for constitutive modeling is an important step of the simulation process. In this stage, one can understand which phenomena are considered by each material model.

4.2.1.1 Material Type 3

As previously mentioned in the Methodology section, MT3 is a simple bilinear model, and since the yield tensile strength and Young's modulus are already known from the stress-strain curves shown in Figure 3.1, only the plastic component of the stress-strain curve has to be studied to obtain the tangent modulus. Figure 4.10 illustrates how the bilinear curve is obtained based on the experimental true stress vs plastic strain curve. As shown in equation (4.1) the tangent modulus is the slope of the line.

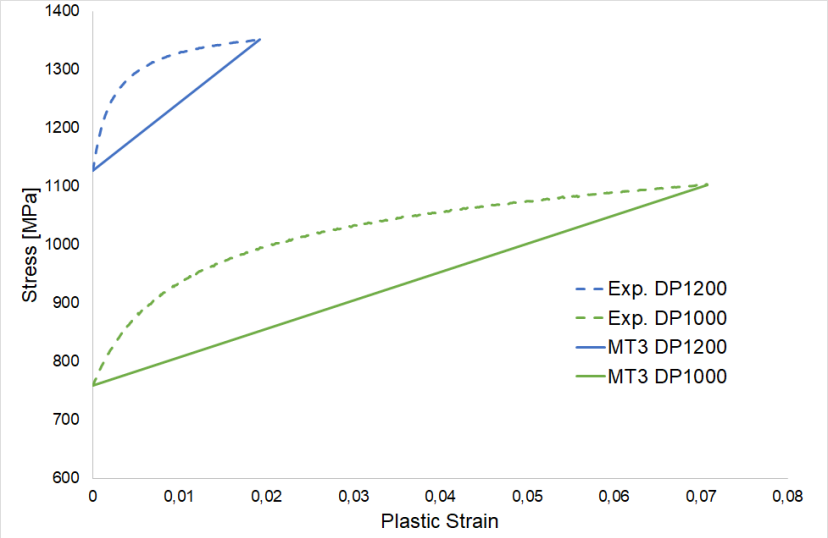

Figure 4.10 - True Stress vs Plastic Strain curve with MT3

$$\sigma = E_t \varepsilon_p + \sigma_y \tag{4.1}$$

The obtained material parameters can be found in Table 4.5. Where ρ, v and σ_y represent the volumetric mass density, Poisson's ratio and yield tensile strength respectively.

Table 4.5 - Material Type 3 parameters

Material Model Parameters	$\rho\ [ton/mm^2]$	$E\ [MPa]$	v	$\sigma_y\ [MPa]$	$E_t\ [MPa]$	β'
DP1000	7.85×10^{-9}	207×10^3	0.3	757.8	4866.8	$\{0, 0.5, 1\}$
DP1200				1126.5	11725	

The use of three different values for β allow the material model to obtain an isotropic, kinematic and combined isotropic-kinematic formulation, as stated in the Methodology chapter.

This material model does not capture any significant phenomena of DP steels, such as the continuous elastic-plastic transition, the hardening behaviour, anisotropy, etc.

4.2.1.2 Material Type 18

This isotropic hardening model based on the Ludwik-Hollomon equation to define the material behaviour. DP steels do not have a constant n-value (hardening exponent) but after a certain amount of plastic strain, this value stabilizes. Thus, the curve fitting will in the last 50% of the true stress-plastic strain curve as illustrated in Figure 4.11. The parameters obtained by curve fitting with the experimental results (uniaxial tension test), are present in Table 4.6.

As can be seen in Figure 4.11, this material model does not capture the hardening behaviour of both DP steels in study. Also, because it's an isotropic hardening model, it does not capture the Bauschinger effect. The sheet anisotropy is not considered by this model.

Table 4.6 - Material Type 18 parameters

Material Model Parameters	$\rho\ [ton/mm^2]$	$E\ [MPa]$	v	$\sigma_y\ [MPa]$	K	n
DP1000	7.85×10^{-9}	207×10^3	0.3	757.8	667	0.25
DP1200				1126.5	442	0.17

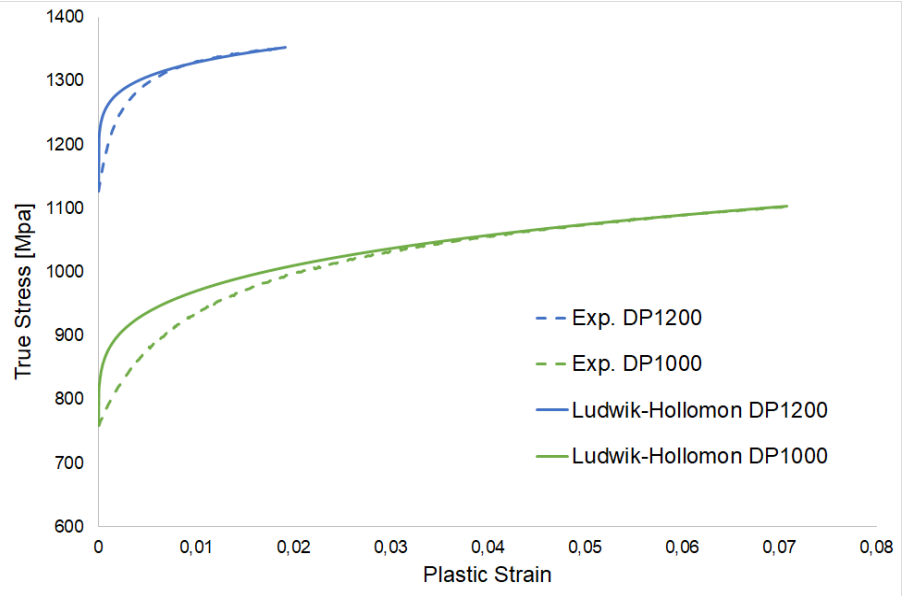

Figure 4.11 - True stress vs plastic strain with Ludwik-Hollomon equation

4.2.1.3 Material Type 36

MT 36 is an isotropic hardening model with the Barlat and Liam (1989) yield criterion [22]. The yield function is automatically calculated by the software when the Lankford coefficients in 0, 45 and 90-degree directions from the rolling direction.

Unlike MT 3 and 18, the experimental true stress vs plastic strain curve from the uniaxial tensile test can be given as an input. So, the hardening behaviour of DP1000 and DP1200 is successfully captured by this model, which is an improvement from the previous material types. The yield function also considers the sheet anisotropy, and the respective rolling direction (based on the local element directions).

Table 4.7 - Material Type 36 parameters

Material Model Parameters	$\rho\ [ton/mm^2]$	$E\ [MPa]$	v	r_0	r_{45}	r_{90}	M
DP1000	7.85×10^{-9}	207×10^3	0.3	0.737	1.087	1.172	6
DP1200				1.019	1.506	1.319	

4.2.1.4 Material Type 37

This material type is an isotropic hardening model with the Hill (1948) yield criterion. Only transverse anisotropy is considered (normal anisotropy coefficient). The experimental load curve can also be used as an input. The main difference between MT36 and MT37 is that the current model has the option of including Young's modulus degradation through the Yoshida-Uemori equation. The Yoshida-Uemori constants were obtained in previous stages of the project where the main goal was to characterize the materials in study.

The Bauschinger effect and reverse stress characteristics are not considered by this material model due to the hardening rule being isotropic. Although, other important phenomena like Young's modulus degradation, normal anisotropy, and the hardening behaviour are characterized. The parameters for this material model are presented in Table 4.8.

Table 4.8 - Material Type 37 parameters

Material Model Parameters	$\rho\ [ton/mm^2]$	$E\ [MPa]$	v	$\sigma_y\ [MPa]$	$\bar{r}$	$E_a\ [MPa]$	ξ
DP1000	7.85×10^{-9}	207×10^3	0.3	757.8	1.021	155000	60
DP1200				1126.5	1.337	178900	92.9

4.2.1.5 Material Type 103p

This material type is a simplified version of MT103 that uses a visco-plastic formulation while this material model reduces that formulation to an elasto-plastic behaviour. The hardening behaviour is given by the experimental curve (true stress vs plastic strain). This material model is very similar to MT36, the only difference being the yield criterion. This material model considers the sheet anisotropy, the yield surface behaves with isotropic hardening, and the behaviour in stress-strain is captured by the true stress-strain curve from the experimental test. The material parameters are shown in Table 4.9.

Table 4.9 - Material Type 103p parameters

Material Model Parameters	$\rho\ [ton/mm^2]$	$E\ [MPa]$	v	$\sigma_y\ [MPa]$	r_0	r_{45}	r_{90}
DP1000	7.85×10^{-9}	207×10^3	0.3	757.8	0.737	1.087	1.172
DP1200				1126.5	1.019	1.506	1.319

4.2.1.6 Material Type 125

Material Type 125 is the Yoshida-Uemori model combined with MT37. This is a two-surface constitutive material model that uses kinematic hardening for the yield surface and a combined isotropic-kinematic hardening for the bounding surface. In total, there are 11 material parameters to identify from two different characterization tests, cyclic loading-unloading tensile and tension-compression tests.

Since the alternated tension-compression tests were not performed due to equipment and sample (sheet) limitations, not all the material parameters could be identified from the experimental test performed for the ULTRAFORMING project. Thus, the parameters that could not be identified are the reverse stress (C and h) that characterize the transient Bauschinger effect, and the early re-yielding. Thus, the reverse stress parameters were obtained from the work of Ali Anyanpour and Daniel Green [35] for DP980 steel. DP980 presented a lot of similarities to the current DP1000 in study. Although no other parameters were found for DP1200, so those parameters were fixed for both materials.

The curve fitting for the Bounding surface for DP1000 and DP12000 steels, is illustrated in Figure 4.12 and the respective material parameters in Table 4.10. Yield tensile strength, Poisson's ratio and mass density are also material input parameters but since they are presented in the previous material models, they are not present in Table 4.10.

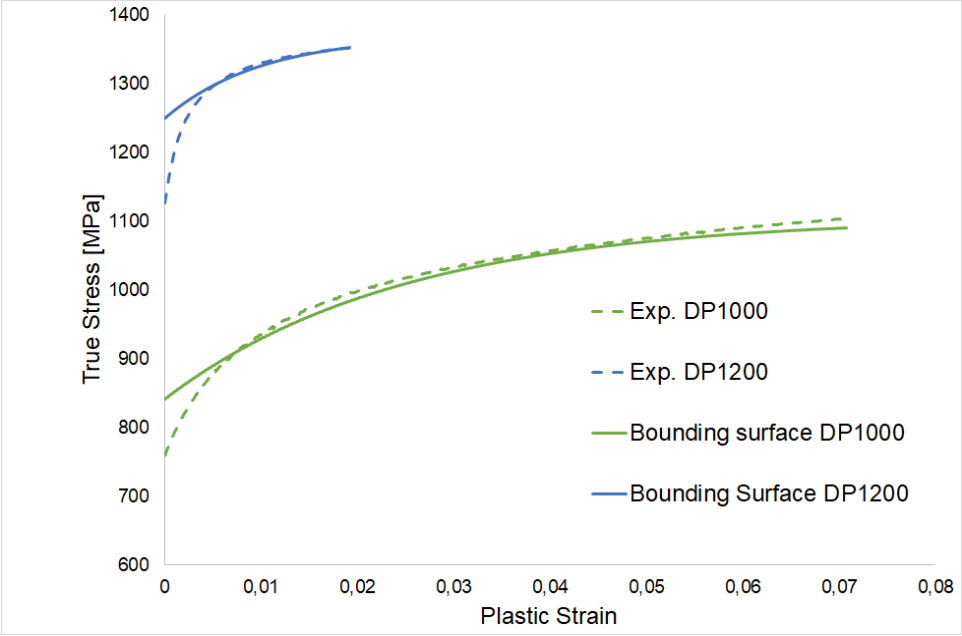

Figure 4.12 - Curve Fitting for Material Type 125

Table 4.10 - Material Type 125 parameters

	$B\ [MPa]$	m	$R_{sat}\ [MPa]$	$b\ [MPa]$	C	H	$E_a\ [MPa]$	ξ	$\bar{r}$
DP1000	840	40	142.9	122.1	239.7	0.821	155000	60	1.021
DP1200	1250	100	70	50			178900	92.9	1.337

These parameters performed well for the U-shaped bend test setups with a higher punch and die radiuses but failed for the smaller ones. However, in the work of Yoshida and Uemori (2003) [27], this model presented good results in the sidewall curl prediction. Thus, the parameters for the reverse stress were altered for the ones presented in the work of T. Phongsai et al. [31] but no significant differences in the results were obtained.

4.2.2 Nakajima Simulations

Initially, for these simulations, a failure criterion was implemented based on the von-Mises and the effective plastic strain. However, this led to an early element erosion (element deletion), and the simulations could not be completely performed, due to the resulting loading paths not being able to develop properly. Thus, the punch displacement is given as input and the major and minor strains are analysed.

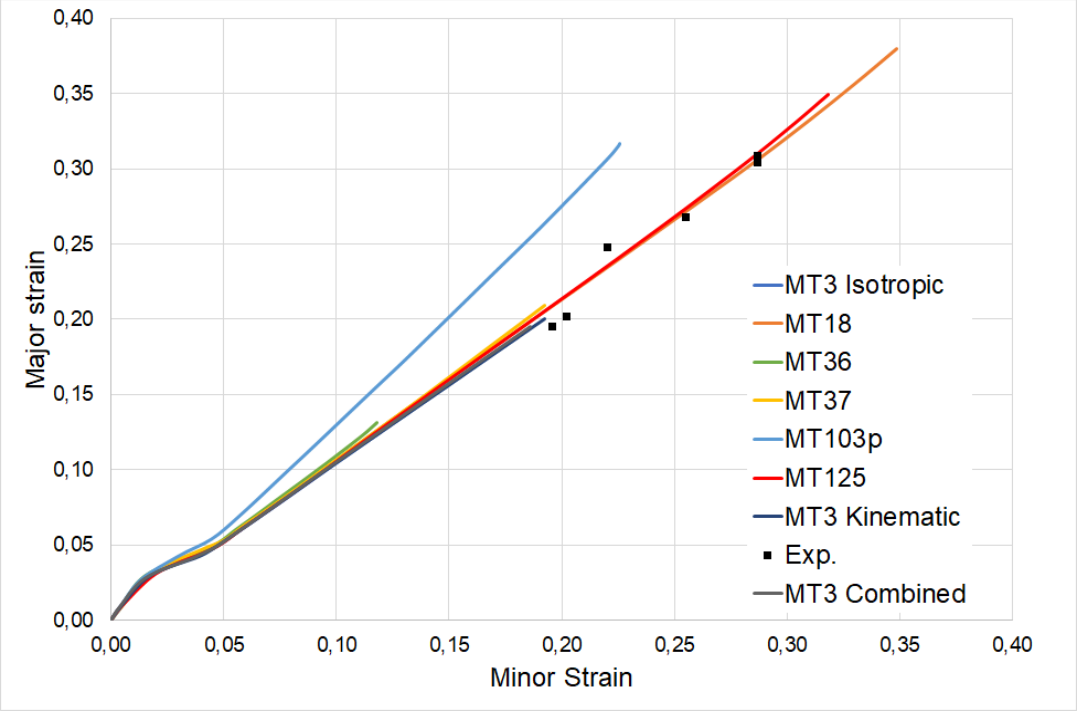

Figure 4.13 – DP1000 Nakajima simulation results for W80 loading path

Figure 4.13 illustrates the loading paths simulated for DP1000 steel with the W80, 1.0 mm thick specimen type. Except for MT103p, all the material models described accurately the loading path, however, only MT125 and MT18 could reach slightly higher values of strain (this was expected since the punch had a higher displacement in the simulation).

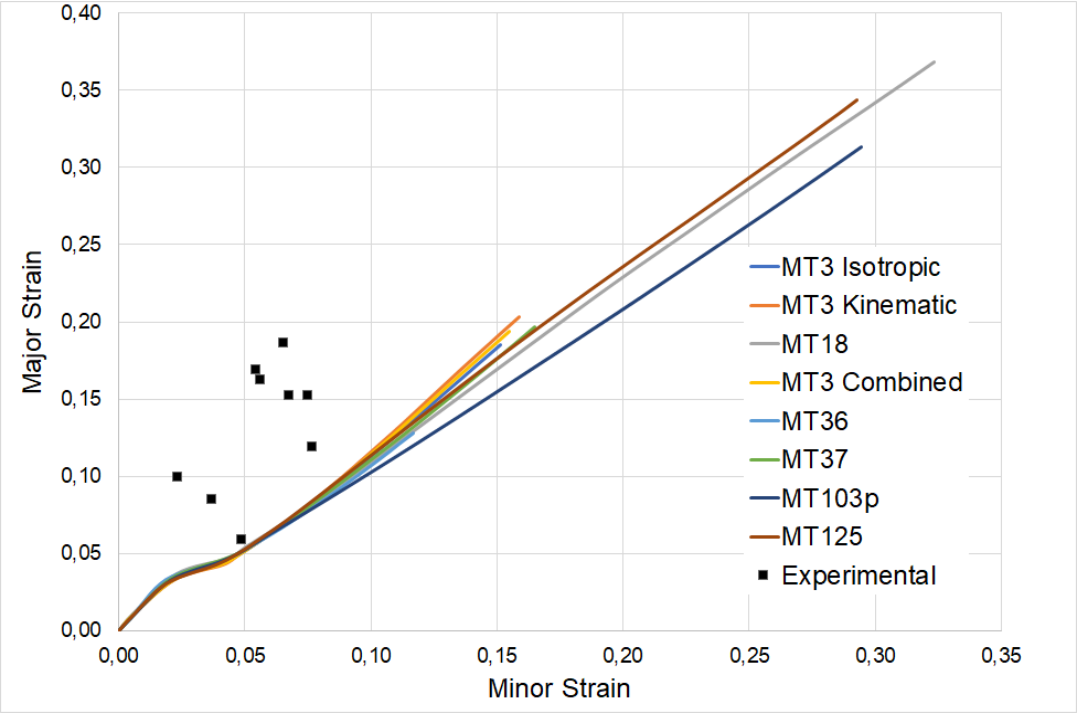

Figure 4.14 – DP1000 Nakajima Simulation Results for W60 loading path

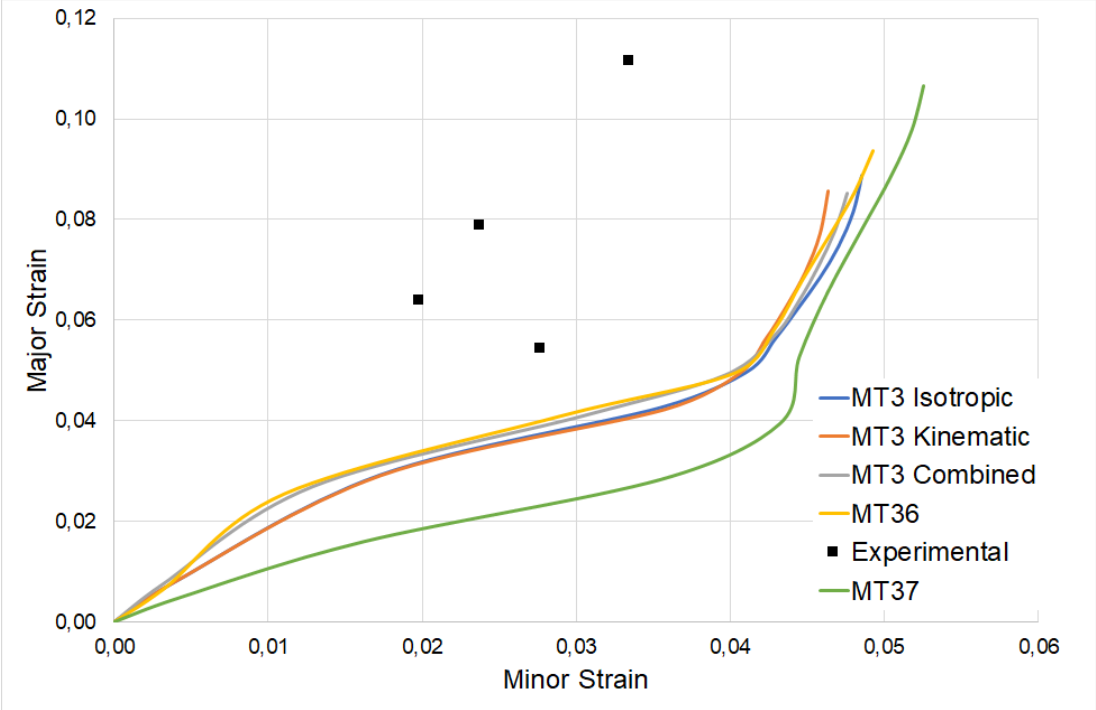

Figure 4.15 – DP1000 Nakajima test simulation results for W40 loading path

Unlike the W80 loading path, the results for the W60 specimen illustrated in Figure 4.14 none of the material models could describe the loading path. Even though that the measurement methods might induce some slight shift in the experimental results, the material models behaved very similarly to the W80 specimen.

The simulations for W40 presented some instabilities in the described loading path, as can be seen in Figure 4.15. This loading path seems to be more complex, since the specimen must adapt in a high nonlinear track, due to the specimen initial adaptation do the punch. Even though that the energy of the simulation showed a quasi-static process for all material models, MT125, MT103p, and MT18 exhibited a large element distortion. In attempt to solve this problem, the mesh was refined, and the tool motion was slowed down. This did not work, and the elements presented the exact same behaviour even though that the hourglass energy remained zero.

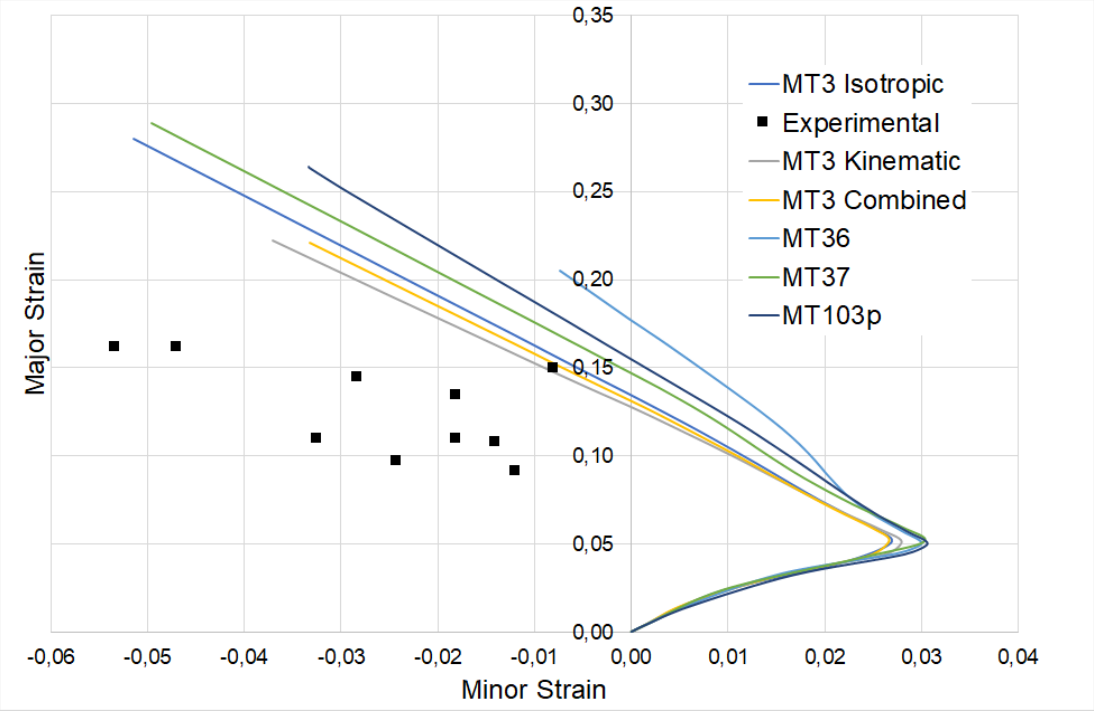

Figure 4.16 – DP1000 Nakajima simulation results for W20 loading path

The path described by the simulations of the W20 specimen for DP1000 steel are illustrated in Figure 4.16. Initially, the elements expand in both Major and minor strains followed by a sudden change in the trajectory. This might be the influence of the friction between the punch and the specimen. MT125 revealed once more large element distortions when the trajectory shifts. MT103p was the one closest to the experimental measurements, although none of the material models could accurately describe the loading path.

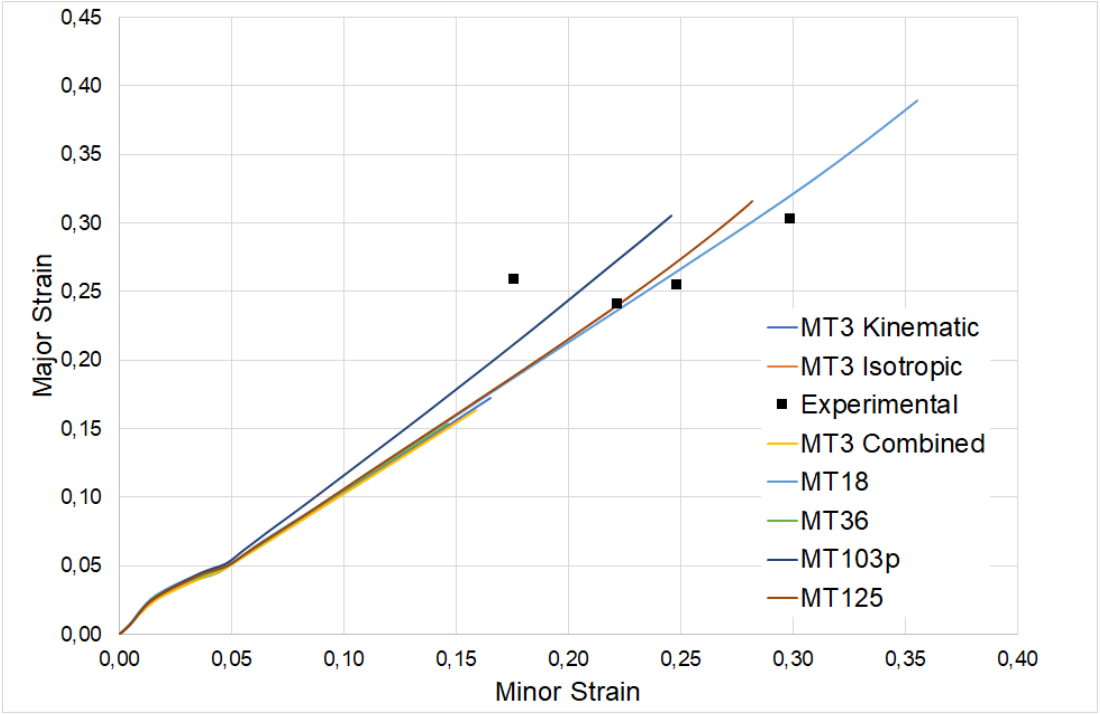

Figure 4.17 - DP1200 Nakajima simulation results for W80 loading path

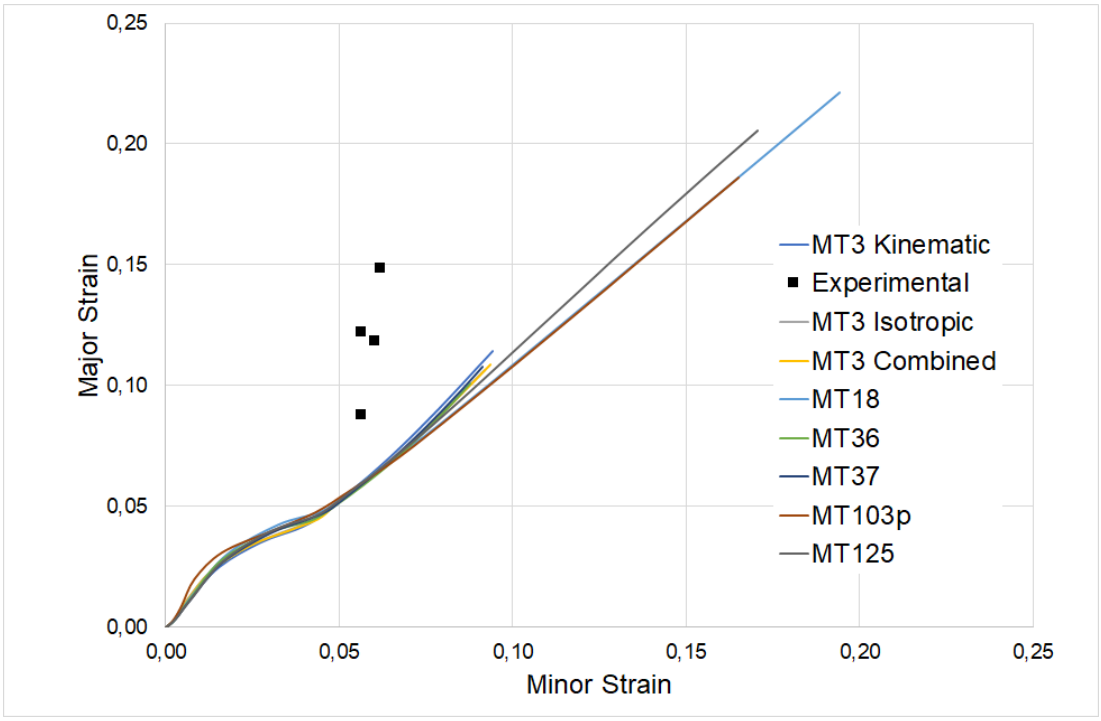

Figure 4.18 - DP1200 Nakajima simulation results for W60 loading path

The results for DP1200 Nakajima test with W80 specimen type are illustrated in Figure 4.17. Like with DP1000, the material models can describe this loading path, although MT103p seems to have slightly shifted. Overall, all the material models presented a similar behaviour.

W60 loading path described by the material models also exhibited resemblance to the results obtained for DP1000. The path does not match the experimental measurements and did not follow de experimental measurements.

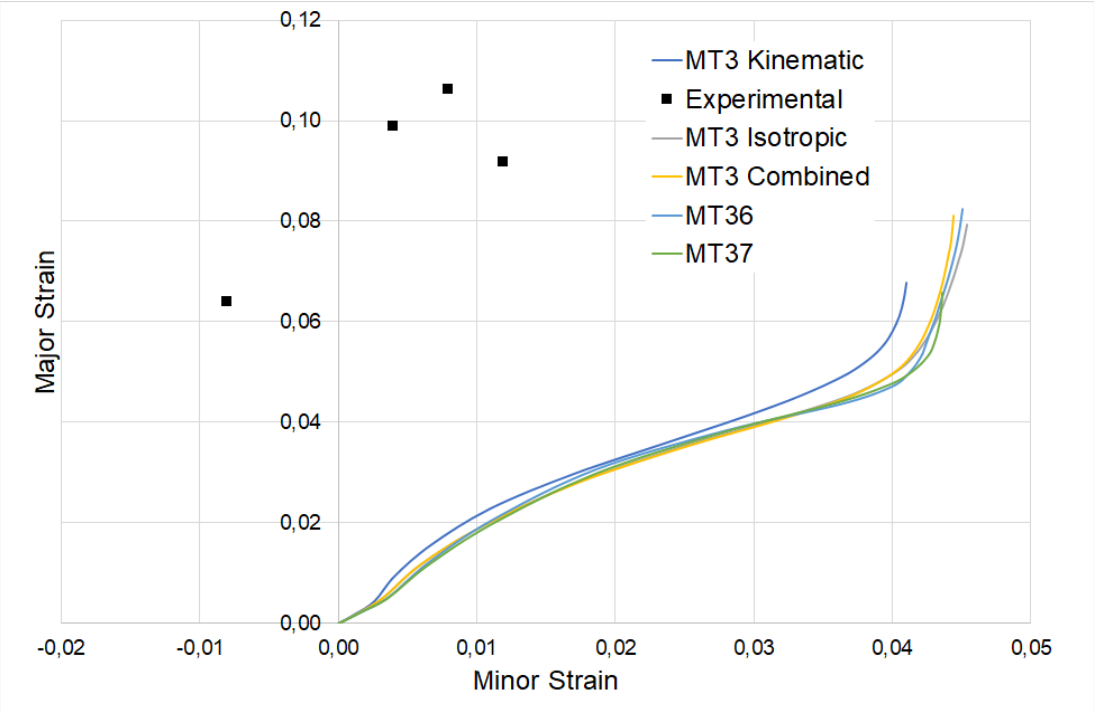

Figure 4.19 - DP1200 Nakajima simulation results for W40 loading path

The same material models that presented a large element distortion for W40 with DP1000 material parameters also behaved for the same specimen type with DP1200 steel. Even though that some material models could perform the simulation, the complex loading path does not find the experimental results.

Except for MT103p, all material models characterized well the W80 loading path but only MT125 achieved the strain values like the experimental results. As for the other loading paths, all material models behaved similarly, even though that the path is different from the experimental test. Since the measurement procedure might have induced some errors, it's not conclusive that the material models could not characterize the different loading paths. Regarding MT125, Ali Aryanpour et al. [35]] stated that this material model might be poorly implemented in the software, although, the energy problems were not found in this study.

4.2.3 Notch Tensile Test

The notch tensile tests were only performed for DP1000. And only one of the specimen types was simulated, the one where the notch radius is 25 mm for 1.0 mm thickness. The results of the simulation and the experiments are illustrated in Figure 4.20.

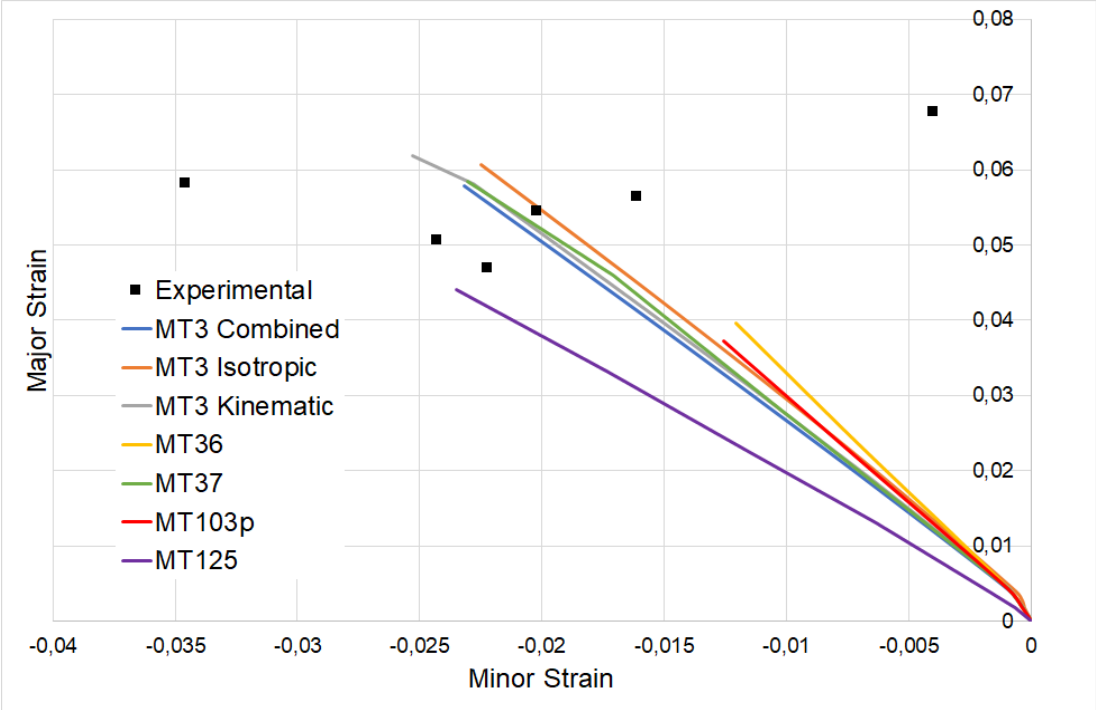

Figure 4.20 - R25 Notch Tensile test simulation for DP1000

In these simulations, all constitutive models behaved similarly regarding the loading path. MT36 and MT103p underestimate the major and minor strains, while all the other material models seem to reach satisfactory results. Due, to the large dispersion of the experimental results, it is not clear which material model better suits for this test. Overall, the material models show accuracy for the elementary loading paths.

4.2.4 U-Shaped Bend Test Simulation

In this section, the LS-DYNA material models are studied for their application to springback prediction. The results show the sidewall curl and the opening angle as a function of the punch radius. The evolution of the springback with the punch radius is not linear, however, the

experimental test performed only considered two different punch radiuses. It is important to notice that the die radius also change, as mentioned in the Methodology section.

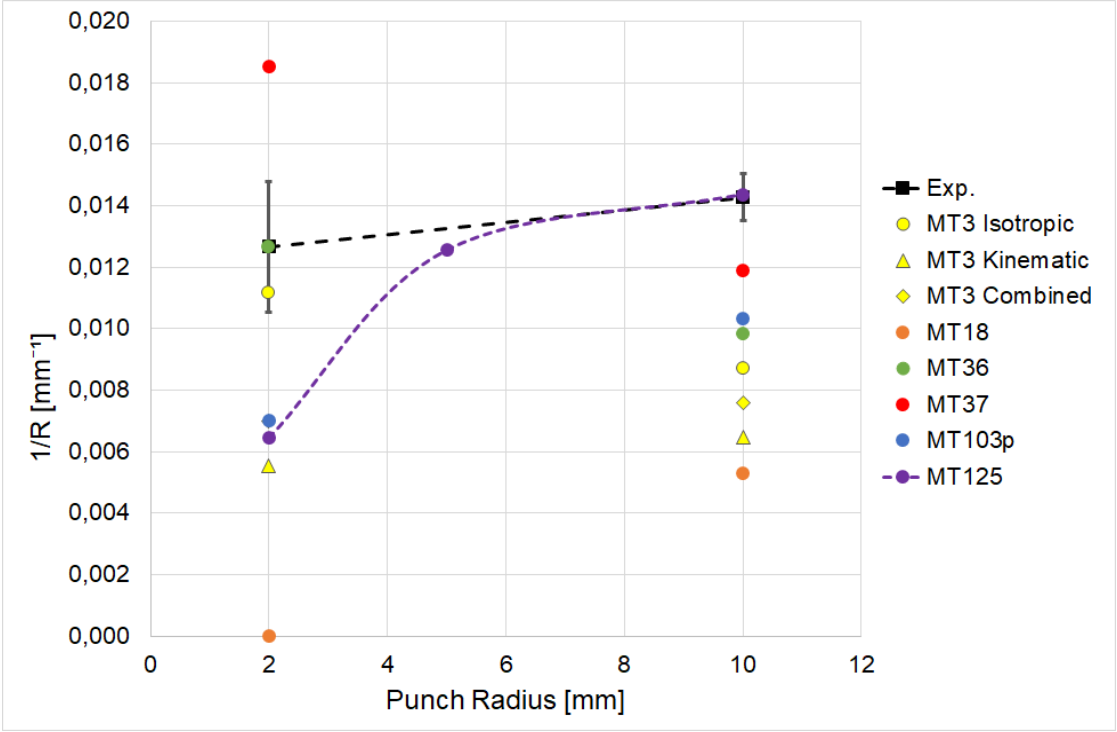

Figure 4.21 - Sidewall curl after springback with 10P30 setup for DP1000 steel

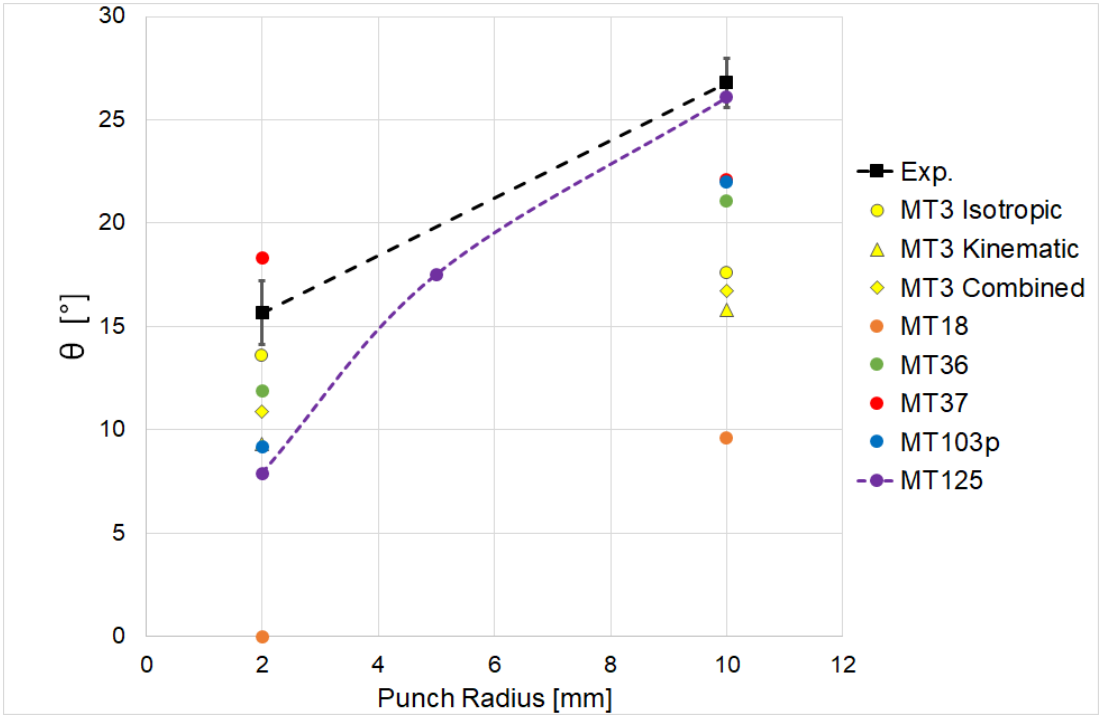

Figure 4.22 - Opening angle after springback with 10P30 setup for DP1000 steel

Figure 4.21 and Figure 4.22 illustrate the comparison between the springback calculated by the material models with the experimental result for the sidewall curl and the opening angle, respectively, for the 10P30 test setup with both punch/die radiuses. The remaining simulation results for DP1000 steel are presented in Appendix A.2. Since the 10P30R10 and 10P60R10 were the only test setups that successfully performed the U-shaped bend test for DP1200 steel, the results are presented in Table A.11.

The three formulations used with material type 3 failed to predict the final geometry of the specimen underestimating the springback. Since it is a bilinear model, the stress-strain curve modelled does not describe the true stress-strain curve behaviour. Thus, it was expected a poor performance regarding the springback prediction. Although, by using three formulations it is possible to study the influence of kinematic, isotropic and combined hardening models. According to Yoshida et al. [27], for smaller punch/die radiuses the material is subjected to severe stretch bending/unbending (when drawn over the punch/die corner) and the springback takes place elasto-plastically, due to the transient Bauschinger effect. The authors also noticed that the Linear-Kinematic (LK) hardening rule underestimates the flow stress for cyclic deformations, resulting in smaller springback. The kinematic formulation in this material model is very similar to the LK used by Yoshida and this is the one that presented smaller springback. Because it considers the Bauschinger effect, the MT3 kinematic showed sensitivity to the punch radius. The isotropic formulation had a reasonable performance in the sidewall curl radius for smaller punch/die radiuses, although the opening angle is significantly underestimated and the overall springback prediction is poor. As illustrated in Table A.11, the isotropic formulation predicted accurately both the sidewall curl and the opening angle for DP1200 with the 10P30R10 setup but did not show consistency and failed to predict the springback for the 10P60R10 setup.

Material Type 18 is an isotropic hardening model with stress-strain curve modelled with the Ludwik-Hollomon's equation, which does not capture the elasto-plastic behaviour of dual-phase steels. This material models presented a very poor springback prediction and it's not suitable for the materials in study. According to this material model, the use of a 2 mm and 3 mm radiuses for the punch and die, respectively, neglects the springback phenomenon, while for higher radiuses the springback exhibited in the simulation is highly underestimated.

Despite MT36 underestimating the springback like the previous models, the results for the sidewall curl showed an improvement for smaller punch/die radiuses in both steels. Using the true stress-strain curve as input, the material model fully captures the elasto-plastic transition between the elastic and plastic deformation. Also, the characterization of the sheet anisotropy with the Barlat and Lian yield criterion is an asset to this material model. The results depicted in Figure 4.21 and Figure 4.22, support the methodology used for these measurements, while MT36 predicted the sidewall curl radius, it could not predict the opening angle. If only the side wall is considered, the measurements might have been misleading. As resemblance to MT3 Isotropic, the material predicted accurately the springback in 10P30R10 setup for DP1200 but not for 10P60R10.

The only material model that overestimated the springback for punch and die radiuses for DP1000 steel, was material type 37. The Yoshida-Uemori equation for Young's modulus degradation as a function of the plastic strain had a significant impact on the amount of springback exhibited in the simulation, which agrees with Al Azraq [13] when the author states that a smaller elastic modulus leads to a higher springback phenomenon. For the specimens with 1.2 mm thickness, this material model accurately predicted the springback for the smaller punch radius, while it did not show consistency for the higher radius (while simulating with DP1000 material parameters). Since both steels have transverse anisotropy, the yield criterion in this model considering the normal anisotropy coefficient is an advantage to the previous models. As for DP1200 the material model failed to predict the springback.

The material model MT103p is very similar to MT36 being the difference in the yield criterion. The results for both material models are very similar (with both steels) for different 10 mm punch radius setups. Although MT103 demonstrated a much higher sensitivity to the smaller punch/die radius and always underestimated the springback phenomenon.

Material Type 125 is the Yoshida-Uemori model with transverse anisotropy. This material model predicted the springback accurately, for the higher punch radius with both 10P30 and 10P60 test setups. Increasing the sheet thickness for 1.2 mm, the material model presented reasonable results but with 12P60 setup failed to describe the sidewall curl. Even though that for the higher punch radius the material model behaved in agreement with the work of Yoshida and Uemori [27], the material model exhibited a high sensitivity to the punch radius and these results were not consistent to the smaller punch radius. The authors used a punch and die with 5 mm and 2 mm, respectively. In this study, the punch and die had 2 mm and 3mm radius, respectively. Thus, a simulation with a punch of 5 mm and a die of 7.5 mm radius was performed for this material model to study the evolution of the springback exhibited with the variation of the punch radius. The results show that this evolution is not linear and that the model may be accurate from a certain punch radius. However, experimental tests must be performed for comparison. The reverse stress parameters were obtained from the work of Ali Anyanpour et al. [35] with DP980 steel, as previously mentioned. Thus, tension-compression tests must be performed, for the steels in study, since the transient Bauschinger effect, permanent softening and work hardening stagnation are important phenomena to consider in the simulations with smaller punch and die radiuses. A sensibility analysis was performed and the parameters that significantly influence the springback were the R_{sat} and B, which are used for modelling the bounding surface. Since the parameters from reverse stress were the same for DP1200, the Bauschinger effect modelled does not follow the material behaviour, even though that this model predicted the springback for the 10P60R10 setup, it failed for 10P30R10.

5 Conclusions and Future Work

The main goal of the present dissertation was to study and validate constitutive models for loading paths characterization and springback prediction for AHSS steels, DP1000, and DP1200. This final chapter presents the conclusions from all the results obtained in this study and suggestions for future work.

Except for MT103p, all material models described the elementary loading paths (uniaxial and biaxial tension) accurately, highlighting the MT125 (Yoshida-Uemori model) that not only followed the loading paths but also had a good performance in the strain values resultant from the punch displacement.

As for the more complex loading paths, the experimental results and the simulations do not exhibit similar paths. The measurement methodology for the Nakajima test specimens might have influenced the resulting loading path, since it does not consider the curvatures in the deformed specimen. More complex models, such as MT125 and MT103p, presented a large element distortion for the W40 and W20 loading path. Although a more refined mesh and an adaptive mesh refinement were tested, the elements exhibited the same behaviour. The source of the problem was not found since the energy calculations showed a quasi-static process, no energy associated with large element distortion (hourglass energy) and no contact instabilities.

Material Type 125 presented good results in springback predictions for the test setups with a 10 mm punch and 15 mm die radiuses. However, it presented a high sensitivity to the punch/die radius reduction. A simulation with a 5 mm punch radius was performed to study the evolution of the springback simulated as a function of the punch radius. Using an interpolation between the three points, it can be concluded that this material model approximates to the experimental results with higher punch radiuses

For smaller punch and die radiuses the material type 37 was the only material model to overestimate the springback, due to the degradation of the elastic modulus. The fact that MT37 is always closer to the experimental results than MT36, in springback prediction, indicates that the normal anisotropy and the Young's modulus degradation are important phenomena to consider for DP1000 and DP1200.

The methodology used for the measurement of the U-shaped bend test demonstrated to be suitable since some material models accurately described (in some cases) the sidewall curl radius

but not the opening angle. The use of both parameters is important due to the large springback exhibited by DP1000 and DP1200.

The main objectives of this dissertation were achieved, however, further investigation can be conducted, namely:

- Perform the Nakajima tests controlling the punch depth in order to stop the test immediately thus avoiding the opening of the fracture;
- Perform the tension-compression tests to obtain all the material parameters for the Yoshida-Uemori model;
- Implement a user-defined model and simulate the complex loading paths of the Nakajima test;
- Perform U-shaped bend tests with a setup whose punch and die radiuses are 5 mm and 7.5 mm, respectively. Other intermediate radiuses between 2 and 10 mm (for the punch), and 3 and 15 mm (for the die) should be tested as well to observe the influence of the tool's radius in the evolution of springback and compare the results with complex material models such as the Yoshida-Uemori.

References

[1] S. Keeler, M. Kimchi, and P. Mooney, 'Advanced High-Strength Steels Application Guidelines'. WorldAutoSteel, Sep-2017.

[2] R. Kuziak, R. Kawalla, and S. Waengler, 'Advanced high strength steels for automotive industry', *Arch. Civ. Mech. Eng.*, vol. 8, no. 2, pp. 103–117, Jan. 2008.

[3] J. P. P. de S. Amorim, 'Soldadura laser do aço dual-phase 1000', Master Dissertation, Universidade de Aveiro, 2016.

[4] C. Tamarelli, 'AHSS 101: The Evolving Use of Advanced High-Strength Steels for Automovive Applications', Steel Market Development Institute Report, 2011.

[5] S. C. Simões, 'Caracterização experimental e não-destrutiva de aços de alta resistência, DP1000 e DP1200', Master Dissertation, Faculdade de Ciências e Tecnologia da Universidade Nova de Lisboa, 2017.

[6] J. Ha, J. Lee, J. H. Kim, M.-G. Lee, and F. Barlat, 'Investigation of plastic strain rate under strain path changes in dual-phase steel using microstructure-based modeling', *Int. J. Plast.*, vol. 93, pp. 89–111, Jun. 2017.

[7] P. Tsipouridis, 'Mechanical properties of Dual-Phase steels', Doctoral Dissertation, Techinischen Universitat Munchen, 2006.

[8] E. Billur and T. Altan, 'Challenges in Forming Advanced High Strength Steels', 2010.

[9] G. R. Speich, V. A. Demarest, and R. L. Miller, 'Formation of Austenite During Intercritical Annealing of Dual-Phase Steels', *Metall. Mater. Trans. A*, vol. 12, no. 8, pp. 1419–1428, Aug. 1981.

[10] J. Rodrigues, *Tecnologia mecânica: tecnologia da deformação plástica*. Escolar Editora, 2005.

[11] H. Kim, C. Kim, F. Barlat, E. Pavlina, and M.-G. Lee, 'Nonlinear elastic behaviors of low and high strength steels in unloading and reloading', *Mater. Sci. Eng. A*, vol. 562, pp. 161–171, Feb. 2013.

[12] X. Xue, J. Liao, G. Vincze, A. B. Pereira, and F. Barlat, 'Experimental assessment of nonlinear elastic behaviour of dual-phase steels and application to springback prediction', *Int. J. Mech. Sci.*, vol. 117, pp. 1–15, Oct. 2016.

[13] S. M. S. Al Azraq, 'Numerical simulation of metal sheet plastic deformation processes through finite element method', Doctoral Thesis, Università degli Studi di Napoli Federico II, 2007.

[14] J. Jung, S. Jun, H.-S. Lee, B.-M. Kim, M.-G. Lee, and J. H. Kim, 'Anisotropic Hardening Behaviour and Springback of Advanced High-Strength Steels', *Metals*, vol. 7, no. 11, p. 480, Nov. 2017.

[15] F. Zhalehfar, S. J. Hosseinipour, S. Nourouzi, and H. Gorji, 'Numerical Investigation into the Effect of Uniaxial and Biaxial Pre-Strain on Forming Limit Diagram of 5083 Aluminum Alloy', *AIP Conf. Proc.*, vol. 1383, Aug. 2011.

[16] C. D. Schwindt, M. Stout, L. Iurman, and J. W. Signorelli, 'Forming Limit Curve Determination of a DP-780 Steel Sheet', *Procedia Mater. Sci.*, vol. 8, pp. 978–985, Jan. 2015.

[17] R. Wesenjak, C. Krempaszky, and E. Werner, 'Prediction of forming-limit curves of dual-phase steels based on a multiple length scale modelling approach considering material instabilities', *Comput. Mater. Sci.*, vol. 111, pp. 277–288, Jan. 2016.

[18] F. Yoshida and T. Uemori, 'A model of large-strain cyclic plasticity describing the Bauschinger effect and workhardening stagnation', *Int. J. Plast.*, vol. 18, no. 5, pp. 661–686, Oct. 2002.

[19] X. Lemoine and A. Aouafi, 'Bauschinger effect correspondence of experimental tests', *Int. J. Mater. Form.*, vol. 1, no. 1, pp. 241–244, Apr. 2008.

[20] D. Lee, J. Pons-Prats, H. Espinoza, O. Fruitos, and E. Oñate, 'Multi-Objective Design Optimisation of Stamping Process for Advanced High Strength Steels', 2012.

[21] D. Banabic, *Sheet Metal Forming Processes: Constitutive Modelling and Numerical Simulation*. Berlin Heidelberg: Springer-Verlag, 2010.

[22] F. Barlat and K. Lian, 'Plastic behavior and stretchability of sheet metals. Part I: A yield function for orthotropic sheets under plane stress conditions', *Int. J. Plast.*, vol. 5, no. 1, pp. 51–66, Jan. 1989.

[23] Y. Granbom, 'Structure and mechanical properties of dual phase steels An experimental and theoretical analysis', KTH, Stockholm, 2010.

[24] Kelly, *Solid Mechanics Part II: Engineering Solid Mechanics - small strain. Solid mechanics lecture notes, University of Auckland*. 2012.

[25] G. B. Broggiato, F. Campana, and L. Cortese, 'The Chaboche nonlinear kinematic hardening model: calibration methodology and validation', *Meccanica*, vol. 43, no. 2, pp. 115–124, Apr. 2008.

[26] F. Yoshida, T. Uemori, and K. Fujiwara, 'Elastic–plastic behavior of steel sheets under in-plane cyclic tension–compression at large strain', *Int. J. Plast.*, vol. 18, no. 5, pp. 633–659, Oct. 2002.

[27] F. Yoshida and T. Uemori, 'A model of large-strain cyclic plasticity and its application to springback simulation', *Int. J. Mech. Sci.*, vol. 45, no. 10, pp. 1687–1702, Oct. 2003.

[28] L. Sun and R. H. Wagoner, 'Complex unloading behavior: Nature of the deformation and its consistent constitutive representation', *Int. J. Plast.*, vol. 27, no. 7, pp. 1126–1144, Jul. 2011.

[29] J. Liao, X. Xue, M.-G. Lee, F. Barlat, G. Vincze, and A. B. Pereira, 'Constitutive modeling for path-dependent behavior and its influence on twist springback', *Int. J. Plast.*, vol. 93, pp. 64–88, Jun. 2017.

[30] 'LS-DYNA Manual R10.0 - Vol II — LS-DYNA Support'. [Online]. Available: https://www.dynasupport.com/manuals/ls-dyna-manuals/ls-dyna-manual-r10.0-vol-ii/view. [Accessed: 25-Jul-2018].

[31] T. Phongsai, V. Uthaisangsuk, B. Chongthairungruang, S. Suranuntchai, and S. Jirathearanat, 'Simplified identification of material parameters for Yoshida-Uemori kinematic hardening model', in *International Conference on Experimental Mechanics 2013 and Twelfth Asian Conference on Experimental Mechanics*, 2014, vol. 9234, p. 92340A.

[32] B. N Maker and X. Zhu, 'Input parameters for metal forming simulation using LS-DYNA', Jul. 2018.

[33] 'Contact types — LS-DYNA Support'. [Online]. Available: https://www.dynasupport.com/tutorial/contact-modeling-in-ls-dyna/contact-types. [Accessed: 11-Aug-2018].

[34] B. N. Maker, 'Input Parameters for Springback Simulation using LS-DYNA', Jul. 2018.

[35] A. Aryanpour and D. E. Green, 'Evaluation of LS-DYNA Material Models for the Analysis of Sidewall Curl in Advanced High Strength Steels', presented at the 12th International LS-DYNA Users Conference, 2012.

Appendix

A.1 U-shaped Bend Test Measurements

Table A.1 - 10P30R02 measurements of DP1000 steel

Specimen	Left side		Right side	
	1/R $[mm^{-1}]$	θ_w [°]	1/R $[mm^{-1}]$	θ_w [°]
1	0,01604	18.98	0,01197	15.9
2	0,01582	18.23	0,01177	14.9
3	0,01601	18.53	0,01456	15.64
4	0,01730	17.81	0,01273	16.23

Table A.2 - 10P30R10 measurements of DP1000 steel

Specimen	Left side		Right side	
	1/R $[mm^{-1}]$	θ_w [°]	1/R $[mm^{-1}]$	θ_w [°]
1	0,01492	27.47	0,01438	29.23
2	0,01412	26.67	0,01317	27.43
3	0,01413	28.58	0,01397	26.13
4	0,01413	25.55	0,01355	27.66
5	0,01414	25.73	0,01207	27.68

Table A.3 - 12P30R02 measurements of DP1000 steel

Specimen	Left side		Right side	
	1/R $[mm^{-1}]$	θ_w [°]	1/R $[mm^{-1}]$	θ_w [°]
1	0,01556	17.49	0,01093	14.32
2	0,01464	15.55	0,01054	13.73
3	0,01518	16.68	0,01106	14.46
4	0,01471	15.56	0,01097	13.87

Table A.4 - 12P30R10 measurements of DP1000 steel

Specimen	Left side		Right side	
	1/R $[mm^{-1}]$	θ_w [°]	1/R $[mm^{-1}]$	θ_w [°]
1	0,01224	24.17	0,01349	26.35
2	0,01226	23.77	0,01296	24.77
3	0,01195	22.96	0,01311	25.13
4	0,01221	24.10	0,01274	25.33
5	0,01241	25.62	0,01252	26.64

Table A.5 - 10P60R02 measurements of DP1000 steel

Specimen	Left side		Right side	
	1/R $[mm^{-1}]$	θ_w [°]	1/R $[mm^{-1}]$	θ_w [°]
1	0,01485	20.12	0,01283	17.70
2	0,01629	20.15	0,01435	17.72
3	0,01645	21.67	0,01391	18.62
4	0,01767	21.87	0,01503	19.10
5	0,01739	21.63	0,01514	18.71

Table A.6 - 10P60R10 measurements of DP1000 steel

Specimen	Left side		Right side	
	1/R $[mm^{-1}]$	θ_w [°]	1/R $[mm^{-1}]$	θ_w [°]
1	0,01261	31.92	0,01152	30.73
2	0,01365	31.60	0,01300	30.28
3	0,01287	31.23	0,01225	29.94
4	0,01322	31.66	0,01181	30.66
5	0,01296	32.29	0,01294	33.35

Table A.7 - 12P60R02 measurements of DP1000 steel

Specimen	Left side		Right side	
	1/R $[mm^{-1}]$	θ_w [°]	1/R $[mm^{-1}]$	θ_w [°]
1	0,01458	18.71	0,01159	16.11
2	0,01237	17.30	0,01081	18.43
3	0,01188	17.86	0,01028	15.92
4	0,01214	17.64	0,01036	15.92
5	0,01148	17.65	0,01000	15.87

Table A.8 - 12P60R10 measurements of DP1000 steel

Specimen	Left side		Right side	
	1/R $[mm^{-1}]$	θ_w [°]	1/R $[mm^{-1}]$	θ_w [°]
1	0,01429	27.37	0,01355	27.7
2	0,01308	30.11	0,01305	29.45
3	0,01281	28.83	0,01206	28.63
4	0,01408	27.45	0,01266	28.09
5	0,01428	29.24	0,01279	29.54

Table A.9 - 10P30R10 measurements of DP1200 steel

Specimen	Left side		Right side	
	1/R $[mm^{-1}]$	θ_w [°]	1/R $[mm^{-1}]$	θ_w [°]
1	0,01596	29.58	0,01630	33.72
2	0,01647	31.43	0,01701	31.60
3	0,01606	32.07	0,01739	29.90
4	0,01477	30.62	0,01641	31.11
5	0,01671	31.15	0,01678	30.71

Table A.10 - 10P60R10 measurements of DP1200 steel

Specimen	Left side		Right side	
	1/R $[mm^{-1}]$	θ_w [°]	1/R $[mm^{-1}]$	θ_w [°]
1	0,01896	41.69	55.77	0,01793
2	0,01906	39.52	53.22	0,01879

A.2 U-Shaped Bend Tests Simulation Results

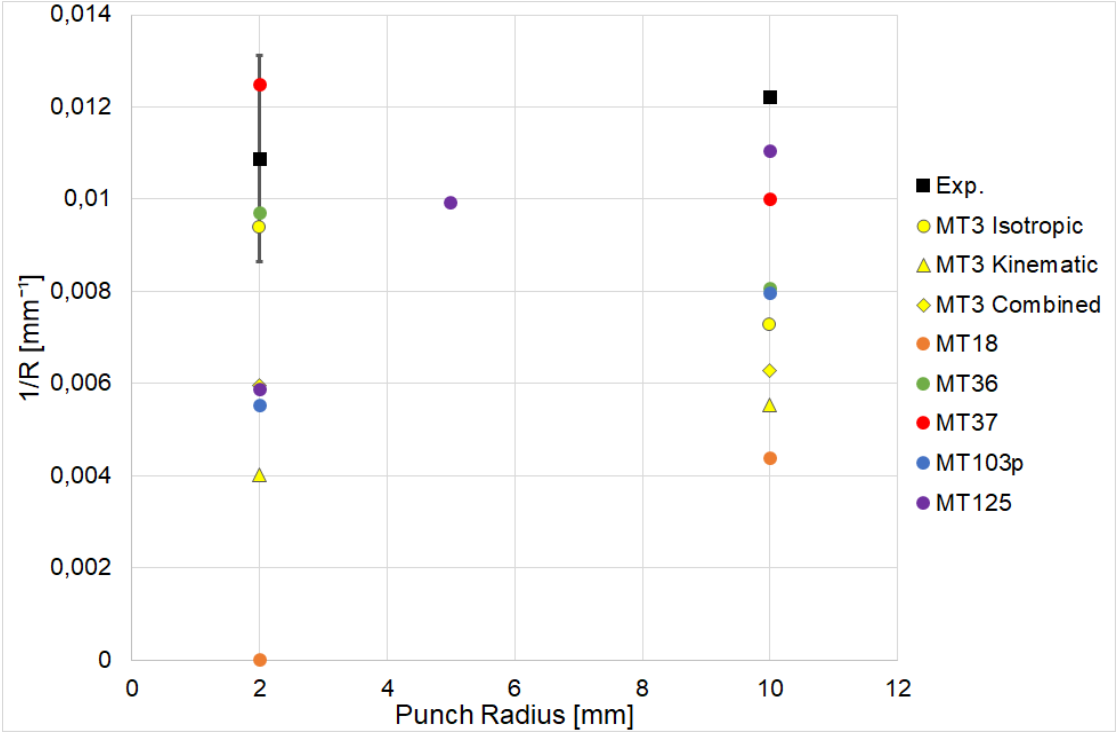

Figure A.0.1 - Sidewall curl after springback with 12P30 setup for DP1000

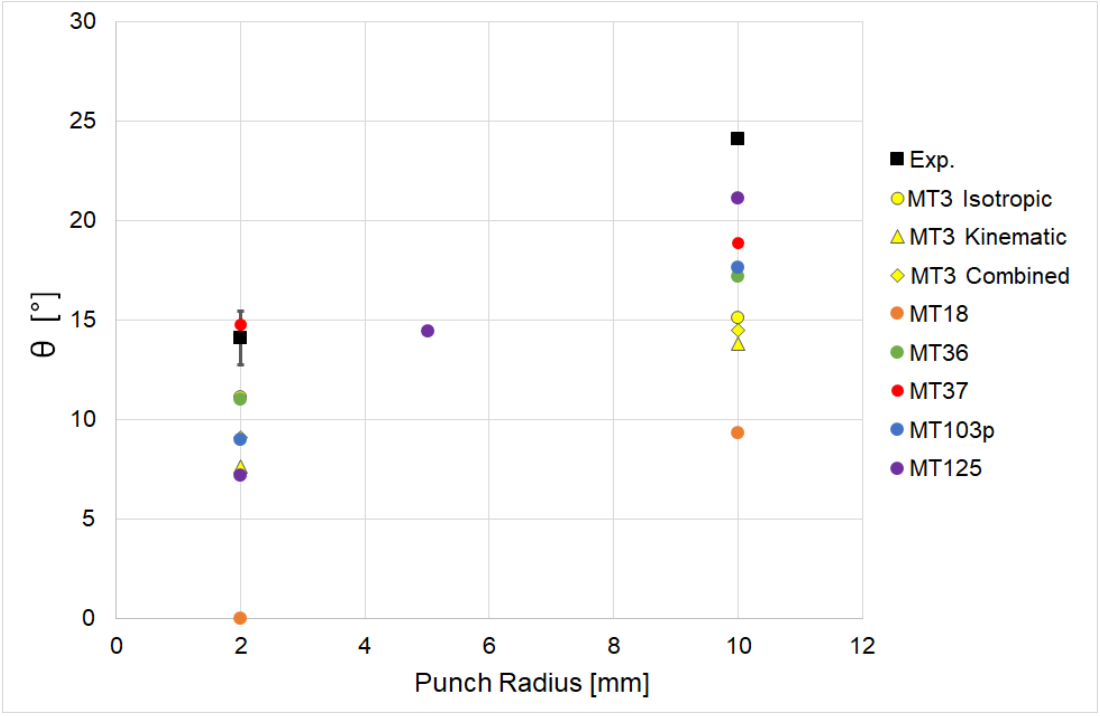

Figure A.0.2 - Opening angle after springback with 12P30 setup for DP1000

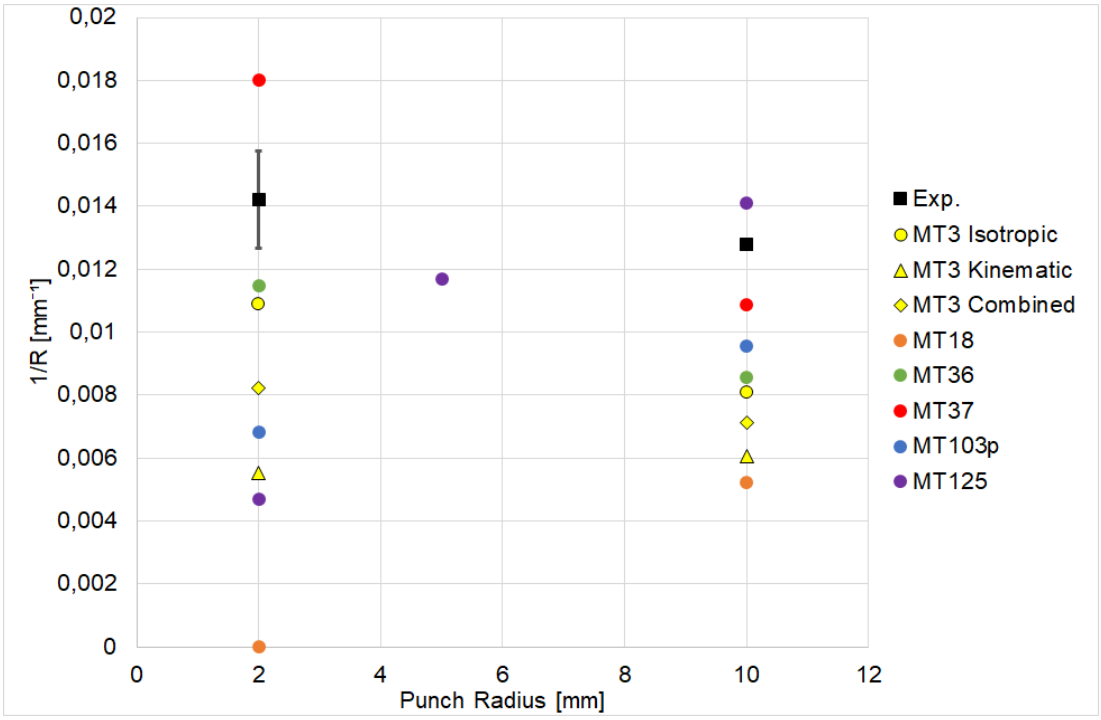

Figure A.0.3 - Sidewall curl after springback with 10P60 setup for DP1000

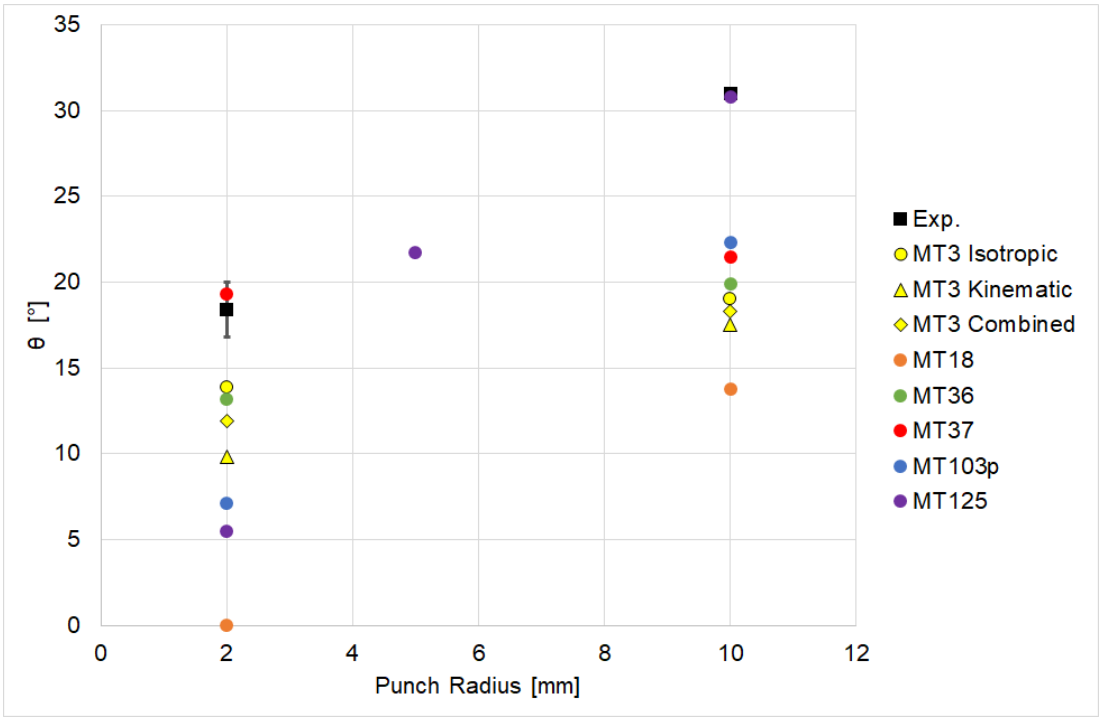

Figure A.0.4 - Opening angle after springback with 10P60 setup for DP1000

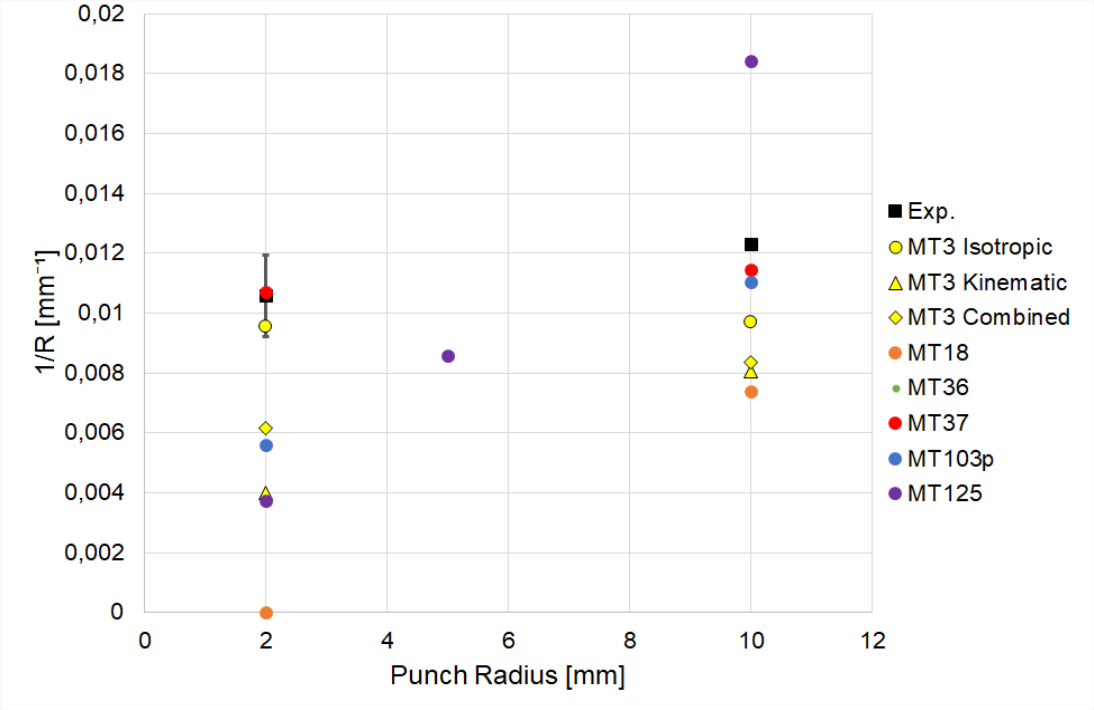

Figure A.0.5 - Sidewall curl after springback with 12P60 setup for DP1000

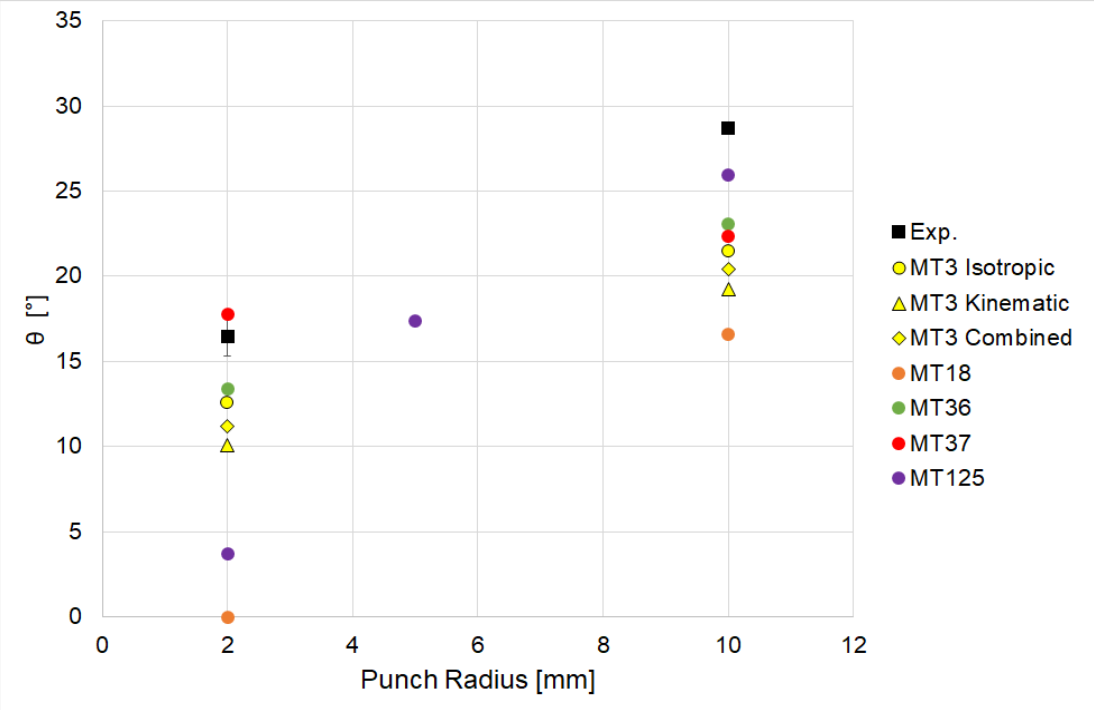

Figure A.0.6 - Opening angle after springback with 12P60 setup for DP1000

Table A.11 - Sidewall curl and opening angle after springback with 10P30R10 and 10P60R10 setups for DP1200

Setup	10P30R10		10P60R10	
Parameter	θ [°]	1/R [mm^{-1}]	θ [°]	1/R [mm^{-1}]
Exp.	31.3	0.01607	41.0	0.01835
MT3 Isotropic	31.4	0.01679	33.4	0.01636
MT3 Kinematic	27.1	0.01121	28.5	0.01069
MT3 Combined	30.0	0.01421	31.2	0.01340
MT18	21.8	0.01113	24.1	0.01092
MT36	30.7	0.01614	31.9	0.01549
MT37	34.4	0.01577	34.4	0.01408
MT103p	31.4	0.01554	31.4	0.01480
MT125	38.1	0.01919	39.5	0.01493